ABSTRACT

Title of dissertation: GEODYNAMIC SIMULATIONS USING THE FAST MULTIPOLE BOUNDARY ELEMENT METHOD

Tyler W. Drombosky, Doctor of Philosophy, 2014

Dissertation directed by: Professor Saswata Hier-Majumder
Department of Geology

Interaction between viscous fluids models two important phenomena in geophysics: (i) the evolution of partially molten rocks, and (ii) the dynamics of Ultralow-Velocity Zones. Previous attempts to numerically model these behaviors have been plagued either by poor resolution at the fluid interfaces or high computational costs. We employ the Fast Multipole Boundary Element Method, which tracks the evolution of the fluid interfaces explicitly and is scalable to large problems, to model these systems.

The microstructure of partially molten rocks strongly influences the macroscopic physical properties. The fractional area of intergranular contact, contiguity, is a key parameter that controls the elastic strength of the grain network in the partially molten aggregate. We study the influence of matrix deformation on the contiguity of an aggregate by carrying out pure shear and simple shear deformations of an aggregate. We observe that the differential shortening, the normalized difference between the major and minor axes of grains is inversely related to the ratio

between the principal components of the contiguity tensor.

From the numerical results, we calculate the seismic anisotropy resulting from melt redistribution during pure and simple shear deformation. During deformation, the melt is expelled from tubules along three grain corners to films along grain edges. The initially isotropic fractional area of intergranular contact, contiguity, becomes anisotropic due to deformation. Consequently, the component of contiguity evaluated on the plane parallel to the axis of maximum compressive stress decreases. We demonstrate that the observed global shear wave anisotropy and shear wave speed reduction of the Lithosphere-Asthenosphere Boundary are best explained by 0.1 vol% partial melt distributed in horizontal films created by deformation.

We use our microsimulation in conjunction with a large scale mantle deep Earth simulation to gain insight into the formation of anisotropy within dense and transient regions known as Ultralow-Velocity Zones, where there is an observed slowdown of shear waves. The results demonstrate a geometric steady state of the dynamic reservoirs by mechanical processes. Within the steady state Ultralow-Velocity Zones, we find significant anisotropy that can explain the speed reduction in shear waves passing through the region.

GEODYNAMIC SIMULATIONS USING THE FAST MULTIPOLE BOUNDARY ELEMENT METHOD

by

Tyler W. Drombosky

Dissertation submitted to the Faculty of the Graduate School of the
University of Maryland, College Park in partial fulfillment
of the requirements for the degree of
Doctor of Philosophy
2014

Advisory Committee:
Assistant Professor Saswata Hier-Majumder, Chair/Advisor
Professor Radu Balan
Associate Professor Ramani Duraiswami
Professor Howard Elman
Associate Professor Kayo Ide
Associate Professor Manuel Tiglio

Preface

Numerical models are a critical component to scientific research. Modern simulations allow scientists and engineers to virtually experiment and analyze physical systems too large, too extreme, or too costly for a laboratory. Computational resources, which have been increasing exponentially, allow for novel high resolution models. Advancements in mathematics, computer science, and the sciences have led to interdisciplinary ventures where methods are derived, designed, and tuned for specific applications. This work is an embodiment of the interaction across skill sets and knowledge bases. Specifically, this thesis connects mathematical physics, numerical analysis, computer science, and geophysics to implement an algorithm for simulating physical behavior at new larger scales.

The thesis uses the Fast Multipole Boundary Element Method to simulate the flow of and interaction between multiple fluids. The Boundary Element Method is specifically chosen for its ability to model sharp interfaces between fluids more accurately than domain-based numerical methods. The Fast Multipole Method enables simulations to scale from the current state of handling several fluids to the presented work involving thousands.

I divide my work into five chapters. Chapter 1 provides motivation for the work and an overview of the research. Chapter 2 presents governing equations, numerical methods, and acceleration techniques used in the Fast Multipole Boundary Element Method. Chapters 3 & 4 are derived from a two part article, *Development of anisotropic texture in deforming partially molten aggregates I: Theory and fast multipole boundary element method* and *Development of anisotropic texture in deforming*

partially molten aggregates II: Implications for the lithosphere-asthenosphere boundary, submitted to the *Journal of Geophysical Research*. The chapters use numerical experiments and analysis related to the microstructure for the Earth's upper mantle to make predictions about the microstructure based on seismic measurements. Chapter 5 uses the numerical implementation to model the evolution, coalescence, and anisotropy of large structures located deep in the Earth's mantle.

Dedication

To Joanna

Acknowledgments

Graduate school has been a wonderful journey filled with the euphoria of discovery and vigor of growth. There are numerous individuals who have stood by me through my journey. Their encouragement, motivation, love, support, and dedication is worth a lifetime of gratitude and recognition.

First and foremost, I would like to thank my advisor, Professor Saswata Hier-Majumder. Like many great things in life, our research relationship grew from a chance meeting early in my graduate career. From letting me sit in on his class during my first year, to helping me find rewarding problems at the junction of mathematics, computer science, and geophysics, his guidance has helped me overcome challenges, better myself, and lead a more rewarding graduate career than I ever thought possible. His intellectual motivation and mentorship guided me through my graduate career. More than an academic advisor, Sash's and his family's generosity and hospitality over the years has taught me how to continually better myself personally, as well as academically.

I owe my peers in the Applied Mathematics & Scientific Computation program many thanks. We have worked through graduate school together, helping each other and exploring our academic curiosities. We also helped each other remember the importance of life outside graduate school. Whether social events, sports, or just casual conversations on the bus, we forged great friendships that will last a lifetime. I would especially like to thank Alex Cloninger for his friendship over the years. We were in for quite a wonderful journey neither of us fully expected when we first

started.

The staff in Applied Mathematics & Scientific Computation department have been instrumental in the degree process. Specifically, Alverda McCoy was incredibly helpful with the required paperwork, forms, and submissions. Her aid allowed me to spend countless more hours on academics rather than administrative tasks.

My family has played a tremendous role in my life. My father and mother, Ken and Cheryl Drombosky, gave me the encouragement and resources to explore my curiosities. I cannot overstate the unconditional support they have given me as I have moved from one stage of life to the next. I have also been fortunate to have my grandparents Martin and Shirley Gartner very much in my life from a young age. Their love and wisdom have taught me to always appreciate both the opportunities and challenges in life.

Finally, my deepest thanks go to my wife, Joanna Kreiselman. She started off by my side in graduate school as my girlfriend, then fiancée, and now wife. Her support and dedication are unwavering, and her desire for me to achieve my dreams is something I am incredibly fortunate to have in my life. With Joanna, I have a partner who encourages me to be the best I can possibly be in every dimension of life. So much of what I have done would not have been possible without her.

Table of Contents

List of Tables ix

List of Figures x

List of Abbreviations xvi

1 Introduction 1

2 Governing Equations and Numerical Methods 6
- 2.1 Governing equations . . . 7
- 2.2 Boundary Integral Equations . . . 8
  - 2.2.1 Single domain . . . 9
  - 2.2.2 Multiple domains . . . 14
  - 2.2.3 Boundary conditions . . . 18
  - 2.2.4 Nondimensionalization . . . 21
- 2.3 Discretization . . . 24
  - 2.3.1 Geometry . . . 25
  - 2.3.2 Linear system . . . 27
- 2.4 Fast Multipole Method . . . 30
  - 2.4.1 Far-field expansions . . . 32
  - 2.4.2 Near-field expansions . . . 35
  - 2.4.3 Domain partitioning . . . 37
- 2.5 Validation and benchmarking . . . 39
  - 2.5.1 Hadamard-Rybczyñski analytical solution . . . 40
  - 2.5.2 Asymptotic scaling . . . 42

3 Development of Anisotropic Contiguity in Deforming Partially Molten Aggregates I: Theory and Fast Multipole Boundary Element Method 47
- 3.1 Introduction . . . 47
- 3.2 Model . . . 51
  - 3.2.1 Governing equations . . . 51
  - 3.2.2 Setup for numerical experiments . . . 57
  - 3.2.3 Post-processing . . . 59

3.2.4 Numerical methods . . . 62
3.3 Results . . . 65
3.3.1 Pure shear deformation . . . 67
3.3.2 Simple shear deformation . . . 71
3.4 Discussion . . . 78
3.4.1 Trade-offs in selection of parameters . . . 78
3.4.2 Comparison with previous results . . . 79
3.5 Conclusion . . . 80

4 Development of Anisotropic Contiguity in Deforming Partially Molten Aggregates II: Implications for the Lithosphere-Asthenosphere Boundary 81
4.1 Introduction . . . 81
4.2 Methods . . . 83
4.2.1 Numerical model . . . 84
4.2.2 Calculation of shear wave speed and anisotropy . . . 86
4.3 Development of anisotropy . . . 89
4.3.1 Development of anisotropic contiguity . . . 90
4.3.2 Development of seismic anisotropy . . . 94
4.4 Implications for melting in the LAB . . . 98
4.5 Conclusion . . . 102

5 Evolution of Anisotropy in Migrating Ultralow-Velocity Zones 103
5.1 Introduction . . . 103
5.2 Model . . . 106
5.3 Simulations . . . 113
5.4 Results . . . 115
5.5 Discussion . . . 124
5.5.1 The role of buoyancy . . . 124
5.5.2 Strain and anisotropy within the ULVZ . . . 126
5.6 Conclusion . . . 128

6 Conclusion 130

A Resolving the Stokes' Paradox 133

B Tabular data from figures 135

List of Tables

2.1 Parallel scaling analysis of the FMM matrix-vector multiplication for the Stokeslet and Stresslet matrices. The time for a single thread measured in seconds is in the T_1 column. We set the number of threads $T_{max} = 24$, the maximum number of threads that can simultaneously issue through HT. The efficiency E_p measures the efficiency for the number of physical cores for $c = 12$. 46

3.1 Parameter space for the simulations. The evolution of the grain-melt aggregate is simulated for each type of shearing, six capillary numbers, and four viscosity ratios for a total of 52 simulations. . . . 59

4.1 Parameters for fit to the reduction in shear wave speed $\delta V_{Si}(i = x, y)$ as a function of strain in pure and simple shear experiments. The equation for the fit is $\delta V_{Si} = p_1\epsilon + p_2\epsilon^2$, where ϵ is either the shortening or the shear strain. 96

5.1 Summary of parameters used in simulations. At the LLSVP-mantle interface, the viscosity ratio and compositional Rayleigh number are set to zero. The buoyancy neutral simulations set $\mathcal{R}_p = 0$ at the LLSVP-ULVZ interface. The boundary conditions at the LLSVP-mantle interface are given by (5.5). 115

B.1 Data from Figure 4.2 135
B.2 Data from Figure 4.3 136
B.3 Data from Figure 4.4 137
B.4 Data from Figure 4.5 138

List of Figures

2.1 The original domain, Ω, has an ϵ-ball centered at $\boldsymbol{x}_0$, removing the singularity from the new domain, Ω'. The boundary of the original domain is labeled Γ, and the boundary of the ϵ-ball is labeled Γ_ϵ. The vectors along the boundaries represent the direction of the unit normal vector pointing outward from Ω'. 13
2.2 The portion of the boundary $\Gamma_{p,\epsilon}$ of the larger boundary Γ_p, which separates the p-th fluid from the suspension. The unit normal vector to the boundary is represented by $\hat{\boldsymbol{n}}$, and the vector $\boldsymbol{t}$ is the unit vector tangent to the boundary of $\Gamma_{p,\epsilon}$ on the fluid interface. 19
2.3 Possible arrangements for a geometry containing multiple fluids with various properties contained within an infinite suspending fluid, Ω_s. The different domains may have the same physical properties (denoted by color) as Ω_1 and Ω_4, or different properties as with Ω_2 and Ω_3. A bounded fluid may be completely contained within another bounded fluid as is the case with Ω_3 and Ω_2. 25
2.4 Discretization of the p-th fluid interface, Γ_p. The nodes are ordered counterclockwise with cyclic indexing used for convenience. The e-th boundary element of the fluid is denoted $\Gamma_{p,e}$ and is the segment between $\boldsymbol{x}_{p,e}$ and $\boldsymbol{x}_{p,e+1}$. 26
2.5 Geometry of the axis-symmetric translating sphere with radius $r = a$ in spherical coordinates. The fluids are symmetric about the $\phi = 0$ axis, hence the lack of the azimuthal angle in the geometry. The polar angle is measured from the left edge of the sphere. The exterior fluid is set to translate from right to left, over and under the sphere. . . . 41
2.6 The blue and red dots represent the radial and tangential components of the velocity of a settling viscous drop obtained from solving BIE (2.37) with $\lambda = 1$, $\mathcal{R} = 3.75$, and $a = 1$ for 100 poles evenly distributed along the boundary. The blue and red lines represent the radial and tangential components of the analytical velocity given by the Hadamard-Rybczyñski solution. Both values are given with respect to the angle θ, which represents the counterclockwise angle from the point to the negative y axis. 43
2.7 The black line represents the relative error between the numerical solution to the translating drop problem with N nodes and $2N$ nodes. The dashed red line is $\mathcal{O}\left(N^{-2.5}\right)$. There is excellent agreement until the error drops below 10^{-9}, which is to be expected as the iterative solver stops refining when the residual in the solution is less than 10^{-9}. 44

2.8 Asymptotic scaling of the FMM matrix-vector multiplication for the Stokeslet (red) and Stresslet (blue) matrices. Explicit timing measurements are marked with a dot, and the black dashed line represents linear scaling. 45

3.1 Setup for numerical experiments. (a) Initial geometry of a grain surrounded by six other grains and interstitial melt in gray at three grain junctions. The unit normal to the grain interface $\hat{n}_k(\boldsymbol{x})$, the contact function χ, and the ψ_{xx} component of the contiguity tensor are also shown in the diagram. Viscosity of the melt is μ_m, while that of the grain is $\lambda\mu_m$. (b) The initial configuration of the entire aggregate prior to the pure shear experiment. The aggregate consists of 1200 grains arranged in 40 rows and 30 columns. The red lines indicate the imposed external flow. (c) The initial configuration for simple shear experiment. The aggregate consists of 900 grains arranged in 10 rows and 90 columns. The sense of applied shear, as depicted by the bold red arrows, is dextral. 66

3.2 (a) Comparison between the deformation of a low viscosity ratio, $\lambda = 1.0$, grain-melt aggregate at the beginning and end of a simulation in a pure shear flow. The aggregate is colored blue at the start of the evolution and red at the end. Bounding boxes are added to emphasize the overall deformation of the aggregate. (b) A sample grain-melt patch with low viscosity ratio, $\lambda = 1.0$, at the end of a simulation in a pure shear flow. The gray areas between the grains represent the melt. (c) Comparison between the deformation of a high viscosity ratio, $\lambda = 50.0$, grain-melt aggregate at the beginning and end of a simulation in a pure shear flow. The aggregate is colored blue at the start of the evolution and red at the end. Bounding boxes are added to emphasize the overall deformation of the aggregate. (d) A sample grain-melt patch with low viscosity ratio, $\lambda = 50.0$, at the end of a simulation in a pure shear flow. The gray areas between the grains represent the melt. 68

3.3 Streamlines indicating flow velocities within the grains and the melt pocket. In the top panel, streamlines (a) at the onset and (b) at the end of the numerical experiment are drawn for $\lambda = 1$ and $\mathcal{C}a = 1$. In the lower panel, streamlines (a) at the onset of deformation and (b) at the end of deformation are drawn for $\lambda = 50$ and $\mathcal{C}a = 1$. The streamlines are colored by the magnitude of dimensionless velocity. . 70

3.4 (a) and (b) Values of deformation and anisotropy in the contiguity tensor at the start, $t = 0.2$, of a simulation. (c) and (d) Values of deformation and anisotropy in the contiguity tensor at the end, $t = 1.0$, of a simulation. All subfigures are from a pure shear simulation with $\mathcal{C}a = 1.0$ and $\lambda = 1.0$. A heat map is used to show the values of grain properties for a selection of inner grains of the grain-melt aggregate. (a) and (c) show the value of differential shortening, $D = (L-B)/(L+B)$, for each grain, where L is the length of the major axis and B is the length of the minor axis of the grain. (b) and (d) show anisotropy of the contiguity tensor as measured by the ratio between the normal components of the contiguity tensor, ψ_1/ψ_2. The gray patches between the grains and gray area surrounding the aggregate represent the melt. 72

3.5 (a) Comparison between the deformation of a low viscosity ratio, $\lambda = 1.0$, grain-melt aggregate at the beginning and end of a simulation in a pure shear flow. The aggregate is colored blue at the start of the evolution and red at the end. The top right portion of (a) shows a sample grain-melt patch with low viscosity ratio, $\lambda = 1.0$, at the end of a simulation in a pure shear flow. The gray areas between the grains represent the melt. (c) Comparison between the deformation of a high viscosity ratio, $\lambda = 50.0$, grain-melt aggregate at the beginning and end of a simulation in a pure shear flow. The aggregate is colored blue at the start of the evolution and red at the end. The top right portion of (b) shows a sample grain-melt patch with low viscosity ratio, $\lambda = 50.0$, at the end of a simulation in a pure shear flow. The gray areas between the grains represent the melt. 73

3.6 Streamlines indicating flow velocities within the grains and the melt pocket. In the top panel, streamlines (a) at the onset and (b) at the end of the numerical experiment are drawn for $\lambda = 1$ and $\mathcal{C}a = 1$. In the lower panel, streamlines (c) at the onset of deformation and (d) at the end of deformation are drawn for $\lambda = 50$ and $\mathcal{C}a = 1$. The streamlines are colored by the magnitude of dimensionless velocity. . 74

3.7 (a) and (b) Values of deformation and anisotropy in the contiguity tensor at the start, $t = 0.2$, of a simulation. (c) and (d) Values of deformation and anisotropy in the contiguity tensor at the end, $t = 1.0$, of a simulation. All subfigures are from a simple shear simulation with $\mathcal{C}a = 1.0$ and $\lambda = 1.0$. A heat map is used to show the values of grain properties for a selection of inner grains of the grain-melt aggregate. (a) and (c) show the value of differential shortening, $D = (L - B)/(L + B)$, for each grain, where L is the length of the major axis and B is the length of the minor axis of the grain. (b) and (d) show anisotropy of the contiguity tensor as measured by the ratio between the normal components of the contiguity tensor, ψ_1/ψ_2. The gray patches between the grains and gray area surrounding the aggregate represent the melt. 75

3.8 (a) Best fit between the anisotropy of the contiguity tensor, ψ_1/ψ_2, and differential shortening, D, for the pure shear simulations. The blue dots represent measurements of grains from simulations where $\lambda = 50.0$ and $\mathcal{C}a = 1.0$. The red dots represent measurements of grains from simulations where $\lambda = 1.0$ and $\mathcal{C}a = 1.0$. The relationship is given by $\psi_1/\psi_2 \sim \exp(-3.909D^2 - 1.005D)$ with $R^2 = 0.998$. (b) A zoomed in view of the high viscosity data points from (a). 77
3.9 Development of anisotropic textures in pure shear experiments. (a) Plot of anisotropy in contiguity ψ_1/ψ_2 as a function of bulk strain for viscosity ratios $\lambda = 1$ (red squares) and $\lambda = 50$ (blue circles). (b) Plot of differential shortening as a function of bulk strain for viscosity ratios $\lambda = 1$ (red squares) and $\lambda = 50$ (blue circles). 79

4.1 Microstructure of a small section from the deforming aggregate. On the left, the undeformed aggregate is shown. The ψ_{xx} component of the contiguity tensor is illustrated on a grain boundary of the undeformed aggregate. On the right, microstructures resulting from pure shear (top) and simple shear (bottom) deformation are shown. 90
4.2 Development of anisotropic contiguity in pure shear. (a) Plot of the magnitude of contiguity, ψ, and the components ψ_{xx} and ψ_{yy} as a function of shortening. Each data point is averaged over 1200 grains in the numerical experiment. Width of the shaded region represents the range of contiguity reported by *Takei* [2005] for comparable melt volume fractions. (b) Ratio between the two principal components of contiguity (ψ_1/ψ_2) and the ratio between the ψ_{xx} and ψ_{yy} components. The data sets are practically indistinguishable and overlie each other. 91
4.3 Development of anisotropic contiguity during simple shear. Each data point is averaged over 900 grains in the numerical experiment. (a) Plots of magnitude of contiguity ψ, and the components ψ_{xx} and ψ_{yy} as a function of shear strain. Width of the shaded region represents the range of contiguity reported by *Takei* [2005] for comparable melt volume fractions. (b) Ratio of the two principal components of contiguity (ψ_1/ψ_2) and the ratio between the ψ_{xx} and ψ_{yy} components. . 93
4.4 Development of shear wave anisotropy as a function of strain in pure shear. Variations in the wave speed of a wave traveling out of the plane of deformation with a polarization parallel to the (a) x axis, δV_{Sx}, and (b) y axis, δV_{Sy}, normalized by the wave speed in the isotropic aggregate, V_{eq}. The blue lines are polynomial fits to the data. Parameters for the fit and the fitting function are reported in Table 4.1. (c) Total seismic anisotropy, difference between the two polarizations of the shear wave, normalized by V_{eq}. The strain on the horizontal axis is shortening. Each data point represents an average of the 1200 grains. 95

4.5 Development of shear wave anisotropy as a function of strain in simple shear. Variations in the wave speed of a wave traveling out of the plane of deformation with a polarization parallel to the (a) x axis, δV_{Sx}, and (b) y axis, δV_{Sy}, normalized by the wave speed in the isotropic aggregate, V_{eq}. The blue lines are polynomial fits to the data. Parameters for the fit and the fitting function are reported in Table 4.1. (c) Total seismic anisotropy, difference between the two polarizations of the shear wave, normalized by V_{eq}. The strain on the horizontal axis is the shear strain. Each data point represents an average of the 900 grains. 97

4.6 (a) A cartoon identifying the components of anisotropy and stress in an aggregate deformed by pure shear. Also shown are two waves, V_{Sx} and V_{Sy}, that travel out of the plane of deformation and are polarized in the x and y directions, respectively. The component of contiguity, ψ_{xx}, is reduced by predominant wetting of the grain boundaries perpendicular to the x direction. (b) Two illustrative cases resulting from preferential wetting of either horizontal or vertical grain boundaries. When the grain boundary melt films are horizontal, $V_{SH} > V_{SV}$, while the picture is reversed for vertical melt films. 98

4.7 (a) Effect of melt geometry in shear wave speed reduction in the LAB. The gray shaded region represents shear wave speed profiles varying between potential temperatures of 1300 K and 1500 K, from *Xu et al.* [2008]. The temperature sensitive top and bottom of the melting zones are marked by broken horizontal lines. The blue shaded profiles represent shear wave speed reduction caused by 2 vol% melt in tubules for dihedral angles of 5° and 25°. (b) The thin blue curves correspond to reduction in the shear wave speed of the reference mantle if the 0.1 vol% melt is distributed in grain boundary tubules. The red regions represent reduction in the shear wave velocity if the same volume fraction of melt is distributed in thin grain boundary films. The width of the region represents the variations in the aspect ratio of the film. For the melt fraction of 0.1 vol%, the observed 5% reduction in shear wave velocity can be explained by melt films of aspect ratio 0.002, created by deformation. (c) Profiles of seismic anisotropy resulting from the distribution of melt in grain boundary films. If the films are oriented horizontally, the melting zone will depict an anisotropy of +4%. The sign of anisotropy will reverse if the melt is organized in vertical films. 100

5.1 Evolution of circular ULVZ reservoirs placed in the LLSVP. The five snapshots show the evolution of the system between 0 and 12 Ma. The streamlines are colored by the magnitude of the velocity with light blue corresponding to 1 cm/yr and dark red to 3 cm/yr. The ULVZ patches are separated from the LLSVP by a black outline and shaded in gray. 116

5.2 Evolution of rectangular ULVZ reservoirs with rounded corners placed in corners of the LLSVP. The five snapshots show the evolution of the system between 0 and 8.75 Ma. The streamlines are colored by the magnitude of the velocity with light blue corresponding to 1 cm/yr and dark red to 2 cm/yr. The ULVZ patches are separated from the LLSVP by a black outline and shaded in gray. 118
5.3 Change in height of the ULVZ reservoir as it climbs the wall of the LLSVP in Figure 5.2 is plotted by the solid line. The dashed line represents no change in height, i.e., steady state. The derivative is passed through a triangle smoothing filter to reduce noise in the measurement. 120
5.4 Evolution of ULVZ reservoirs wedged into the corners of the LLSVP. The five snapshots show the evolution of the system between 0 and 5 Ma. The streamlines are colored by the magnitude of the velocity with light blue corresponding to 1 cm/yr and dark red to 2 cm/yr. The ULVZ patches are separated from the LLSVP by the black outline and shaded in gray. The last snapshot highlights the streamlines, in green and orange, completely within the ULVZ indicating a steady state geometry has been achieved. 122
5.5 Change in height of the ULVZ reservoir as it falls down the wall of the LLSVP in Figure 5.4 is plotted in the solid line. The dashed line represents no change in height, i.e., steady state. The derivative is passed through a triangle smoothing filter to reduce noise in the measurement. 123
5.6 Evolution of buoyancy free, i.e., $\mathcal{R}_p = 0$, ULVZ reservoirs. The streamlines are colored by the magnitude of the velocity with light blue corresponding to 0 cm/yr and dark red to 1 cm/yr. a) and b) initially started in the same condition as Figure 5.2 at 0 Ma after 8.75 Ma and 15 Ma, respectively. c) and d) initially started in the same condition as Figure 5.4 at 0 Ma after 5 Ma and 10 Ma. The buoyancy neutral ULVZs are completely lifted up the wall of the LLSVP. . . . 125
5.7 Strain tensor throughout the LLSVP for a) the end of the first simulation where the ULVZs were initially distributed in the center of the LLSVP and swept into the corner and b) the end of the third simulation where the ULVZ was initially a triangle wedge that settled into a steady state geometry. The strain is colored based on the magnitude of the principal dimension of deformation. The black lines represents the angle of melt channels forming within the ULVZs. 127

List of Abbreviations

BEM	Boundary Element Method
BIE	Boundary Integral Equation
DOF	Degrees of Freedom
FDM	Finite Difference Method
FEM	Finite Element Method
FMBEM	Fast Multipole Boundary Element Method
FMM	Fast Multipole Method
FVM	Finite Volume Method
HR	Hadamard-Rybczyñski
HT	Intel®Hyper-Threading architecture
LAB	Lithosphere-Asthenosphere Boundary
LLSVP	Large Low Shear Velocity Province
LPO	Lattice Preferred Orientation
MKL	Intel®Math Kernel Library
PDE	Partial Differential Equation
RIM	Radial Integration Method
RK4	Runge-Kutta Order 4
ULVZ	Ultralow-Velocity Zone

Chapter 1: Introduction

Creeping motion of viscous fluids, governed by the conservation of mass, momentum, and energy, controls the pattern and evolution of flow in a wide variety of natural situations and industrial applications. For example, microstructural evolution of partially molten rocks, deformation of red blood cells near capillary walls, and micro-fluid flow in chemical engineering are governed by the interaction between a large number of viscous particles embedded in a viscous medium. While governed by the classical Partial Differential Equations (PDEs) of Stokes flow, the many-body interaction inherent to these situations renders simulating such flows computationally challenging.

In geophysical modeling, similar to many other applications, information regarding the shape of each participating particle or grain is required. While domain discretization methods such as Finite Element Method (FEM), Finite Difference Method (FDM), or Finite Volume Method (FVM) can be used to provide scalable and stable numerical implementation of flows within a domain, tracking the shapes of multiple interfaces in a multiphase flow is not computationally feasible in these techniques.

The Boundary Element Method (BEM) addresses the issue of dynamic inter-

action between adjacent particles, leading to their deformation, by converting the governing PDEs into a set of Boundary Integral Equations (BIEs) on the interface of each particle. By coupling the BIEs with level set equations that govern the evolution of each particle shape, we model the interaction between a number of particles and their resulting deformation. While the BIE reduces the dimension of the problem by moving the calculation from the domain to the boundary, the calculations become computationally expensive as the number of particles grows, increasing the Degrees of Freedom (DOFs) of the discretized set of algebraic equations. The computational expense of the BEM poses a challenge in carrying out simulations with a large number of grains. The work in this thesis resolves this issue by implementing the Fast Multipole Boundary Element Method (FMBEM), which reduces the computational cost of solving the dense system of linear equations resulting from the discretization of the BIE by employing fast multipole expansions.

This is the first collection of work to use the FMBEM to address rock physics with direct geophysical applications. We follow a majority of computational geophysical work and use two-dimensional models to represent three-dimensional physical systems. The results are often representative of higher dimensional behavior in addition to being computationally less demanding. Comparisons between two- and three-dimensional models show qualitative similarities between results. Certainly two-dimensional models are subject to error, specifically when dealing with interface measurements. However, the novelty of our approach and current state of two-dimensional geophysical simulations makes this an acceptable choice.

Chapter 2 provides an overview of the derivation of the BEM and the numerical

methods. We present the strong form of the PDEs governing the two-dimensional flow for viscous fluids. From the dimensional PDEs, we derive dimensionless BIEs describing two-dimensional flow involving multiple viscous particles with boundary conditions appropriate for geophysical situations. We highlight the discretization of the geometry and BIEs. Finally, we describe the application of the Fast Multipole Method (FMM) acceleration technique to the BIE. The numerical approximation technique is central to our ability to simulate the high resolution behavior of many fluids in later chapters.

In the Earth's deep interior, rocks deform in a time-dependent, viscous manner. If partially molten, the distribution of the melt within the network of mineral grains is highly sensitive to the state of stress. Chapter 3 presents simulations of the evolution of melt distribution in a partially molten rock under an applied stress. This chapter is under revision as the *Journal of Geophysical Research* with the title "Development of Anisotropic Contiguity in Deforming Partially Molten Aggregates I: Theory and Fast Multipole Boundary Element Method" [*Drombosky and Hier-Majumder*, 2014]. The geometry of melt distribution strongly influences the macroscopic physical properties through the fractional area of intergranular contact, contiguity. Contiguity controls the elastic strength of the grain network in the partially molten aggregate, influencing the speed of seismic waves traveling through the aggregate.

In this chapter, we study the influence of matrix deformation on the contiguity of an aggregate. We employ an FMBEM model that tracks the evolution of grain shape and contiguity during deformation. We carry out a pure shear deformation of

an aggregate of 1200 grains up to 47% shortening and a simple shear deformation of 900 grains up to a shear strain of 0.75. Our results demonstrate that the initially isotropic, scalar contiguity becomes strongly anisotropic during deformation. We also observe that the differential shortening, the normalized difference between the major and minor axes of grains, is inversely related to the ratio between the principal components of the contiguity tensor. In pure shear, the principal components of the contiguity tensor remain parallel to the irrotational principal axes of the applied strain. In simple shear, however, the principal components of the contiguity tensor rotate continually during the course of deformation in this study.

As the contiguity of partially molten rocks becomes anisotropic, the speed of seismic waves traveling through these rocks varies based on their directions of propagation and polarization, a phenomenon called seismic anisotropy. In Chapter 4, we calculate the seismic anisotropy resulting from melt redistribution during pure and simple shear deformation. This chapter is under revision as the *Journal of Geophysical Research* with the title "Development of Anisotropic Contiguity in Deforming Partially Molten Aggregates II: Implications for the Lithosphere-Asthenosphere Boundary" [*Hier-Majumder and Drombosky*, 2014]. During deformation, the melt is expelled from tubules along three grain corners to films along grain edges. The initially isotropic contiguity becomes anisotropic due to deformation. Consequently, the component of contiguity evaluated on the plane parallel to the axis of maximum compressive stress decreases. In pure shear deformation, the principal contiguity directions remain stationary while they rotate during simple shear. The ratio between the principal components of the contiguity tensor decreases from 1 in an undeformed

aggregate to 0.1 after 45% shortening in pure shear and to 0.3 after a shear strain of 0.75 in simple shear. In both pure and simple shear experiments, anisotropy in the shear wave velocity increases with the strain in a strongly nonlinear fashion. In pure shear deformation, the steady state microstructure produces nearly 3% anisotropy between shear waves vibrating perpendicular and parallel to the planes of melt films. We demonstrate that the observed global shear wave anisotropy and shear wave speed reduction of Earth's Lithosphere-Asthenosphere Boundary (LAB) are best explained by 0.1 vol% partial melt distributed in horizontal films created by deformation. Chapters 3 and 4 are currently in revision in the *Journal of Geophysical Research*.

The bottom of the Earth's mantle is marked by a number of dynamic structures. Two large antipodal structures in the lower mantle, geographically located beneath the Pacific Ocean and Africa and termed Large Low Shear Velocity Provinces (LLSVPs), are caused by thermal and chemical anomalies in the mantle. Along the bottom periphery of the LLSVPs, a patchwork of dense, low-viscosity structures, termed Ultralow-Velocity Zones (ULVZs), have been observed in seismic records. In Chapter 5, we simulate the evolution of two-dimensional ULVZ patches driven by a cavity-like flow in the LLSVP. Driven by a balance between buoyancy forces and entrainment by circulation within the LLSVP, we find that only high density ULVZs accumulate near the bottom corner of the LLSVPs. In the absence of a density contrast, the ULVZs are stirred and mixed within the LLSVP such that they won't be detectable by current seismic methods. We also find the dominant strain within the ULVZ patches varies based on the location of the ULVZ within the LLSVP.

Combined with the results from Chapters 3 and 4, we predict the nature of seismic anisotropy will also be distinct based on the locations of the ULVZs.

Chapter 2: Governing Equations and Numerical Methods

The Boundary Element Method (BEM) provides a boundary-only technique for solving Partial Differential Equations (PDEs) describing the flow of multiple viscous fluids through a collection of Boundary Integral Equations (BIEs). The BIEs are discretized, leading to a linear system of algebraic equations, which can be solved numerically. Naïve implementation of the BEM scales poorly for large simulations. The Fast Multipole Method (FMM) approximation technique accelerates the BEM, allowing the method to be applied to high resolution simulations involving many viscous fluids.

This chapter provides an overview of the Stokes flow equations and Fast Multipole Boundary Element Method (FMBEM) for the geophysical simulations presented in Chapters 3, 4, and 5. Section 2.1 presents the strong form of the governing equations for Stokes and creeping flow. Section 2.2 provides the derivation of a collection of BIEs used in the BEM. We provide an overview of discretization in Section 2.3. Section 2.4 presents details on the application of the FMM to the BEM for Stokes flow. Finally, Section 2.5 displays results of validation and analysis of the algorithm.

2.1 Governing equations

In a viscous, incompressible, creeping fluid, conservation of mass leads to the PDE,

$$u_{i,i}(\boldsymbol{x}) = 0 \qquad \boldsymbol{x} \in \Omega, \tag{2.1}$$

where u_i is the i-th component of velocity. In the absence of acceleration, the momentum conservation equation arises from a balance between dynamic pressure, viscous deformation, and body forces, leading to

$$-P_{,i}(\boldsymbol{x}) + \mu u_{i,jj}(\boldsymbol{x}) + \rho g_i = 0 \qquad \boldsymbol{x} \in \Omega, \tag{2.2}$$

where P is the pressure, u_i is the velocity, μ is the constant viscosity, ρ is the density of the fluid, and g_i is the gravity. Equation (2.2) is valid for any point $\boldsymbol{x}$ in the open set Ω.

To convert the momentum conservation equation (2.2) into a BIE, it is useful to introduce the stress tensor, σ_{ij}, defined as

$$\sigma_{ij} = -\delta_{ij} P + \frac{\mu}{2} \left(u_{i,j} + u_{j,i} \right), \tag{2.3}$$

where δ_{ij} is the Kronecker delta function.

Differentiating (2.3) with respect to x_i and substituting into (2.2) yields the

conservation of momentum equation in the presence of a body force,

$$\sigma_{ij,i} + \rho g_j = 0, \tag{2.4}$$

which balances the forces generated from changes in the fluid stress against the force from gravitational acceleration.

The evolution of a viscous particle is described using the kinematic condition. Let $\Omega' \subset \Omega$ with interface $\Gamma' = \partial\Omega'$ defined by the level set $F(\boldsymbol{x}, t) = 0$. Incompressibility of the fluid dictates that the volume of the particle must remain constant while the shape changes due to deformation, leading to

$$F_{,t}(\boldsymbol{x}, t) + u_i(\boldsymbol{x}, t)F_{,i}(\boldsymbol{x}, t) = 0. \tag{2.5}$$

The gradient of the level set $F_{,i}$ is in the direction of the outward-facing normal vector, by choosing $F(\boldsymbol{x}, t) < 0$ if $\boldsymbol{x} \in \Omega'$ and $F(\boldsymbol{x}, t) > 0$ if $\boldsymbol{x} \notin \overline{\Omega'}$.

2.2 Boundary Integral Equations

The BEM requires the development of BIEs from the governing PDEs for mass and momentum conservation. The following sections present the steps taken to developing this BIE from the PDEs. Section 2.2.1 develops the BIEs for a homogeneous fluid in a single domain. The BIEs for the special case multipole domains, each containing a homogeneous fluid, are derived from the single domain equations in Section 2.2.2. Section 2.2.3 describes the boundary conditions applied at the in-

terface between distinct fluids. Section 2.2.4 covers nondimensionalization schemes used, based on boundary conditions, to more amicably map physical problems to a computer simulation.

2.2.1 Single domain

The BIE for a homogeneous viscous fluid relates the stresses and velocities along the boundary. Consider two solutions to the governing PDE (2.2) designated as u_i and u'_i, respectively. The reciprocity equation relates these two velocities with their corresponding stress tensors, σ_{ij} and σ'_{ij}, by [*Pozrikidis*, 1991]

$$u'_{i,j}(\boldsymbol{x})\sigma_{ij,j}(\boldsymbol{x}) - u_{i,j}(\boldsymbol{x})\sigma'_{ij,j}(\boldsymbol{x}) = 0 \qquad \boldsymbol{x} \in \Omega. \tag{2.6}$$

Integrating (2.6) over the domain and applying Gauss's theorem produces a boundary integral relationship between the two solutions:

$$0 = \int_\Gamma \left[u'_i(\boldsymbol{x})\sigma_{ij}(\boldsymbol{x}) - u_i(\boldsymbol{x})\sigma'_{ij}(\boldsymbol{x})\right] \hat{n}_j(\boldsymbol{x})\, \mathrm{d}\Gamma, \tag{2.7}$$

where $\Gamma = \partial\Omega$ is the boundary of the domain and $\hat{n}_i$ is the outward-facing unit normal vector. The integral reciprocity equation in (2.7) is the first step toward deriving the BIE for the Stokes flow equations. Next, carefully chosen velocity and stress fields for the prime fluid in (2.7) extract information about the unknown flow.

A canonical choice for the prime solution is the fundamental solution to the

forced Stokes flow equation,

$$-P_{,i}(\boldsymbol{x}) + \mu u_{i,jj}(\boldsymbol{x}) + g_i \delta(\boldsymbol{x} - \boldsymbol{x}_0) = 0 \qquad \boldsymbol{x} \in \Omega, \tag{2.8}$$

where δ is the Dirac delta function representing a point source force at $\boldsymbol{x}_0$, an arbitrary location that may or may not be in the domain. Because the Dirac delta is a singularity distributed around $\boldsymbol{x}_0$, the point $\boldsymbol{x}_0$ is referred to as a pole point. The velocity solution to (2.8) is given by

$$u_i(\boldsymbol{x}) = \frac{1}{4\pi\mu} \mathcal{U}_{ij}(\boldsymbol{x}, \boldsymbol{x}_0) g_j, \tag{2.9}$$

where $\mathcal{U}_{ij}$ is the Green's function for the velocity. The corresponding pressure and stress are written as

$$P(\boldsymbol{x}) = \frac{1}{4\pi} \mathcal{P}_j(\boldsymbol{x}, \boldsymbol{x}_0) g_j \tag{2.10}$$

$$\sigma_{ik}(\boldsymbol{x}) = \frac{1}{4\pi} \mathcal{T}_{ijk}(\boldsymbol{x}, \boldsymbol{x}_0) g_j, \tag{2.11}$$

where $\mathcal{P}_j$ is the Green's function for the pressure and $\mathcal{T}_{ijk}$ is the Green's function for the stress. Green's functions $\mathcal{U}_{ij}$, $\mathcal{P}_j$, and $\mathcal{T}_{ijk}$ are referred to as the Stokeslet, Pressurelet, and Stresslet, respectively.

The expression for the Stokeslet depends on the domain shape and boundary conditions. For example, shear flow in a doubly periodic domain and motion of a viscous particle against a wall can modify the form of the Stokeslet tensor [*Pozrikidis*,

1990; *Li and Pozrikidis*, 1996]. Here we focus on the free-space Green's function for an infinite domain given by

$$\mathcal{U}_{ij}(\boldsymbol{x}, \boldsymbol{x}_0) = -\delta_{ij} \log(r) + \frac{\hat{x}_i \hat{x}_j}{r^2} + c_{ij}, \tag{2.12}$$

where $\hat{\boldsymbol{x}} = \boldsymbol{x} - \boldsymbol{x}_0$, $r = \|\hat{\boldsymbol{x}}\|_2$, and c_{ij} is an arbitrary constant tensor. A more detailed discussion on the choice for Green's function is given in Appendix A.

The Pressurelet and Stresslet are derived by inserting (2.12) into (2.8) and (2.3), while expressing the pressure and stress given by equations (2.10) and (2.11), respectively, leading to

$$\mathcal{P}_i(\boldsymbol{x}, \boldsymbol{x}_0) = 2\frac{\hat{x}_i}{r^2} \tag{2.13}$$

$$\mathcal{T}_{ijk}(\boldsymbol{x}, \boldsymbol{x}_0) = -4\frac{\hat{x}_i \hat{x}_j \hat{x}_k}{r^4}. \tag{2.14}$$

Next, we replace the velocity and stress in the reciprocity equation (2.6) by the expressions in equations (2.9) and (2.11), and substitute the Stokeslet and Stresslet tensors from equations (2.12) and (2.14) leading to

$$\mathcal{U}_{ij,k}(\boldsymbol{x}, \boldsymbol{x}_0)\sigma_{ik,k}(\boldsymbol{x}) - \mu u_{i,k}(\boldsymbol{x})\mathcal{T}_{ijk,k}(\boldsymbol{x}, \boldsymbol{x}_0) = 0 \qquad \boldsymbol{x} \in \Omega. \tag{2.15}$$

Here the arbitrary g_j from (2.9) and (2.11) has been dropped, resulting in a set of reciprocity equations.

Integrating (2.15) over the domain and applying Gauss's theorem to arrive at

a BIE requires extra care since the solutions composed of $\mathcal{U}_{ij}(\boldsymbol{x}, \boldsymbol{x}_0)$ and $\mathcal{T}_{ijk}(\boldsymbol{x}, \boldsymbol{x}_0)$ have a singularity at $\boldsymbol{x} = \boldsymbol{x}_0$. Three cases lead to three separate BIEs when

1. $\boldsymbol{x}_0 \notin \overline{\Omega}$, the pole point is neither in the computational domain nor on the boundary.

2. $\boldsymbol{x}_0 \in \Omega$, the pole point is in the computational domain.

3. $\boldsymbol{x}_0 \in \Gamma$, the pole point is on the boundary of the computational domain.

In the simplest case, $\boldsymbol{x}_0 \notin \overline{\Omega}$, integration over Ω and application of Gauss's theorem for (2.15) is straightforward, resulting in

$$0 = \int_\Gamma \mathcal{U}_{ij}(\boldsymbol{x}, \boldsymbol{x}_0) f_i(\boldsymbol{x}) \, \mathrm{d}\Gamma - \mu \int_\Gamma u_i(\boldsymbol{x}) \mathcal{T}_{ijk}(\boldsymbol{x}, \boldsymbol{x}_0) \hat{n}_k(\boldsymbol{x}) \, \mathrm{d}\Gamma \qquad \boldsymbol{x}_0 \notin \overline{\Omega}, \tag{2.16}$$

where $f_i = \sigma_{ik} \hat{n}_k$ is the traction along the boundary.

Each of the two integrals in equation (2.16) has a unique physical interpretation. The first integral on the right hand side, commonly called the single-layer potential, represents the distribution of the surface forces of the unknown flow field along the boundary. The second integral on the right hand side, commonly called the double-layer potential, arises from stresses at the boundary.

In the next case, we consider $\boldsymbol{x}_0 \in \Omega$. Let $\Omega_\epsilon = \mathcal{B}(\boldsymbol{x}_0, \epsilon)$ be the ball of radius ϵ centered at $\boldsymbol{x}_0$ with ϵ small enough such that $\Omega_\epsilon \subset \Omega$, as illustrated in Figure 2.1. Following the methods outlined by *Pozrikidis* [1991], we carry out the integral as $\epsilon \to 0$. Then applying the divergence theorem, boundary integral representation

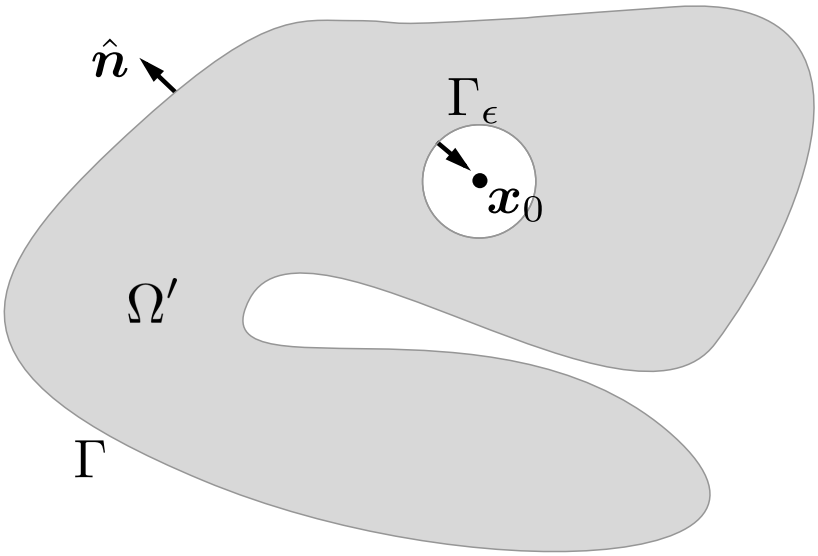

Figure 2.1: The original domain, Ω, has an ϵ-ball centered at $\boldsymbol{x}_0$, removing the singularity from the new domain, Ω'. The boundary of the original domain is labeled Γ, and the boundary of the ϵ-ball is labeled Γ_ϵ. The vectors along the boundaries represent the direction of the unit normal vector pointing outward from Ω'.

becomes

$$u_j(\boldsymbol{x}_0) = \frac{1}{4\pi\mu}\int_\Gamma \mathcal{U}_{ij}(\boldsymbol{x},\boldsymbol{x}_0) f_i(\boldsymbol{x})\,\mathrm{d}\Gamma - \frac{1}{4\pi}\int_\Gamma u_i(\boldsymbol{x})\mathcal{T}_{ijk}(\boldsymbol{x},\boldsymbol{x}_0)\hat{n}_k\,\mathrm{d}\Gamma \qquad \boldsymbol{x}_0 \in \Omega. \tag{2.17}$$

The BIE in (2.17) is used to calculate the velocity of a fluid at any point within the computational domain once the velocity at the boundary is known. We use this equation to visualize the velocity field within the fluid domain.

The final BIE arises when $\boldsymbol{x}_0 \in \Gamma$. We perform a similar analysis as in the $\boldsymbol{x}_0 \in \Omega$ case, defining the sphere of radius ϵ around the pole point. Next, we integrate (2.15) over Ω', apply Gauss's theorem, and take the limit $\epsilon \to 0$, approaching the boundary from both inside and outside the volume. Since both limits should yield

the same result as the boundary is approached, we obtain

$$u_j(\boldsymbol{x}_0) = \frac{1}{2\pi\mu}\int_\Gamma \mathcal{U}_{ij}(\boldsymbol{x},\boldsymbol{x}_0) f_i(\boldsymbol{x})\,\mathrm{d}\Gamma - \frac{1}{2\pi}\int_\Gamma^{\mathcal{PV}} u_i(\boldsymbol{x})\mathcal{T}_{ijk}(\boldsymbol{x},\boldsymbol{x}_0)\hat{n}_k(\boldsymbol{x})\,\mathrm{d}\Gamma \qquad \boldsymbol{x}_0 \in \Gamma \tag{2.18}$$

when the normal vector on Γ is continuous in a neighborhood about $\boldsymbol{x}_0$, i.e., Γ is a Lyapunov surface.

The above derivation of the Stokes flow BIEs is valid when the viscosity, density, and body force are constant throughout the domain. A more general analysis of the strong form of the PDEs is required if these terms are a function of position. The special case where μ and ρ are piecewise constant throughout the domain is covered in the next section.

2.2.2 Multiple domains

The BIEs for a fluid that has piecewise constant physical properties are developed by combining the BIEs derived for a single homogeneous fluid and enforcing boundary conditions between the fluid domains that reflect the material discontinuities. Suppose there is an infinite domain Ω_1 containing a homogeneous fluid with viscosity μ_1. Within the infinite domain is a simply- or multi-connected bounded domain Ω_2 containing a second homogeneous fluid with viscosity μ_2. We then define Γ to be the interface between the two fluids.

The no-slip boundary condition is applied at the interface, enforcing continuity

of velocity across the interface; that is,

$$u_i^{(1)}(\boldsymbol{x})\Big|_\Gamma = u_i^{(2)}(\boldsymbol{x})\Big|_\Gamma, \tag{2.19}$$

where the superscript (p) indicates the property corresponds with fluid in Ω_p. No-slip boundary conditions are used when stress generated by physical discontinuities between the two domains drives fluid velocities. This is appropriate when studying the interaction of viscous fluids.

Suppose the pole point is centered at $\boldsymbol{x}_0 \in \Omega_1$. Then, we can express this velocity both as an interior flow for Ω_1 using (2.17) and an exterior flow for Ω_2 by using equation (2.16). Combining these equations, we can obtain an integral equation for the velocity $u_j^{(1)}(\boldsymbol{x}_0)$, internal to the domain Ω_1:

$$u_j^{(1)}(\boldsymbol{x}_0) = -\frac{1}{4\pi\mu_1}\int_\Gamma \Delta f_i(\boldsymbol{x})\mathcal{U}_{ij}(\boldsymbol{x},\boldsymbol{x}_0)\,\mathrm{d}\Gamma + \frac{1-\lambda}{4\pi}\int_\Gamma u_i(\boldsymbol{x})\mathcal{T}_{ijk}(\boldsymbol{x},\boldsymbol{x}_0)\hat{n}_k\,\mathrm{d}\Gamma, \tag{2.20}$$

where $\Delta f_i = f^{(1)} - f^{(2)}$ is the interfacial stress jump and $\lambda = \mu_2/\mu_1$ is the viscosity ratio between the fluids.

Next, we repeat the same process to obtain an integral equation for the velocity $u_j^{(2)}(\boldsymbol{x}_0)$ within the domain Ω_2:

$$u_j^{(2)}(\boldsymbol{x}_0) = -\frac{1}{4\pi\mu_1\lambda}\int_\Gamma \Delta f_i(\boldsymbol{x})\mathcal{U}_{ij}(\boldsymbol{x},\boldsymbol{x}_0)\,\mathrm{d}\Gamma + \frac{1-\lambda}{4\pi\lambda}\int_\Gamma u_i(\boldsymbol{x})\mathcal{T}_{ijk}(\boldsymbol{x},\boldsymbol{x}_0)\hat{n}_k\,\mathrm{d}\Gamma. \tag{2.21}$$

Finally, we notice that when the pole point lies on the boundary, the BIE can be written in a manner similar to (2.18) using both domains Ω_1 and Ω_2. Since both velocities are equal at the boundary due to the no-slip boundary condition, we arrive at the BIE for the velocity at the interface,

$$u_j(\boldsymbol{x}_0) = \frac{2}{1+\lambda}\left[-\frac{1}{4\pi\mu_1}\int_\Gamma \Delta f_i(\boldsymbol{x})\mathcal{U}_{ij}(\boldsymbol{x},\boldsymbol{x}_0)\,\mathrm{d}\Gamma \right. \\ \left. +\frac{1-\lambda}{4\pi}\int_\Gamma^{\mathcal{PV}} u_i(\boldsymbol{x})\mathcal{T}_{ijk}(\boldsymbol{x},\boldsymbol{x}_0)\hat{n}_k\,\mathrm{d}\Gamma\right]. \tag{2.22}$$

As before, there is the assumption that Γ is a Lyapunov surface.

Equations (2.20), (2.21), and (2.22) may be generalized for an infinite suspending fluid with viscosity μ_s containing P distinct fluids where the p-th fluid has viscosity μ_p by adding the relationship between the velocity and stress along the boundary from the perspective of that particle. As before, the bounded domain of the p-th fluid Ω_p may be single- or multi-connected. In addition, a known far-field velocity, u_j^∞ can be applied to the system, leading to the BIEs

$$u_j(\boldsymbol{x}_0) = u_j^\infty(\boldsymbol{x}_0) - \frac{1}{4\pi\mu_s}\sum_{p=1}^{P}\int_{\Gamma_p}\Delta f_i(\boldsymbol{x})\mathcal{U}_{ij}(\boldsymbol{x},\boldsymbol{x}_0)\,\mathrm{d}\Gamma_p \\ +\sum_{p=1}^{P}\frac{1-\lambda_p}{4\pi}\int_{\Gamma_p} u_i(\boldsymbol{x})\mathcal{T}_{ijk}(\boldsymbol{x},\boldsymbol{x}_0)\hat{n}_k(\boldsymbol{x})\,\mathrm{d}\Gamma_p \qquad \boldsymbol{x}_0\in\Omega_s, \tag{2.23}$$

$$u_j(\boldsymbol{x}_0) = \frac{1}{\lambda_q} u_j^{\infty}(\boldsymbol{x}_0) - \frac{1}{4\pi\mu_s\lambda_q} \sum_{p=1}^{P} \int_{\Gamma_p} \Delta f_i(\boldsymbol{x}) \mathcal{U}_{ij}(\boldsymbol{x}, \boldsymbol{x}_0) \, \mathrm{d}\Gamma_p$$
$$+ \sum_{p=1}^{P} \frac{1-\lambda_p}{4\pi\lambda_q} \int_{\Gamma_p} u_i(\boldsymbol{x}) \mathcal{T}_{ijk}(\boldsymbol{x}, \boldsymbol{x}_0) \hat{n}_k(\boldsymbol{x}) \, \mathrm{d}\Gamma_p \qquad \boldsymbol{x}_0 \in \Omega_q, \tag{2.24}$$

$$u_j(\boldsymbol{x}_0) = \frac{2}{1+\lambda_q} \left[u_j^{\infty}(\boldsymbol{x}_0) - \frac{1}{4\pi\mu_s} \sum_{p=1}^{P} \int_{\Gamma_p} \Delta f_i(\boldsymbol{x}) \mathcal{U}_{ij}(\boldsymbol{x}, \boldsymbol{x}_0) \, \mathrm{d}\Gamma_p \right.$$
$$\left. + \sum_{p=1}^{P} \frac{1-\lambda_p}{4\pi} \int_{\Gamma_p}^{\mathcal{PV}} u_i(\boldsymbol{x}) \mathcal{T}_{ijk}(\boldsymbol{x}, \boldsymbol{x}_0) \hat{n}_k(\boldsymbol{x}) \, \mathrm{d}\Gamma_p \right] \qquad \boldsymbol{x}_0 \in \Gamma_q, \tag{2.25}$$

for the cases where the pole point is in the infinite suspending fluid, Ω_s; in a bounded fluid, Ω_p; and on a fluid interface, Γ_p.

The three BIEs (2.23), (2.24), and (2.25) are the most general integral equations for multiple viscous fluids with no-slip boundary conditions. Although the equations were derived for bounded fluids that directly interface with an infinite suspending fluid, the equations support nested fluids with minor changes to the definition of the interfacial stress jump, viscosity ratio, and direction of normal vector.

Two steps remain before discretizing the BIEs and obtaining numerical solutions. First, Section 2.2.3 derives the interfacial stress jump based on the physical model of the interface and stresses that arise from discontinuities of physical properties across the interface. Second, the BIEs in this section are dimensional; that is, the variables have units attached to them. The equations may be used to describe fluids from physical systems that differ by orders of magnitude. Section 2.2.4 covers the derivation of dimensionless BIEs that have normalized length and time scales

appropriate for numerical solvers.

2.2.3 Boundary conditions

Boundary conditions between the embedded fluids reflect the discontinuities of physical properties between the fluids while also enforcing continuity of the velocity and momentum throughout the aggregate. Already the no-slip boundary condition has been applied to the derivation of the BIEs in Section 2.2.2. No-slip boundary conditions are used when stress generated by the physical discontinuities between the two domains drives fluid velocities.

Conservation of momentum requires that the stress be balanced across the interface of the fluids. Each term in (2.4) may contain a discontinuity at the fluid interface due to discrete jumps in physical properties. The interfacial surface force term becomes

$$\Delta f_i = f_i^{(s)} - f_i^{(p)} = \left[\sigma_{ij}^{(s)} + \rho_s g_k x_k \delta_{ij} - \sigma_{ij}^{(p)} - \rho_p g_k x_k \delta_{ij}\right] \hat{n}_j. \tag{2.26}$$

Regrouping the stress and density terms, the interfacial stress jump may be written as

$$\Delta f_i = \Delta\rho g_k x_k \delta_{ij} \hat{n}_j + \Delta\sigma_{ij} \hat{n}_j, \tag{2.27}$$

where $\Delta\rho = \rho_s - \rho_p$ and $\Delta\sigma_{ij} = \sigma_{ij}^{(s)} - \sigma_{ij}^{(p)}$. The first term represents buoyancy forces due to the density contrast between the fluids, with the second term representing

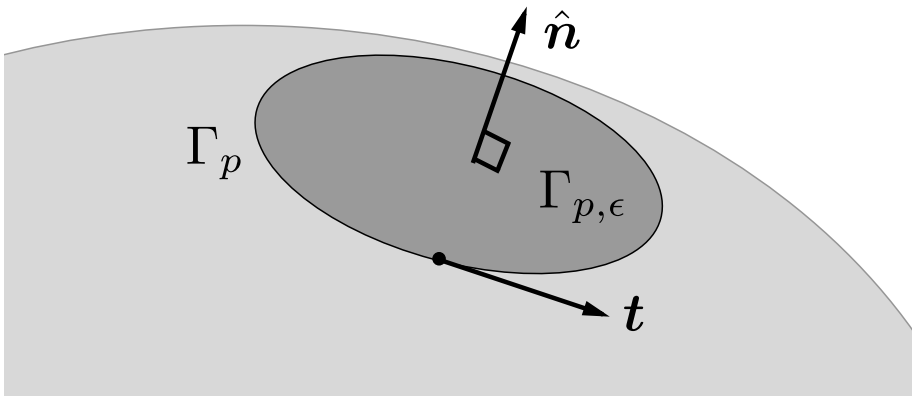

Figure 2.2: The portion of the boundary $\Gamma_{p,\epsilon}$ of the larger boundary Γ_p, which separates the p-th fluid from the suspension. The unit normal vector to the boundary is represented by $\hat{\boldsymbol{n}}$, and the vector $\boldsymbol{t}$ is the unit vector tangent to the boundary of $\Gamma_{p,\epsilon}$ on the fluid interface.

stresses driven by the physical properties of the interface.

Resolving the fluid stress jump, $\Delta\sigma_{ij}$, depends on the physical properties of the interface. Derivation of this term for common types of interfaces is covered in *Pozrikidis* [2001]. Here we examine the interfacial surface stresses originating from isotropic surface tension along a clean interface. The force balance between the surface tension γ and the normal fluid stress jump $\Delta\sigma_{ij}\hat{n}_j$ on a small element of the interface is given by

$$\begin{aligned}\int_{\Gamma_{p,\epsilon}} \Delta\boldsymbol{\sigma}\hat{\boldsymbol{n}}\,\mathrm{d}\Gamma_{p,\epsilon} &= \int_{\partial\Gamma_{p,\epsilon}} \gamma\hat{\boldsymbol{n}}\times\hat{\boldsymbol{t}}\,\mathrm{d}\partial\Gamma_{p,\epsilon} \\ &= \int_{\Gamma_{p,\epsilon}} \left[\hat{\boldsymbol{n}}\nabla\cdot(\gamma\hat{\boldsymbol{n}}) - \nabla(\gamma\hat{\boldsymbol{n}})\cdot\hat{\boldsymbol{n}}\right]\mathrm{d}\Gamma_{p,\epsilon}, \end{aligned} \tag{2.28}$$

where $\Gamma_{p,\epsilon}$ is a small continuous portion of the interface Γ_p, $\partial\Gamma_{p,\epsilon}$ is the boundary of the interface, and $\hat{\boldsymbol{t}}$ is the unit tangent vector to the interface as shown in Figure 2.2. Using a few identities, we can rewrite equation (2.28) in the indicial notation

as

$$\Delta\sigma_{ij}\hat{n}_j = \gamma\kappa\hat{n}_i - (\delta_{ij} - \hat{n}_i\hat{n}_j)\,\gamma_{,j}, \tag{2.29}$$

where the principal curvature is given by $\kappa = \hat{n}_{i,i}$.

The stresses induced by the two terms in (2.29) are referred to as the Laplace and Marangoni terms, respectively. The Laplace term arises from curvature driven surface tension force and describes the forces normal to the interface due to surface tension. The second term, often called the Marangoni term, arises from surface tension variations along the interface. The Marangoni term represents forces tangential to the interface, as indicated by the tangential projection operator, $(\delta_{ij} - \hat{n}_i\hat{n}_j)$. Variations in the tension on the grain surface can arise from either crystal anisotropy or midrange forces generated by interactions with neighboring grains [*Kang*, 2005].

Combining (2.27) and (2.29), we can express the stress jump across the interface as a function of buoyancy forces and isotropic surface tension,

$$\Delta f_i = \Delta\rho g_j x_j \hat{n}_i + \gamma\kappa\hat{n}_i - (\delta_{ij} - \hat{n}_i\hat{n}_j)\,\gamma_{,j}. \tag{2.30}$$

We use variations of (2.30) for the numerical experiments in Chapters 3, 4, and 5 where we assume fluid interfaces are clean.

2.2.4 Nondimensionalization

The BIEs in equations (2.23), (2.24), and (2.25) may be used to describe fluids that cover a wide range of physical characteristics. For instance, the length scale of features of interest may be on the scale of micrometers or tens of kilometers. Similarly, the time scales of the fluids may range from meters per second to centimeters per year. Handling the extreme range of physical properties is a computational challenge. The nondimensionalization process creates dimensionless BIEs, which have length and time scales appropriate for computation while capturing the influence of the physical parameters through a collection of dimensionless parameters.

This section describes three nondimensionalization processes of (2.25) based on the interfacial stress jump described in Section 2.2.3. The three dimensionless equations will represent the cases when the interfacial stress jump is driven by buoyancy and surface tension, buoyancy, and surface tension. Derivation of dimensionless forms of the BIE for a point in the infinite suspension and in the domain of a bounded fluid are straightforward from the dimensionless form of (2.25).

Nondimensionalization performs a change of variables in the BIE. The new variables are "dimensionless," lacking any physical units originally present. We first define the change of variables for the position and velocity variables. The relationships between the dimensional and dimensionless values are given by

$$x_i = x_c x_i' \tag{2.31}$$

$$u_i = u_c u_i', \tag{2.32}$$

where the non-prime variables are dimensional and the prime variables are dimensionless. The scalars x_c and u_c are the characteristic length and velocity scales, respectively. Characteristic scales represent the typical order of magnitude of values in the dimensional problem.

The dimensionless stress jump condition (2.30) can be expressed as

$$\Delta f_i' = \mathcal{B}_p \hat{g}_j x_j' \hat{n}_i + \gamma' \kappa' \hat{n}_i - (\delta_{ij} - \hat{n}_i \hat{n}_j)\, \gamma_{,j}'. \tag{2.33}$$

The dimensionless coefficient in front of the buoyancy term is referred to as the Bond number, which represents the ratio between the buoyancy forces and surface tension, given by

$$\mathcal{B}_p = \frac{\Delta \rho_p g x_c^2}{\gamma_c}. \tag{2.34}$$

As implied by the p subscripts, the Bond number may differ at each fluid interface. Specifically, a change in a Bond number represents a difference in the density contrast between two fluids.

Setting the characteristic velocity to $u_c = \frac{\gamma_c}{\mu_s}$, we arrive at the dimensionless BIE when both buoyancy and surface tension forces are present:

$$\begin{aligned} u_j(\boldsymbol{x}_0) =& \frac{2}{1+\lambda_q} \left[u_j^{\infty}(\boldsymbol{x}_0) - \frac{1}{4\pi} \sum_{p=1}^{P} \int_{\Gamma_p} \Delta f_i(\boldsymbol{x}) \mathcal{U}_{ij}(\boldsymbol{x}, \boldsymbol{x}_0)\, \mathrm{d}\Gamma_p' \right. \\ & \left. + \sum_{p=1}^{P} \frac{1-\lambda_p}{4\pi} \int_{\Gamma_p}^{\mathcal{PV}} u_i(\boldsymbol{x}) \mathcal{T}_{ijk}(\boldsymbol{x}, \boldsymbol{x}_0) \hat{n}_k(\boldsymbol{x})\, \mathrm{d}\Gamma_p \right] \qquad \boldsymbol{x}_0 \in \Gamma_q. \end{aligned} \tag{2.35}$$

If buoyancy forces are significantly larger than surface tension forces, the surface tension is approximated by $\gamma \approx 0$, changing the interfacial force term. The surface force is rewritten as

$$\Delta f_i = \Delta\rho g x_c \left[\hat{g}_j x'_j \hat{n}_i\right], \tag{2.36}$$

where the dimensionless values in the square brackets compose the dimensionless interfacial stress, $\Delta f'_i$. The BIE is rewritten as

$$\begin{aligned} u_j(\boldsymbol{x}_0) =& \frac{2}{1+\lambda_q}\left[u_j^{\infty}(\boldsymbol{x}_0) - \sum_{p=1}^{P}\frac{\mathcal{R}_p}{4\pi}\int_{\Gamma_p}\Delta f_i(\boldsymbol{x})\mathcal{U}_{ij}(\boldsymbol{x},\boldsymbol{x}_0)\,\mathrm{d}\Gamma_p\right. \\ &\left. + \sum_{p=1}^{P}\frac{1-\lambda_p}{4\pi}\int_{\Gamma_p}^{\mathcal{PV}} u_i(\boldsymbol{x})\mathcal{T}_{ijk}(\boldsymbol{x},\boldsymbol{x}_0)\hat{n}_k(\boldsymbol{x})\,\mathrm{d}\Gamma_p\right] \qquad \boldsymbol{x}_0 \in \Gamma_q. \end{aligned} \tag{2.37}$$

The dimensionless coefficient to the single-layer potential integral is commonly referred to as the compositional Rayleigh number, which represents the ratio of buoyancy terms to the viscous flow and is given by

$$\mathcal{R}_p = \frac{\Delta\rho_p g x_c^2}{u_c \mu_s}. \tag{2.38}$$

As implied by the p subscripts, the compositional Rayleigh number may differ at each fluid interface. Specifically, a change in the compositional Rayleigh number represents a difference in the density contrast between two fluids.

Finally, when buoyancy is negligible compared to surface tension, implying

$\mathcal{B}_p \ll 1$, we obtain a different form of the BIE,

$$u_j(\boldsymbol{x}_0) = \frac{2}{1+\lambda_q}\left[u_j^{\infty}(\boldsymbol{x}_0) - \frac{1}{4\pi \mathcal{C}a}\sum_{p=1}^{P}\int_{\Gamma_p} \Delta f_i(\boldsymbol{x})\mathcal{U}_{ij}(\boldsymbol{x},\boldsymbol{x}_0)\,\mathrm{d}\Gamma_p \right.$$
$$\left. + \sum_{p=1}^{P}\frac{1-\lambda_p}{4\pi}\int_{\Gamma_p}^{\mathcal{PV}} u_i(\boldsymbol{x})\mathcal{T}_{ijk}(\boldsymbol{x},\boldsymbol{x}_0)\hat{n}_k(\boldsymbol{x})\,\mathrm{d}\Gamma_p\right], \qquad \boldsymbol{x}_0 \in \Gamma_q, \tag{2.39}$$

where the dimensionless capillary number,

$$\mathcal{C}a = \frac{\mu_s u_c}{\gamma_c}, \tag{2.40}$$

represents the ratio between the viscous forces and surface tension.

Equations (2.35), (2.37), and (2.39) are dimensionless versions of the dimensional BIE from (2.25). In practice, the BIE for the pole point located on the boundary is the most important. These equations are used to obtain numerical solutions on the fluid interfaces. Then, if desired, the other BIEs are used to compute the velocities in the domain through a post-processing step. The dimensionless versions of the other BIEs are developed in the same straightforward manner and have been omitted for brevity.

2.3 Discretization

Solving the BIEs presented in Section 2.2 requires discretizing the geometry and integral equations to form an algebraic linear system of equations. Section 2.3.1 discusses the details of the discretization, interpolation, and adaptive refinement methods of fluid interface in two dimensions. Section 2.3.2 covers the discretization

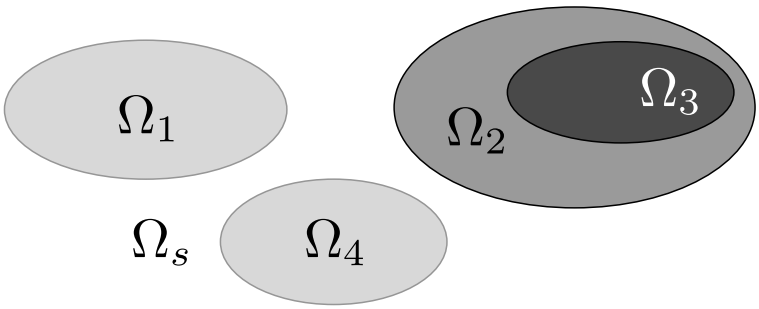

Figure 2.3: Possible arrangements for a geometry containing multiple fluids with various properties contained within an infinite suspending fluid, Ω_s. The different domains may have the same physical properties (denoted by color) as Ω_1 and Ω_4, or different properties as with Ω_2 and Ω_3. A bounded fluid may be completely contained within another bounded fluid as is the case with Ω_3 and Ω_2.

of the BIEs and produces a linear system of equations used to solve for the unknown velocities, as well as the numerical implementation of the kinematic condition for creeping flow.

2.3.1 Geometry

The discretization scheme for the geometry must be able to represent sufficiently-complicated geometries that capture the behavior of fluids encountered in physical models. In addition, an interpolation scheme for the discretized geometry is required for the integration of the BIEs. The discretization must also be adaptable, allowing for high-resolution features of the fluid interfaces to form while minimizing computational costs for representing low resolution geometry. Figure 2.3 is an example geometry that may be used in conjunction with the Stokes flow BIEs for multiple fluids presented in Section 2.2. Each closed curve contains a homogeneous fluid with properties distinct from adjacent fluids. Figure 2.4 shows the discretiza-

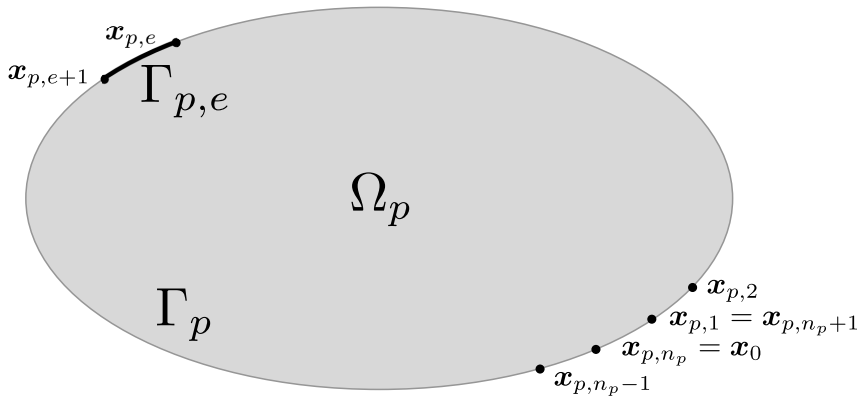

Figure 2.4: Discretization of the p-th fluid interface, Γ_p. The nodes are ordered counterclockwise with cyclic indexing used for convenience. The e-th boundary element of the fluid is denoted $\Gamma_{p,e}$ and is the segment between $\boldsymbol{x}_{p,e}$ and $\boldsymbol{x}_{p,e+1}$.

tion of a closed curve Γ_p into n_p boundary nodes. The nodes, labeled $\boldsymbol{x}_{p,1}, \ldots, \boldsymbol{x}_{p,n_p}$ and oriented in the counterclockwise direction, are indexed in cyclical fashion, e.g., $\boldsymbol{x}_{p,0} = \boldsymbol{x}_{p,n_p}$ and $\boldsymbol{x}_{p,n_p+1} = \boldsymbol{x}_{p,1}$. The segment between consecutive nodes $\boldsymbol{x}_{p,e}$ and $\boldsymbol{x}_{p,e+1}$ is the boundary element denoted by $\Gamma_{p,e}$. We interpolate the position within each boundary element using cubic spline interpolation, thus ensuring the interface is a Lyapunov surface with a continuous normal vector along the entire boundary.

The distance between the nodes, δ, dictates the resolution of the geometry. There is an inherent link between the curvature of the geometry and the δ required to sufficiently represent the features. We follow the work of *Dritschel* [1989], which developed an optimal empirical relationship between the curvature and node density. It was found that $\delta \propto \kappa^{\frac{2}{3}}$ provided the best representation of high resolution geometry while minimizing computational cost.

In addition to the relationship between node spacing and curvature, we place bounds on the maximum and minimum boundary element length and bounds on

the maximum-allowed curvature in the interface. Specifically, the high curvature features correspond to high-resolution features in the interface. If the curvature at a node rises beyond the predetermined threshold, surgery is performed to reduce the curvature. The modification creates error in the model; however, that error is deemed acceptable as any numerical model is only capable of finite resolution.

2.3.2 Linear system

The BIE (2.25) is a Fredholm equation of the second type, which can be discretized and solved using the method of collocation. In the method of collocation, the field point is placed on a boundary node. Then, the pole point is placed over the boundary nodes. Each of the integrals on each particle is thus expressed as a sum of integrals carried out on the boundary elements. The majority of boundary element integrals are regular and integrated using the standard eight-point Gaussian quadrature.

However, the integrals become singular when the pole point $\boldsymbol{x}_{q,f}$ is located on the boundary element. Due to the choice of geometry discretization, singular integration occurs when integrating over $\Gamma_{q,f-1}$ and $\Gamma_{q,f}$. For each pole point there are four boundary element integrals that must be handled with care. The single-layer potential integrals are weakly singular with the integral being finite despite the integrand diverging. The double-layer potential integrals are strongly singular with the integral being finite only in the sense of Cauchy principal value. Both types of singularities must be handled with care when integrating numerically.

We employ the radial integration method in two dimensions (RIM) introduced by *Gao* [2006] to numerically approximate the weakly and strongly singular integrals. The RIM separates the singular integral into finite and infinite parts by performing a change of variables and approximating the integrand as a power series. The new integral is written completely in terms of the radial distance from the singularity, which allows for the separation into singular and non-singular components. For weakly singular integrals, the singular integral goes to zero. The singular integral for strongly singular integrals is exactly the portion of the integral that becomes zero in the sense of Cauchy principal value.

There are $N = \sum_{p=1}^{P} n_p$ summations over boundary elements for each pole point $\boldsymbol{x}_{q,f}$ as well as N entries in the vectors representing the interfacial stress jump and velocity at the interface. Taken together, the boundary integrals may be represented as square matrix multiplications

$$\mathbf{U}\boldsymbol{\Delta f} \qquad \text{and} \qquad \mathbf{T}\boldsymbol{u}, \tag{2.41}$$

representing the single- and double-layer potential integrals, respectively. Each entry in $\mathbf{U}$ or $\mathbf{T}$ represents an evaluation of a boundary element integral. The matrices encompass information about the specific kernel function as well as the interpolation scheme for the variables along the boundary. The vectors $\boldsymbol{u}$ and $\boldsymbol{\Delta f}$ represent the unknown velocity and interfacial stress jump at pole points along the boundary, respectively.

Plugging in the representations from (2.41) into the BIE (2.25) yields an alge-

braic system of linear equations approximating the BIE for Stokes flow with multiple fluids,

$$\boldsymbol{u} = \boldsymbol{\lambda}\left[\boldsymbol{u}^{\infty} - \frac{1}{4\pi\mu_s}\mathbf{U}\boldsymbol{\Delta f} + \frac{1}{4\pi}\mathbf{T}\boldsymbol{u}\right], \tag{2.42}$$

where $\boldsymbol{\lambda}$ is a diagonal matrix given by

$$\boldsymbol{\lambda}_{ii} = \frac{2}{1+\lambda_q}, \tag{2.43}$$

where the i-th pole point is located on the interface of the q-th fluid. Rearranging the matrix equation isolates the unknown velocities $\boldsymbol{u}$:

$$\left(\boldsymbol{\lambda}^{-1} - \frac{1}{4\pi}\mathbf{T}\right)\boldsymbol{u} = \boldsymbol{u}^{\infty} - \frac{1}{4\pi\mu_s}\mathbf{U}\boldsymbol{\Delta f}. \tag{2.44}$$

The linear system (2.44) provides a numerical method for obtaining the unknown velocity or stress of the fluid along the boundary. The matrices $\mathbf{U}$ and $\mathbf{T}$ are known, involving the Stokeslet, Stresslet, interpolation scheme, and geometry. The viscosity matrix $\boldsymbol{\lambda}$ and viscosity of the suspension are known from the physical parameters of the problem. Likewise, the imposed velocity $\boldsymbol{u}^{\infty}$ is prescribed. Depending on boundary conditions, either the interfacial stress jump or velocity is prescribed at each pole point, leaving the other unknown.

After the velocity is obtained from (2.44), the geometry evolves through the kinematic condition (2.5). For the discretization scheme, pole points on the fluid

interfaces evolve in a forward Lagrangian manner with

$$\boldsymbol{x}_{p,e}^{(t+\Delta t)} = \boldsymbol{x}_{p,e}^{(t)} + \Delta t \boldsymbol{u}_{p,e}^{(t)}, \tag{2.45}$$

where Δt is the time step size, $\boldsymbol{x}_{p,e}^{(t)}$ is the position of the pole point at time t, $\boldsymbol{x}_{p,e}^{(t+\Delta t)}$ is the pole point at the next time step, and $\boldsymbol{u}_{p,e}^{(t)}$ is the velocity at the pole point at time t. After the geometry evolves, it is rediscretized based on the new geometry as outlined in Section 2.3.1.

We use an adaptive fourth order Runge-Kutta (RK4) method to update grain shapes from equation (2.5) using the velocities obtained from the BIE. In this adaptive scheme, the location of boundary nodes were updated using both one RK4 iteration of step size Δt and two RK4 iterations, each of step size $\Delta t/2$. If the L_1 norm of the difference between the pole positions for every node is less than a prescribed tolerance, then we use the result as the more refined evolution of the next time step. Otherwise, the process is repeated with $\Delta t/2$. When the time stepping scheme is successful, the next evolution attempts a time step of size $2\Delta t$, as long as the new larger time step is not larger than the maximum-allowed time step.

2.4 Fast Multipole Method

The system of linear algebraic equations arising from discretization of (2.25) is dense and generally asymmetric, requiring direct matrix inversion to solve. Direct methods require $\mathcal{O}(N^3)$ time and $\mathcal{O}(N^2)$ storage, where N is the number of pole points. The FMM uses series expansions to approximate the dense matrix-vector

multiplications [*Appel*, 1985; *Barnes and Hut*, 1986; *Ambrosiano et al.*, 1988; *Carrier et al.*, 1988; *Greengard and Gropp*, 1990; *Board and Schulten*, 2000]. The series expansions separate the pole points from the integrals over the field points, removing the requirement of a unique evaluation for every combination of pole point and boundary element. The end result is an approximate matrix-vector multiplication that takes $\mathcal{O}(N)$ time and space. The accelerated multiplication, in conjunction with iterative methods such as the general minimal residual method [*Saad*, 2003], solves the linear system (2.44) in $\mathcal{O}(N)$ time.

The boundary element integrals in the discretized BIE are written generally as

$$I(\boldsymbol{x}_0) = \sum_{e \in E} \int_{\Gamma_e} f(\boldsymbol{x}, \boldsymbol{x}_0) \, \mathrm{d}\Gamma_e, \tag{2.46}$$

where E is the collection of N boundary elements and $f(\boldsymbol{x}, \boldsymbol{x}_0)$ is a generic function dependent on both the pole and field point. The sum divides into

$$I(\boldsymbol{x}_0) = \underbrace{\sum_{e \in E_{near}} \int_{\Gamma_e} f(\boldsymbol{x}, \boldsymbol{x}_0) \, \mathrm{d}\Gamma_e}_{\text{Near-field}} + \underbrace{\sum_{e \in E_{far}} \int_{\Gamma_e} f(\boldsymbol{x}, \boldsymbol{x}_0) \, \mathrm{d}\Gamma_e}_{\text{Far-field}}, \tag{2.47}$$

where the first sum represents integrals over boundary elements near the pole point, while the second sum represents integrals over boundary elements far from the pole point, with $|E_{near}| \ll |E_{far}|$.

The FMM exploits the well-behaved kernels by representing a boundary element integral located away from the pole point with a series expansion approxi-

mation about some point, $\boldsymbol{x}_c$. Using a series approximation for distant boundary element integrals, equation (2.47) is approximated by

$$I(\boldsymbol{x}_0) \approx \underbrace{\sum_{e \in E_{near}} \int_{\Gamma_e} f(\boldsymbol{x}_0, \boldsymbol{x}) \, \mathrm{d}\Gamma_e}_{\text{Near-field}} + \underbrace{\sum_{k=0}^{p} g_k(\boldsymbol{x}_0, \boldsymbol{x}_c) c_k(\boldsymbol{x}_c)}_{\text{Far-field}}, \tag{2.48}$$

where the second summation on the right hand side has been replaced by a truncated series expansion that approximates the value of the integrals over distant boundary elements. The functions g_k are basis functions of the series expansions, which depend only on the pole point and the expansion center. The series coefficients c_k contain information about the distant boundary element integrals and do not depend on the pole points. With the series evaluation taking $\mathcal{O}(1)$ time, and $|E_{near}| \in \mathcal{O}(1)$, it only takes $\mathcal{O}(1)$ time to compute (2.48) versus $\mathcal{O}(N)$ for (2.47).

The following sections describe the mechanics for creating, translating, and evaluating the series expansion coefficients required for the FMM. Two types of series expansions are required to produce a final equation like (2.48). One section is dedicated for each type of expansion. The last section covers the details for domain partitioning, the required bookkeeping that maximizes the efficiency of the FMM.

2.4.1 Far-field expansions

The single-layer potential integrals from (2.25) may be rewritten as a complex integral using the canonical mapping from two dimensions to the complex plane,

$$I_{p,e}(z_0) = \int_{\Gamma_{p,e}} \Delta f_i(z) \mathcal{U}_{i1}(z, z_0)\, \mathrm{d}\Gamma_{p,e} + i \int_{\Gamma_{p,e}} \Delta f_i(z) \mathcal{U}_{i2}(z, z_0)\, \mathrm{d}\Gamma_{p,e}, \tag{2.49}$$

where $i = \sqrt{-1}$, $z = x_1 + i x_2$, z_0 is the complex representation of a pole point, and z is a complex point on the e-th boundary element of the p-th interface. The complex boundary element integral is expressed using the complex series expansion

$$\begin{aligned} I_{p,e}(z_0) = & \frac{1}{2} \left[\sum_{k=0}^{\infty} O_k(z_0 - z_c) M_k(z_c) \right. \\ & + z_0 \sum_{k=0}^{\infty} \overline{O_{k+1}(z_0 - z_c) M_k(z_c)} \\ & \left. + \sum_{k=0}^{\infty} \overline{O_k(z_0 - z_c)} N_k(z_c) \right], \end{aligned} \tag{2.50}$$

where $\overline{()}$ denotes the complex conjugate, the auxiliary functions are

$$I_k(z) = \frac{z^k}{k!} \quad k \geq 0 \quad \text{and} \quad O_k(z) = \begin{cases} -\log(z) & k = 0 \\ \frac{(k-1)!}{z^k} & k > 0 \end{cases}, \tag{2.51}$$

and the far-field series coefficients are

$$M_k(z_c) = \int_{\Gamma_{p,e}} I_k(z - z_c)\Delta f(z)\,\mathrm{d}\Gamma_{p,e} \qquad k \geq 0, \tag{2.52}$$

$$N_k(z_c) = \begin{cases} \int_{\Gamma_{p,e}} \Delta f(z)\,\mathrm{d}\Gamma_{p,e} & k = 0 \\ \int_{\Gamma_{p,e}} \left[\overline{I_k(z - z_c)}\Delta f(z) - z\overline{I_{k-1}(z - z_c)\Delta f(z)}\right]\,\mathrm{d}\Gamma_{p,e} & k \geq 1 \end{cases}, \tag{2.53}$$

where $\Delta f = \Delta f_1 + i\Delta f_2$ is the complex interfacial stress jump. Series expansion (2.50) is only valid when $|z - z_c| \ll |z_0 - z_c|$, which is to say the pole point must be located *far* away from the expansion center in relation to the field points on the boundary element.

Far-field expansion series may be translated from expansion center z_c to a new expansion center at z_c' using a matrix-vector multiplication defined by

$$M_k(z_c') = \sum_{l=0}^{k} I_k(z_c - z_c')M_l(z_c) \tag{2.54}$$

$$N_k(z_c') = \sum_{l=0}^{k} \overline{I_k(z_c - z_c')}N_l(z_c). \tag{2.55}$$

The new coefficients are valid under the additional constraint $|z - z_c'| \ll |z_0 - z_c'|$. Translating and adding far-field expansion series coefficients allows us to combine the coefficients from different far-field expansions series representing many distinct boundary element integrals.

Next, the double-layer potential integral is first written in complex form using

the canonical mapping from two dimensions to the complex plane,

$$J_{p,e}(z_0) = \int_{\Gamma_{p,e}} u_i(z)\mathcal{T}_{i1k}(z, z_0)\hat{n}_k(z)\,\mathrm{d}\Gamma_{p,e} + i\int_{\Gamma_{p,e}} u_i(z)\mathcal{T}_{i2k}(z, z_0)\hat{n}_k(z)\,\mathrm{d}\Gamma_{p,e}. \quad (2.56)$$

Then the complex integral is approximated using the far-field series expansion

$$\begin{aligned} J_{p,e}(z_0) = &\sum_{k=1}^{\infty} O_k(z_0 - z_c)\widetilde{M}_k(z_c) \\ &+ z_0 \sum_{k=1}^{\infty} \overline{O_{k+1}(z_0 - z_c)\widetilde{M}_k(z_c)} \\ &+ \sum_{k=1}^{\infty} \overline{O_k(z_0 - z_c)}\widetilde{N}_k(z_c). \end{aligned} \quad (2.57)$$

The coefficients for a Stresslet boundary element integral are given by

$$\widetilde{M}_k(z_c) = \int_{\Gamma_{p,e}} I_{k-1}(z - z_c)\hat{n}(z)u(z)\,\mathrm{d}\Gamma_{p,e} \qquad k \geq 1, \quad (2.58)$$

$$\widetilde{N}_k(z_c) = \begin{cases} \int_{\Gamma_{p,e}} \left[\hat{n}(z)\overline{u(z)} + \overline{\hat{n}(z)}u(z)\right]\,\mathrm{d}\Gamma_{p,e} & k = 1 \\ \int_{\Gamma_{p,e}} \left\{\overline{I_{k-1}(z - z_c)}\left[\hat{n}(z)\overline{u(z)} + \overline{\hat{n}(z)}u(z)\right]\right. & k \geq 2 \\ \qquad \left. -z\overline{I_{k-2}(z - z_c)\hat{n}(z)u(z)}\right\}\,\mathrm{d}\Gamma_{p,e} & \end{cases}, \quad (2.59)$$

where $u = u_1 + iu_2$ is the complex velocity and $\hat{n} = \hat{n}_1 + i\hat{n}_2$ is the complex unit normal vector along the boundary. Equations (2.54) and (2.55) translate the coefficients of the far-field series expansions for the Stresslet boundary element integrals as well, replacing the non-tilde coefficients with the tilde coefficients.

2.4.2 Near-field expansions

Near-field series expansions gather more boundary element integral information in series, while still ensuring the series is valid for a meaningful collection of pole points. Unlike the far-field series expansions, near-field series expansions are valid only near the expansion center. The near-field coefficients centered about z_L are constructed from far-field coefficients through

$$L_l(z_L) = (-1)^l \sum_{k=0}^{\infty} O_{l+k}(z_L - z_c) M_k(z_c) \tag{2.60}$$

$$K_l(z_L) = (-1)^l \sum_{k=0}^{\infty} \overline{O_{l+k}(z_L - z_c)} N_k(z_c) \tag{2.61}$$

for both the Stokeslet and Stresslet coefficients. Equations (2.60) and (2.61) are derived by relating the far- to near-field series expansions through the boundary element integrals for the potential equation [*Liu and Nishimura*, 2006].

As the name implies, near-field series are only valid when $|z_0 - z_L| \ll |z_c - z_L|$, which is to say the pole point must be much closer to the near-field expansion center than the far-field series expansion center. The near-field series are translated through

$$L_l(z'_L) = \sum_{m=l}^{\infty} I_{m-l}(z'_L - z_L) L_m(z_L) \tag{2.62}$$

$$K_l(z'_L) = \sum_{k=l}^{\infty} \overline{I_{m-l}(z'_L - z_L)} K_m(z_L) \tag{2.63}$$

under the additional constraint $|z_0 - z'_L| \ll |z_c - z'_L|$. The near-field expansion series

for the single- and double-layer boundary element integrals are evaluated by

$$\sum_{e \in E_{far}} I_e(z_0) = \frac{1}{2}\left[\sum_{l=0}^{\infty} L_l(z_L) I_l(z_0 - z_L) - z_0 \sum_{l=1}^{\infty} \overline{L_l(z_L) I_{l-1}(z_0 - z_L)} + \sum_{l=0}^{\infty} K_l(z_L) \overline{I_l(z_0 - z_L)}\right], \tag{2.64}$$

where E_{far} is the set of the boundary elements sufficiently far from z_0 represented by the near-field series coefficients.

2.4.3 Domain partitioning

The computational domain is partitioned using the Morton numbering scheme [*Morton*, 1966]. The scheme aids with the creation, translation, and combination of series coefficients, achieving the efficiency of the FMM without itself being computationally burdensome. The Morton numbering scheme partitions the domain into nested square cells based on an index generated from the cell's position in the physical domain. A typical cell has a parent, neighbors, and child cells, all of which can be computed in $\mathcal{O}(1)$ time given the Morton number of the cell. Cells with no children are commonly referred to as leaf cells.

By centering the far- and near-field series expansions in the cells, we can quickly determine their validity when translating and evaluating the series. This is critical to the linear speed and memory footprint of the FMM. Using an exact distance calculation between pole points and boundary elements would take $\mathcal{O}(N^2)$

time and space, which is an order slower than the optimal FMM multiplication scheme.

The Morton number of a point is based on its position. Given $\boldsymbol{x} \in [0,1)^2$, the point is represented in binary as $\boldsymbol{x} = (0.a_1a_2a_3a_4\ldots, 0.b_1b_2b_3b_4\ldots)_2$. The 8-bit Morton number for $\boldsymbol{x}$ is given by $(a_1b_1a_2b_2a_3b_3a_4b_4)_2$, where the significant digits of the point are interleaved. The Morton number scheme leads to a natural partitioning of the domain into cells organized in a quadtree.

The quadtree is used to track the validity of series expansions, using the L_1 scheme to replace the naïve $\mathcal{O}(N^2)$ internode distance test using L_2 distances. At any given level of the tree, a far-field series expansion in level l is valid in every cell except for the cell it is centered in and neighboring cells. A near-field series expansion in level l is valid only in the cell in which the expansion is centered.

Translating and combining far- and near-field series up and down the quadtree, near-field series representing $\mathcal{O}(N^2)$ boundary elements are calculated at each leaf cell in $\mathcal{O}(N)$ by

1. creating far-field series at the center of each leaf cell.

2. translating and merging near-field series up the quadtree.

3. translating far-field series to near-field series in non-neighboring cells.

4. translating and merging near-field series down the quadtree.

5. evaluating the near-field expansion in a leaf cell at all pole points in the cell.

6. directly evaluating the boundary element integrals in a pole point's leaf cell

and neighboring cells.

The result of the upward and downward pass is a near-field series in each leaf cell representing $\mathcal{O}(N)$ of the boundary element integrals. The series are evaluated in $\mathcal{O}(1)$, relying only on the pole point, expansion center, and near-field coefficients. There are $\mathcal{O}(1)$ integrals not represented by a near-series, which must be computed directly. In all, the FMM reduces the time to perform a matrix-vector multiplication from $\mathcal{O}(N^2)$ time and storage to $\mathcal{O}(N)$.

2.5 Validation and benchmarking

The FMBEM is implemented in the Fortran 2008 language using the Intel®Math Kernel Library (MKL) for linear algebra operations, including the GMRES solver, and the Intel®ComposerXE Fortran compiler. The algorithm is parallelized for shared memory machines using OpenMP directives. We validate our implementation against the Hadamard-Rybczyñski solution for a steady state viscous drop settling in an infinite fluid [*Kim and Karilla*, 2005; *Happel and Brenner*, 1983]. Asymptotic analysis of the program's runtime confirms the algorithm is implemented correctly, and properly scales with both problem size and computer hardware.

BIE (2.25) is a Fredholm equation of the second type when solving for the velocity at the fluid interfaces, allowing for straightforward discretization and solving. The resulting linear system has both positive and negative eigenvalues all with magnitude less than or equal to unity, thus the convergence of GMRES is governed by the condition number of the matrix, κ. The condition number depends on the

boundary discretization and the viscosity ratio with $\kappa \propto exp(|\log\lambda|)$. In our numerical experiments, $|\log\lambda| \leq 2$ resulting in well conditioned linear systems, which were experimentally confirmed. The convergence theorem for positive definite matrices guarantees accurate solutions when the relative error of the residual is less than 10^{-8}.

2.5.1 Hadamard-Rybczyñski analytical solution

The Hadamard-Rybczyñski analytical solution (HR) provides steady state analytical approximation of the velocities for a viscous sphere translating in an infinite fluid. The solution is built from Lamb's general solutions both inside and outside of an axis-symmetric sphere. The coefficients of the spherical harmonics are calculated based on the boundary conditions at the interface between the fluids. Similar to the boundary conditions used in the derivation of the BIE, HR prescribes no-slip velocities and conservation of momentum along the fluid interface. An additional kinematic condition is prescribed to ensure the velocities for the drop are indeed a steady state solution, i.e., the shape of the sphere does not change.

The spherical drop, denoted Ω_2, is embedded in an infinite suspending fluid Ω_1, as seen in Figure 2.5. The drop of radius a is represented in spherical coordinates, centered at $r = 0$. The geometry and solution are axis-symmetric about the azimuthal angle θ, leading to tangential variations in the velocity along the polar angle ϕ.

Using Lamb's general solutions, the velocity outside the spherical drop is de-

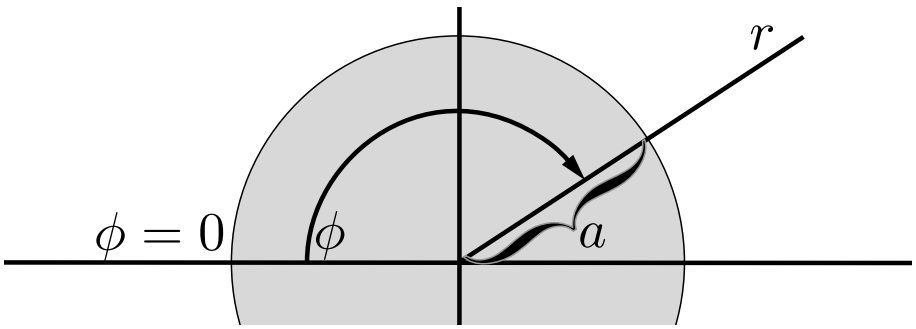

Figure 2.5: Geometry of the axis-symmetric translating sphere with radius $r = a$ in spherical coordinates. The fluids are symmetric about the $\phi = 0$ axis, hence the lack of the azimuthal angle in the geometry. The polar angle is measured from the left edge of the sphere. The exterior fluid is set to translate from right to left, over and under the sphere.

scribed by

$$u_r^{(1)}(r,\phi) = \left[A_1\left(\frac{a}{r}\right) - 2B_1\left(\frac{a}{r}\right)^3\right] u_c \cos\phi \tag{2.65}$$

$$u_\phi^{(1)}(r,\phi) = -\left[\frac{A_1}{2}\left(\frac{a}{r}\right) + B_1\left(\frac{a}{r}\right)^3\right] u_c \sin\phi, \tag{2.66}$$

where u_c is the HR velocity for the settling drop. A similar formulation is derived for the velocity inside of the drop:

$$u_r^{(2)}(\rho,\phi) = \left[\frac{a_1}{10}\left(\frac{r}{a}\right)^2 + b_1\right] u_c \cos\phi \tag{2.67}$$

$$u_\phi^{(2)}(r,\phi) = -\left[\frac{a_1}{5}\left(\frac{r}{a}\right)^2 + b_1\right] u_c \sin\phi. \tag{2.68}$$

Determining the coefficients of (2.65), (2.66), (2.67), and (2.68) requires four constraints. Specifically, at the boundary of the drop, $r = a$, we require

1. $u_r^{(1)} = u_c \cos\phi$ for no-slip and kinematic conditions.

2. $u_r^{(2)} = u_c \cos\phi$ for no-slip and kinematic conditions.

3. u_ϕ be continuous for the no-slip condition.

4. $\sigma_{\phi r}$ be continuous for conservation of momentum.

The resulting coefficients for Lamb's general solution for a translating viscous sphere are:

$$A_1 = \frac{2+3\lambda}{2(1+\lambda)} \qquad B_1 = \frac{\lambda}{4(1+\lambda)} \qquad a_1 = -\frac{5}{1+\lambda} \qquad b_1 = \frac{3+2\lambda}{2(1+\lambda)}. \tag{2.69}$$

We tested a range of viscosity ratios and density differences for the drop problem. For each test, $N = 100$ pole points were evenly distributed along the interface. Agreement was very high in the tangential direction, especially when $\lambda > 1$ as seen in Figure 2.6. The radial velocity never differed by more than 10%, as observed in other published and verified implementations of the BEM. The error between the HR and BEM solutions is attributed to the problem dimension. The numerical solution we derive is more akin to a translating infinite cylinder in three dimensions than a translating sphere.

We verify convergence by solving a numerical problem using N and $2N$ pole points and computing the difference between solutions. As N increases, the difference between the two numerical solutions decreases at the convergence rate. Figure 2.7 shows the convergence of our numerical algorithm and confirms the convergence rate $\mathcal{O}\left(N^{-2.5}\right)$ we expect for BEM with our interpolation scheme.

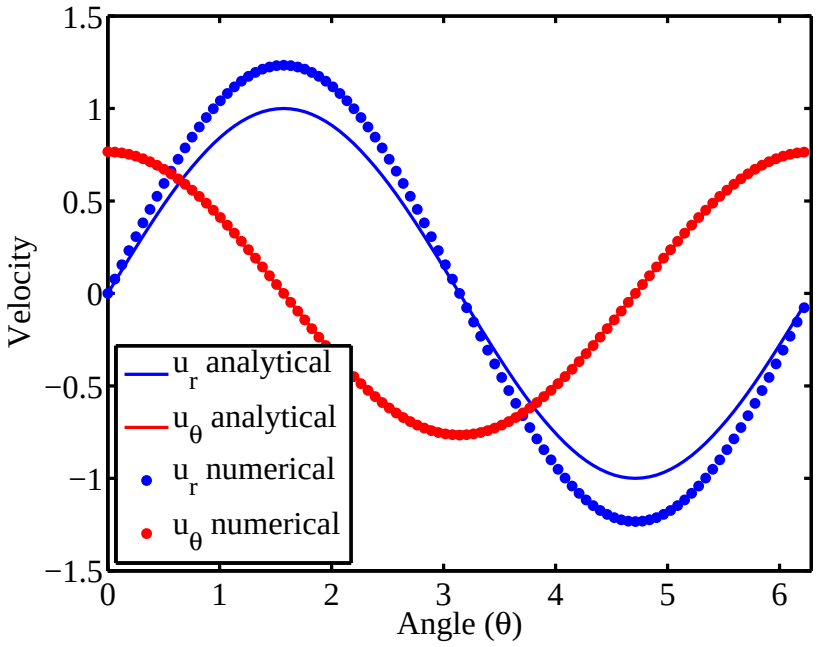

Figure 2.6: The blue and red dots represent the radial and tangential components of the velocity of a settling viscous drop obtained from solving BIE (2.37) with $\lambda = 1$, $\mathcal{R} = 3.75$, and $a = 1$ for 100 poles evenly distributed along the boundary. The blue and red lines represent the radial and tangential components of the analytical velocity given by the Hadamard-Rybczyñski solution. Both values are given with respect to the angle θ, which represents the counterclockwise angle from the point to the negative y axis.

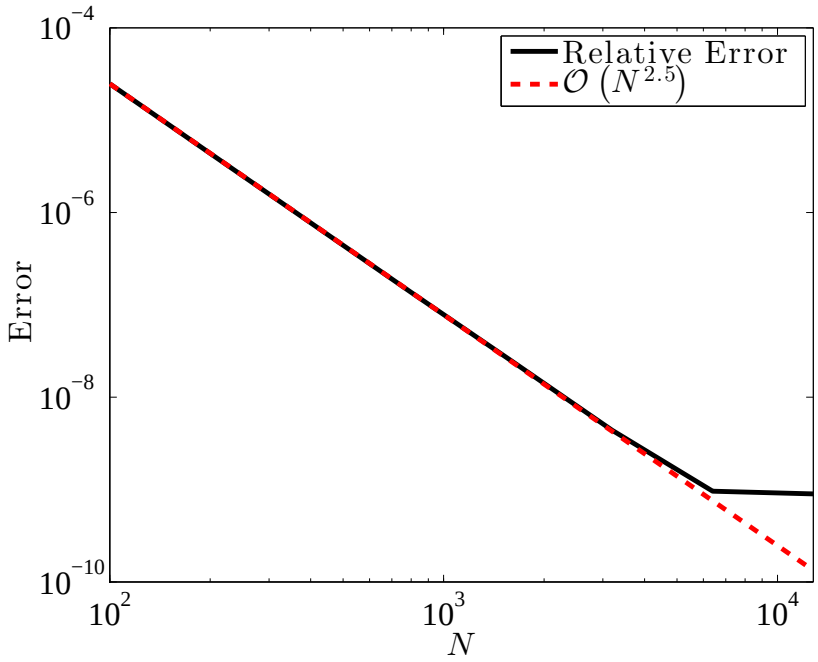

Figure 2.7: The black line represents the relative error between the numerical solution to the translating drop problem with N nodes and $2N$ nodes. The dashed red line is $\mathcal{O}\left(N^{-2.5}\right)$. There is excellent agreement until the error drops below 10^{-9}, which is to be expected as the iterative solver stops refining when the residual in the solution is less than 10^{-9}.

2.5.2 Asymptotic scaling

Asymptotic scaling analysis is performed for the FMBEM matrix-vector multiplications using the Stokeslet and Stresslet matrices. For testing, we used a workstation powered by two Intel®Xeon E5-2620 processors and 64 GB of memory. Each Xeon package has six physical cores mapped to twelve virtual cores through the Intel®Hyper-Threading architecture (HT). A physical core has 256 KB of private L2 cache and shares a 15 MB L3 cache with the five other processors on the package.

Scaling of the algorithm on 24 virtual cores for a varying number of pole nodes is displayed in Figure 2.8 in Log-Log format. Overall, there is good agreement between the time to perform a matrix-vector product and linear scaling. For smaller matrices, i.e., less than 10^6 degrees of freedom (DOF), the agreement is not as tight as it is for larger matrices where there is little deviation between the theoretical and experimental scaling analysis.

Efficiency of the algorithm using c cores is given by

$$E_c = \frac{T_1}{T_c c}, \tag{2.70}$$

where T_1 is the time to run on one core and T_c is the time to run on c cores. Ideally, the efficiency is 1, indicating each additional processor contributes fully to the problem.

We issue a thread for each virtual core, but use the physical core count when measuring efficiency as it reflects the amount of computational units on the proces-

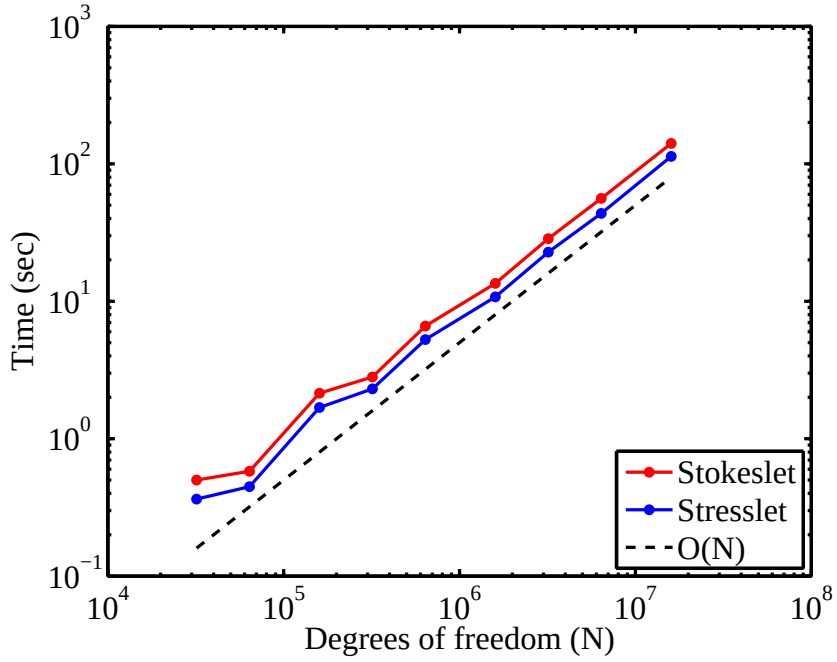

Figure 2.8: Asymptotic scaling of the FMM matrix-vector multiplication for the Stokeslet (red) and Stresslet (blue) matrices. Explicit timing measurements are marked with a dot, and the black dashed line represents linear scaling.

sor. Table 2.1 shows the efficiency of a matrix-vector multiplication for a problem with 3.2×10^6 DOFs for 12 physical cores. The efficiency for the physical cores is near the theoretical optimum with an efficiency of 96.0% for the Stokeslet computation and 84.5% for the Stresslet computation.

Multiplication	T_1	T_{max}	E_p
Stokeslet	316.5	27.5	96.0%
Stresslet	225.4	22.2	84.5%

Table 2.1: Parallel scaling analysis of the FMM matrix-vector multiplication for the Stokeslet and Stresslet matrices. The time for a single thread measured in seconds is in the T_1 column. We set the number of threads $T_{max} = 24$, the maximum number of threads that can simultaneously issue through HT. The efficiency E_p measures the efficiency for the number of physical cores for $c = 12$.

Chapter 3: Development of Anisotropic Contiguity in Deforming Partially Molten Aggregates I: Theory and Fast Multipole Boundary Element Method

3.1 Introduction

The geometry of melt distribution in partially molten rocks strongly influences their effective physical properties such as elastic moduli, viscosity, electrical conductivity, permeability, and mechanical absorption. In the microscopic scale, contiguity, the fractional area of intergranular contact, determines the strength of the load bearing network of grains in the aggregate. For a given volume fraction of melt and a given melt-grain dihedral angle, the contiguity of the aggregate depends on the state of deformation [*Takei and Holtzman*, 2009; *Takei*, 2005]. For example, in an undeformed aggregate, a small volume fraction of melt can be distributed in randomly oriented grain-edge tubules. Deformation of such an aggregate will redistribute the same volume fraction of melt into grain boundary films [*Hier-Majumder and Kohlstedt*, 2006; *Zimmerman et al.*, 1999; *Daines and Kohlstedt*, 1997] or melt-rich, disaggregated bands [*Holtzman et al.*, 2003; *Hustoft and Kohlstedt*, 2006; *King et al.*, 2011]. The orientation of these newly created melt films and bands will be

governed by the orientation of the principal stresses, transforming the contiguity from a scalar to an anisotropic tensorial quantity. Since the elastic strength of the network of grains is controlled by the contiguity of the aggregate, the development of anisotropic contiguity will be reflected in a change of the elastic properties of the aggregate.

Forces arising from plate tectonics can be agents of such textural transformation in the Earth's interior. One especially interesting region is the Lithosphere-Asthenosphere Boundary (LAB), characterized by a large reduction of the strength of the asthenosphere underlying the rigid lithosphere. Besides the reduction in strength, the LAB is marked by a sharp reduction [*Fischer et al.*, 2010; *Rychert et al.*, 2010; *Schmerr*, 2012] and a global anisotropy [*Nettles and Dziewoski*, 2008] in shear wave speed, anisotropic electrical conductivity [*Naif et al.*, 2013; *Evans et al.*, 2005], and a small volume fraction of melt [*Sifré et al.*, 2014]. The LAB is also a dynamic environment as the motion between rigid plates and the flow in the weak asthenosphere are coupled through this region. Deformation of the partially molten matrix of the LAB will segregate the melt, rendering the contiguity anisotropic. The coupling between deformation and anisotropic contiguity, therefore, provides an important set of constraints to explain the observed features of the LAB. To quantify this coupling, laboratory experiments and theoretical models of microstructures serve as powerful tools.

The role of deformation in melt redistribution has been studied extensively in laboratory experiments [*Daines and Kohlstedt*, 1997; *Holtzman et al.*, 2003; *Hustoft and Kohlstedt*, 2006; *Hier-Majumder and Kohlstedt*, 2006; *Zimmerman et al.*,

1999; *Takei*, 2005; *King et al.*, 2011]. In these two step experiments, the first step involved preparing undeformed, hot isostatically pressed aggregates. Next, these aggregates were deformed in pure shear, simple shear, or torsion configurations. After deformation, melt segregation was characterized by comparing microstructures of undeformed and deformed samples. While the melt geometry before and after deformation could be measured from these experiments, the experimental setup precluded the possibility of monitoring the evolution of contiguity during the course of deformation. In addition, *Takei* [2005] studied the development of shear wave anisotropy caused by the development of anisotropic contiguity during deformation experiments on analogue materials. While the results from these laboratory experiments indicate a likely relation between them, a direct quantification linking deformation, anisotropic contiguity, and anisotropic shear wave speed is still lacking.

Theoretical models of microstructure follow two different approaches. The first approach uses grain-melt geometry based on an assumed steady state grain shape [*von Bargen and Waff*, 1986; *Wray*, 1976; *German*, 1985; *Takei*, 1998]. The work of *Takei* [1998] introduced the use of contiguity in the constitutive relations of partially molten rocks. The contiguity in this work, however, was derived by varying the size of intergranular contact patches on the surface of a spherical grain. Since the description of contiguity is purely geometric, this group of formulations fails to account for the role of deformation in the evolution of contiguity. To address this issue, a second group of microgeodynamic models presented a formulation for modeling equilibrium geometry of partially molten aggregates driven by surface tension and small viscous deformation within the grains [*Hier-Majumder*, 2008,

2011; *Hier-Majumder and Abbott*, 2010; *Wimert and Hier-Majumder*, 2012]. Using the Boundary Element Method (BEM) and a semianalytical method, this group of articles quantified the contiguity of a unit cell in a partially molten aggregate for varying surface tensions in the steady state.

The BEM, while containing the equations necessary to describe the microstructure at large strains, suffered from a limitation. In the BEM, the governing PDEs of mass and momentum conservation are converted to a Boundary Integral Equation (BIE). When this BIE is discretized into a set of algebraic equations, the resulting system of algebraic equations is dense. As a result, calculations involving many grains become prohibitively expensive. This issue limited the capacity of these models in addressing the role of deformation in the development of anisotropic contiguity. It is crucial to incorporate a large number of grains in microstructural simulations of deformation such that melt segregation over length scales larger than a unit cell can be modeled. Thus, it is necessary to develop a numerical technique that can address the crucial issues of measuring anisotropic contiguity during deformation and yet remain computationally feasible.

This work bridges the gap by implementing the Fast Multiple Method (FMM) to numerically accelerate the BEM. We employ the resulting Fast Multipole Boundary Element Method (FMBEM) to study the development of anisotropic contiguity in deforming partially molten rocks. This model tracks the evolution of anisotropic contiguity and anisotropic shear wave speed as deformation progresses. To the best of our knowledge, this is the first study that directly quantifies the link between deformation, development of anisotropic contiguity, and anisotropic shear wave speeds.

This chapter outlines numerical methods and presents the simulated microstructures for pure and simple shear deformation. Chapter 4 presents the results for anisotropic contiguity and anisotropic shear wave velocity and the implications for the observed nature of the LAB [*Hier-Majumder and Drombosky*, 2014]. We introduce the various aspects of our mathematical model in Section 3.2. We present the governing Partial Differential Equations (PDEs) and the BIE in this section. The section also includes a mathematical description of the problem geometry and computation of differential shortening and the contiguity tensor. In Section 3.2.4, we develop the numerical methods involving FMM numerical acceleration technique. Section 3.3 presents the results of our numerical simulations. In Section 3.4, we discuss the trade-offs involved in our selection of parameter space and provide a qualitative comparison between our work and previous studies. Summary and conclusions of the microstructural model are provided in Section 3.5.

3.2 Model

The evolution of the melt geometry in a deforming, partially molten aggregate is determined by a coupled viscous flow within the grains and melt. In this section, we present the governing equations for the coupled flow, the setup for our numerical experiments, and the methods of post-processing our numerical data.

3.2.1 Governing equations

Consider a collection of viscous, contiguous grains with the interstitial space filled with a less viscous melt. The grains and melt are treated as incompressible fluids, such that the conservation of mass within each phase leads to

$$u^p_{i,i} = 0, \tag{3.1}$$

where the superscript p is different for each grain and the melt, u^p_i is the i-th component of the velocity vector, and $(,i)$ represents the derivative with respect to x_i. Conservation of momentum within each grain and the melt requires that, in the absence of a body force,

$$\sigma^p_{ij,i} = 0, \tag{3.2}$$

where the stress tensor σ^p_{ij} for a phase with viscosity μ_p and dynamic pressure P^p is given by

$$\sigma^p_{ij} = -\delta_{ij} P^p + \frac{\mu_p}{2}\left(u^p_{i,j} + u^p_{j,i}\right), \tag{3.3}$$

where δ_{ij} is the Kronecker delta. The governing PDEs (3.1) and (3.2) within each grain and the melt need to be supplemented with boundary conditions to solve for the unknown velocity and dynamic pressure.

First, we impose the no-slip boundary condition at the surface of each grain

[*Pozrikidis*, 2001; *Leal*, 1992; *Kim and Karilla*, 2005], such that

$$u_i^{(-)}\Big|_{\Gamma_p} = u_i^{(+)}\Big|_{\Gamma_p}, \tag{3.4}$$

where $u_i^{(-)}$ is the velocity just inside the grain surface, $u_i^{(+)}$ is the velocity outside the grain surface, and Γ_p is the surface of the p-th grain.

Next, we require that the difference in traction across the grain interface is balanced by surface tension forces, leading to the vector boundary condition on Γ_p, the surface of the p-th grain,

$$\Delta\sigma_{ij}^p \hat{n}_j + (\delta_{ij} - \hat{n}_i\hat{n}_j)\,\gamma_{,j} - \gamma\kappa\hat{n}_i = 0, \tag{3.5}$$

where $\Delta\sigma_{ij}^p$ is the stress drop across the surface of the p-th grain, $\gamma(\boldsymbol{x})$ is the interfacial tension, and $\hat{n}_i$ is the unit normal vector along Γ_p pointing into the melt [*Leal*, 1992]. The first term in (3.5) arises from the difference in the traction across the grain-melt interface. The second term, often described as the Marangoni condition, arises due to the variation of surface tension along the interface of the grain. The tensor operator, $(\delta_{ij} - \hat{n}_i\hat{n}_j)$, projects the vector gradient of surface tension on the interface of the grain. As a result, this component of the boundary condition is tangential to the boundary. The final term, often described as the Laplace condition, arises from curvature driven surface tension force, where the principal curvature of the interface is given by $\kappa = \hat{n}_{i,i}$ [*Leal*, 1992; *Pozrikidis*, 2001; *Kim and Karilla*, 2005; *Manga and Stone*, 1993]. This term is directed along the unit normal. In

the absence of deformation ($\Delta\sigma_{ij} = \Delta P\delta_{ij}$, from equation (3.3)) and constant surface tension ($\gamma_{,j} = 0$), equation (3.5) reduces to the Young-Laplace equation [*Kang*, 2005, eq. 2.19].

The Marangoni condition indicates that the variation of the interfacial tension along the grain surface leads to an imbalance of shear stress and drives viscous deformation within the grain. Variations in the tension on the grain surface arise from the fact that the atomic scale structure of grain-grain contacts is different from the grain-melt contacts. The dihedral angle at the grain-grain-melt triple junctions is controlled by the Marangoni term. In the absence of motion ($\Delta\sigma^p_{ij} = 0$) and zero curvature on flat contacts ($\kappa = 0$), equation (3.5) reduces to the commonly used dihedral angle equation or the Young Duprée equation [*Sutton and Balluffi*, 1995, eq 4.136]. In this work, we assume that the microstructure is equilibrated prior to deformation, and consider the surface tension to be constant along the grain. Laboratory experiments on a number of different grain-melt aggregates with varying dihedral angles reveal that melt segregation during deformation is independent of the dihedral angle [*Hier-Majumder and Kohlstedt*, 2006; *Hustoft and Kohlstedt*, 2006; *Zimmerman et al.*, 1999]. The assumption $\gamma_{,j} = 0$, therefore, simplifies our governing equations without introducing a substantial error in the results.

Finally, we need an additional equation to describe the change in grain shape due to deformation. Let $F^p(\boldsymbol{x}, t) = 0$ be the level set that defines Γ_p at time t. To ensure that the volume of each grain remains constant during deformation of the

grain, we use the kinematic equation

$$F^p_{,t}(\boldsymbol{x},t) + u_i(\boldsymbol{x},t)F^p_{,i}(\boldsymbol{x},t) = 0. \tag{3.6}$$

In the BEM, we eliminate the dynamic pressure, P^p, by combining the PDEs (3.1) and (3.2), subject to the boundary conditions for no-slip (3.4) and the continuity of traction (3.5) [*Hier-Majumder*, 2008]. This results in an integral equation for the unknown velocity. For an aggregate containing P grains embedded in a melt, the velocity $u_j(\boldsymbol{x}_0)$ at point $\boldsymbol{x}_0$ on the surface of the q-th grain is given by:

$$\begin{aligned} u_j(\boldsymbol{x}_0) =& \frac{2}{1+\lambda_q}\left[u^\infty_j(\boldsymbol{x}_0) - \frac{1}{4\pi\mu_m}\sum_{p=1}^{P}\int_{\Gamma_p}\Delta f_i(\boldsymbol{x})\mathcal{U}_{ij}(\boldsymbol{x},\boldsymbol{x}_0)\,\mathrm{d}\Gamma_p\right. \\ &\left. + \sum_{p=1}^{P}\frac{1-\lambda_p}{4\pi}\int_{\Gamma_p}^{\mathcal{PV}} u_i(\boldsymbol{x})\mathcal{T}_{ijk}(\boldsymbol{x},\boldsymbol{x}_0)\hat{n}_k(\boldsymbol{x})\,\mathrm{d}\Gamma_p\right] \qquad \boldsymbol{x}_0 \in \Gamma_q, \end{aligned} \tag{3.7}$$

where $\boldsymbol{x}_0$ is the pole point and the point $\boldsymbol{x}$ on the surface of the p-th grain is the field point [*Pozrikidis*, 2001]. The two integrals over the interface of the p-th grain, Γ_p, are referred to as the single-layer and double-layer potential integrals, respectively. The dimensionless parameter, $\lambda_p = \mu_p/\mu_m$, is the viscosity ratio between the p-th grain and melt. The velocity $u^\infty_j(\boldsymbol{x}_0)$ represents an applied far-field velocity. By prescribing different far-field velocities, we can simulate the effect of different environments of deformation of the matrix. This issue is discussed in further detail in the following section. The presence of the unknown u_i in the integrand of the double-layer integral renders equation (3.7) a Fredholm integral equation of the second kind.

Both integrands on the right hand side of equation (3.7) contain tensorial kernel functions. These tensors, $\mathcal{U}_{ij}(\boldsymbol{x}, \boldsymbol{x}_0)$ and $\mathcal{T}_{ijk}(\boldsymbol{x}, \boldsymbol{x}_0)$, arise from the velocity and stress components of the fundamental solution to the PDE governing Stokes flow [*Pozrikidis*, 2001; *Ladyzhenskaya*, 1963; *Kim and Karilla*, 2005]. For the present two-dimensional analysis, the second rank tensor $\mathcal{U}_{ij}(\boldsymbol{x}, \boldsymbol{x}_0)$, also referred to as the Stokeslet, is given by

$$\mathcal{U}_{ij}(\boldsymbol{x}, \boldsymbol{x}_0) = -\delta_{ij} \ln r + \frac{\hat{x}_i \hat{x}_j}{r^2}, \tag{3.8}$$

where $\hat{\boldsymbol{x}} = \boldsymbol{x} - \boldsymbol{x}_0$ and $r = |\hat{\boldsymbol{x}}|$. The third rank tensor $\mathcal{T}_{ijk}(\boldsymbol{x}, \boldsymbol{x}_0)$ is known as the Stresslet and is given by

$$\mathcal{T}_{ijk}(\boldsymbol{x}, \boldsymbol{x}_0) = -4\frac{\hat{x}_i \hat{x}_j \hat{x}_k}{r^4}. \tag{3.9}$$

When $\boldsymbol{x} \to \boldsymbol{x}_0$, both $\mathcal{U}_{ij}(\boldsymbol{x}, \boldsymbol{x}_0)$ and $\mathcal{T}_{ijk}(\boldsymbol{x}, \boldsymbol{x}_0)$ diverge. In the context of (3.7), the single-layer integral is weakly singular. That is, the integrand is singular, but the integral remains finite. The double-layer integral is strongly singular and is only finite in a Cauchy principal value sense [*Pozrikidis*, 2001; *Ladyzhenskaya*, 1963; *Kim and Karilla*, 2005].

The interfacial tension $\Delta f_i(\boldsymbol{x})$ in the single-layer integral arises from the boundary condition balancing the stress drop across the grain-melt interface with the Laplace and Marangoni conditions. Based on the discussion following equation

(3.5), we drop the Marangoni term such that the interfacial tension becomes

$$\Delta f_i(\boldsymbol{x}) = \gamma \hat{n}_{j,j} \hat{n}_i. \tag{3.10}$$

We nondimensionalize the governing equations by the grain radius x_c, velocities by a characteristic velocity scale u_c, and the surface tension by γ_c. We rewrite (3.7) in dimensionless form yielding

$$\begin{aligned} u_j(\boldsymbol{x}_0) =& \frac{2}{1+\lambda_q}\left[u_j^{\infty}(\boldsymbol{x}_0) - \frac{1}{4\pi \mathcal{C}a}\sum_{p=1}^{P}\int_{\Gamma_p} \Delta f_i(\boldsymbol{x}) \mathcal{U}_{ij}(\boldsymbol{x},\boldsymbol{x}_0)\,\mathrm{d}\Gamma_p \right. \\ &\left. + \sum_{p=1}^{P}\frac{1-\lambda_p}{4\pi}\int_{\Gamma_p}^{\mathcal{PV}} u_i(\boldsymbol{x}) \mathcal{T}_{ijk}(\boldsymbol{x},\boldsymbol{x}_0)\hat{n}_k(\boldsymbol{x})\,\mathrm{d}\Gamma_p\right] \qquad \boldsymbol{x}_0 \in \Gamma_q, \end{aligned} \tag{3.11}$$

where the dimensionless capillary number, $\mathcal{C}a$, represents the ratio between viscous forces on a grain and the forces arising from surface tension at the grain-melt interface. The capillary number can be expressed in terms of the melt viscosity μ_m, characteristic velocity u_c, and characteristic surface tension γ_c as

$$\mathcal{C}a = \frac{\mu_m u_c}{\gamma_c}. \tag{3.12}$$

The viscosity ratio and the capillary number are the two parameters that control the evolution of grain shapes for an imposed velocity $u_j^{\infty}(\boldsymbol{x}_0)$. At each time step, we solve the BIE (3.11) numerically to obtain the velocities at the boundary nodes of each grain. Next, we update the shape of each grain using equation (3.6). The geometric parameters from the new grain shape are then used to solve the BIE for

the next time step.

3.2.2 Setup for numerical experiments

To study the evolution of anisotropic contiguity by deformation, we carried out two sets of numerical experiments. In each set of experiments, the undeformed aggregate consists of a matrix packed with hexagonal grains surrounded by six neighbors. The simulated microstructure in Figure 3.1(a) outlines the geometry of a typical undeformed grain. Following *Hier-Majumder* [2008], the initial grain shape $F^p(0, \boldsymbol{x}) = 0$ is prescribed by the parametric representation

$$\boldsymbol{x} = \begin{bmatrix} \cos(\theta) \\ \\ \sin(\theta) \end{bmatrix} (1 - \epsilon \cos^2(3\theta)), \tag{3.13}$$

where θ is the counterclockwise angle from the positive x axis and the constant parameter $\epsilon = 0.05$ represents deviation of an individual grain shape from a unit circle [*Hier-Majumder*, 2008].

In the numerical experiments, we want to simulate the response of the partially molten system under an applied, constant strain rate, $\dot{\mathbf{E}}$. This is achieved by prescribing the far-field velocity $\boldsymbol{u}^\infty = \dot{\mathbf{E}} \cdot \boldsymbol{x}$. For pure and simple shear experiments, the strain rate tensors $\dot{\mathbf{E}}_{pure}$ and $\dot{\mathbf{E}}_{simple}$ are defined as

$$\dot{\mathbf{E}}_{pure} = \begin{bmatrix} 1 & 0 \\ \\ 0 & -1 \end{bmatrix} \quad \text{and} \quad \dot{\mathbf{E}}_{simple} = \begin{bmatrix} 0 & 1 \\ \\ 0 & 0 \end{bmatrix}. \tag{3.14}$$

Capillary number ($\mathcal{C}a$)	1	0.7	0.5	0.3	0.1	0.05

Viscosity ratio (λ)	1	2.0	5.0	50.0

Pure shear	Simple shear
$\dot{\mathbf{E}}_{pure} = \begin{bmatrix} 1 & 0 \\ 0 & -1 \end{bmatrix}$	$\dot{\mathbf{E}}_{simple} = \begin{bmatrix} 0 & 1 \\ 0 & 0 \end{bmatrix}$

Table 3.1: Parameter space for the simulations. The evolution of the grain-melt aggregate is simulated for each type of shearing, six capillary numbers, and four viscosity ratios for a total of 52 simulations.

We carried out these two sets of numerical experiments for four different values of the viscosity ratio λ $(1.0, 2.0, 5.0, 50.0)$ and six different values of the capillary number $\mathcal{C}a$ $(1, 0.7, 0.5, 0.3, 0.1, 0.05)$. The parameter space explored in this chapter is summarized in Table 3.1. While the geometry of the deformed aggregates is controlled by the magnitude of strain, the viscosity ratio controls the time of deformation [*Hier-Majumder*, 2008]. To produce a high strain numerical experiment within a reasonable computation time, we employ viscosity ratios that are lower than natural values. This implies that our strain rates are higher than typical natural values. The resulting microstructure, however, is similar to what would be expected in natural aggregates with much higher viscosity ratio. We discuss this issue further in Section 3.4.

3.2.3 Post-processing

The numerical solutions to the BIE (3.11) and the kinematic condition (3.6) return the shape of each grain and the velocities at the boundary nodes of each

grain at each time step. We post-process the numerical data to calculate velocities in the interior of the grains and the melt, the differential shortening of each grain, and the contiguity tensor at each grain. In this section, we describe the method for calculating each of these quantities.

To visualize the coupled flow in the grain interior and the melt, we need to construct streamlines from the velocity vectors. Once the velocities along the boundaries are known, the velocity at a point $\boldsymbol{x}_0$ located in the melt is computed by

$$\begin{aligned} u_j(\boldsymbol{x}_0) =& u_j^{\infty}(\boldsymbol{x}_0) - \frac{1}{4\pi \mathcal{C}a} \sum_{p=1}^{P} \int_{\Gamma_p} \Delta f_i(\boldsymbol{x}) \mathcal{U}_{ij}(\boldsymbol{x}, \boldsymbol{x}_0) \, \mathrm{d}\Gamma_p \\ &+ \sum_{p=1}^{P} \frac{1-\lambda_p}{4\pi} \int_{\Gamma_p} u_i(\boldsymbol{x}) \mathcal{T}_{ijk}(\boldsymbol{x}, \boldsymbol{x}_0) \hat{n}_k(\boldsymbol{x}) \, \mathrm{d}\Gamma_p \qquad \boldsymbol{x}_0 \in \Omega_m. \end{aligned} \tag{3.15}$$

Notice that in contrast to the BIE (3.11), the velocity $u_i(\boldsymbol{x})$ in the integrand of the double-layer integral at the boundary Γ_p is now known along with the other terms on the right hand side. Thus, by choosing the location $\boldsymbol{x}_0$ at various points within the melt and repeating the calculation in equation (3.15), we can generate the representation of the flow field within the melt.

Similarly, the velocity at a point $\boldsymbol{x}_0$ within the q-th grain is given by

$$\begin{aligned} u_j(\boldsymbol{x}_0) =& \frac{1}{\lambda_q} u_j^{\infty}(\boldsymbol{x}_0) - \frac{1}{4\pi \lambda_q \mathcal{C}a} \sum_{p=1}^{P} \int_{\Gamma_p} \Delta f_i(\boldsymbol{x}) \mathcal{U}_{ij}(\boldsymbol{x}, \boldsymbol{x}_0) \, \mathrm{d}\Gamma_p \\ &+ \sum_{p=1}^{P} \frac{1-\lambda_p}{4\pi \lambda_q} \int_{\Gamma_p} u_i(\boldsymbol{x}) \mathcal{T}_{ijk}(\boldsymbol{x}, \boldsymbol{x}_0) \hat{n}_k(\boldsymbol{x}) \, \mathrm{d}\Gamma_p \qquad \boldsymbol{x}_0 \in \Omega_q. \end{aligned} \tag{3.16}$$

Since all quantities on the right hand side of equation (3.16) are known, we can calculate the velocity within each grain by repeating the calculation for different locations in the interior of the grain. We continue the process for other grains to compute the velocity field for a representative section of the aggregate. We generated streamlines from the known velocity fields using the visualization software Paraview.

The undeformed aggregate consists of equant, closely packed, hexagonal grains with an interstitial melt. During deformation, however, the grain shapes evolve in a nonuniform manner, driven by the magnitude of the applied far-field velocity. To observe such spatial and temporal variations of grain shape, we monitor the differential shortening, D, of each grain at each time step. The differential shortening is defined as a function of the lengths of major axis L and minor axis B of a grain,

$$D = \frac{L - B}{L + B}. \tag{3.17}$$

Differential shortening is zero when the grain is equant and approaches the value of one as the grain flattens to a line. Unlike aspect ratio, the differential shortening measurement is bounded with $0 \leq D < 1$.

To evaluate contiguity of each grain, we first need to evaluate the contact function on the grain surface. The contact function χ is a step function, which assumes the value of unity at the grain-grain contact and zero at the grain-melt contact [*Takei*, 1998]. To evaluate the contact function, we first compute the minimum

distance between a point, $\boldsymbol{x}$, on the p-th grain and all other grains as

$$d(\boldsymbol{x}) = \min_{q \neq p} dist(\boldsymbol{x}, \Gamma_q), \tag{3.18}$$

where $dist(\boldsymbol{x}, \Gamma_q)$ is the minimum Euclidean distance between a point $\boldsymbol{x}$ and an interface Γ_q. The contact function, $\chi(\boldsymbol{x})$, is given by

$$\chi(\boldsymbol{x}) = \begin{cases} 1 & \text{if } d(\boldsymbol{x}) < \epsilon \\ \\ 0 & \text{otherwise} \end{cases} . \tag{3.19}$$

If the distance is less than a prescribed threshold ϵ, we consider the p-th grain to be in contact with another grain at the point $\boldsymbol{x}$ on the boundary.

Once the contact function is evaluated on the surface of each grain, we calculate the contiguity tensor ψ_{ij} as

$$\psi_{ij} = \frac{1}{L} \int_{\Gamma_p} \chi(\boldsymbol{x}) \hat{n}_i(\boldsymbol{x}) \hat{n}_j(\boldsymbol{x}) \, \mathrm{d}\Gamma_p, \tag{3.20}$$

where L is the length of Γ_p, and $\hat{n}_i$ is the unit normal on the grain surface [*Takei*, 1998]. The trace of the contiguity tensor, ψ, is also numerically evaluated at each time step for each grain.

The anisotropy of the contiguity tensor is measured by ψ_1/ψ_2, where ψ_1 and ψ_2 are the smallest and largest eigenvalues of ψ_{ij}, respectively. By this definition, $\psi_1/\psi_2 = 1$ when the tensor is isotropic and decreases as the anisotropy in the tensor increases.

3.2.4 Numerical methods

In this section, we briefly present the steps associated with the numerical methods involved in the solution of the BIE. To reduce the BIE into a system of algebraic equations, we discretize the BIE using the method of collocation. During discretization, the singular integrals in the BIE need to be integrated using special integration techniques. Finally, we use the fast multipole expansion to provide a fast approximation of a matrix-vector multiplication for the dense system of algebraic equations resulting from the BIE. The details of each of these steps are discussed next.

We use the method of collocation to discretize the BIE in (3.11). For the p-th interface, we place n_p pole nodes on the grain-melt boundary Γ_p. A segment between two poles on the boundary is referred to as a boundary element. We approximate the position within each boundary element by cubic spline interpolation [*Press et al.*, 1992]. The interfacial surface tension $\Delta f_i(\boldsymbol{x})$ and unknown velocity $u_i(\boldsymbol{x})$ along the boundary are interpolated piecewise linearly over each boundary element.

The resulting linear system is rewritten in matrix notation as

$$\left(\frac{1+\lambda}{2}\mathbf{I} - \frac{1-\lambda}{4\pi}\mathbf{T}\right)\boldsymbol{u} = \boldsymbol{u}^{\infty} - \frac{1}{4\pi\mathcal{C}a}\mathbf{U}\Delta\boldsymbol{f}, \tag{3.21}$$

where $\mathbf{I}$ is the identity matrix, and the matrices $\mathbf{U}$ and $\mathbf{T}$ are generated from the kernels of the single- and double-layer integrals, respectively.

The method of collocation divides the interface of the p-th grain into n_p ele-

ments for which each $\boldsymbol{x}_0$ resides on at most two boundary elements. Thus, all but two of the boundary integrals on the p-th grain are regular for a given $\boldsymbol{x}_0$. Boundary integrals on the other particles are regular as well since by definition $\boldsymbol{x}_0 \notin \Gamma_q$ for $q \neq p$. These regular integrals are approximated using the eight point Gaussian quadrature rule.

When $\boldsymbol{x}_0$ is on $\Gamma_{p,e}$, the e-th boundary element on the p-th interface, the boundary integral becomes singular. For the single-layer integral, the singularity is weak, meaning the integrand is still integrable despite it being unbounded. The double-layer integral has a strong singularity and is only finite in the sense of Cauchy principal value. Special care must be taken when numerically evaluating the integrals in both cases. A variety of techniques have been developed to evaluate singular integrals [*Pozrikidis*, 2001; *Lean and Wexler*, 1985; *Guiggiani and Gigante*, 1990; *Lachat and Watson*, 1987; *Telles*, 1987; *Gao*, 2006]. Following *Hier-Majumder* [2008], we employ the radial integration method proposed by *Gao* [2006]. The radial integration method rewrites the integral in terms of the radial distance from the singularity and approximates the integrand by a power series. The power series form allows the regular and singular portions of the integrand to be separated at which point the singular integral is analytically shown to go to zero.

The FMM uses series expansions to approximate the matrix-vector multiplications in (3.21) [*Appel*, 1985; *Barnes and Hut*, 1986; *Ambrosiano et al.*, 1988; *Carrier et al.*, 1988; *Greengard and Gropp*, 1990; *Board and Schulten*, 2000]. The series expansions separate the pole and field points into two separate sets of equations. This removes the requirement for a unique evaluation for every combination

of pole point and boundary element. The end result is an approximate matrix-vector multiplication that takes $\mathcal{O}(N)$ time compared to $\mathcal{O}(N^2)$ time required by direct methods, where N is the total number of unknowns or the total degrees of freedom of the system of equations. The accelerated multiplication allows the use of iterative methods, such as the GMRES [*Saad*, 2003], to solve the linear system in $\mathcal{O}(N)$ time. *Liu* [2009] presents a general discussion on FMM expansion for BIEs arising from various physical problems. We present the FMM expansions for the single- and double-layer integrals Section 2.4.

We solved the resulting system of sparse linear equations using the GMRES method. We iterated the solver until the relative norm of the residual vector was less than 10^{-8}. As (3.11) is a Fredholm equation of the second type, the linear system is well conditioned and no preconditions were used. The solver converged within a maximum of 100 iterations for all geometries and values of λ and $\mathcal{C}a$ presented in this chapter. In our simulations, the number of GMRES iterations never reached the preset maximum of 1000 iterations.

We use an adaptive fourth order Runge-Kutta (RK4) method to update grain shapes from equation (3.6) using the velocities obtained from the BIE. In this adaptive scheme, the location of boundary nodes is updated using both one RK4 iteration of step size Δt and two RK4 iterations, each of step size $\Delta t/2$. If the L_1 norm of the difference between the pole positions for every node is less than 10^{-2}, then we use the result as the more refined evolution of the next time step. Otherwise, the process is repeated with $\Delta t/2$. When the time stepping scheme is successful, the next evolution attempts a time step of size $2\Delta t$, as long as the new larger time step

is not larger than the maximum allowed time step. Here, we choose our initial and maximum time step size to be $\Delta t = 0.01$.

The numerical solution was carried out using a Fortran 2008 library, using the Intel®Math Kernel Library (MKL) for linear algebra operations including the GMRES solver. The numerical results were validated against the Hadamard-Rybczyñski relation for a steady state viscous drop settling in an infinite fluid [*Kim and Karilla*, 2005; *Happel and Brenner*, 1983].

3.3 Results

In this section, we present the results from our numerical experiments in pure and simple shear. Our results from both pure and simple shear experiments demonstrate that the contiguity tensor becomes strongly anisotropic with progressive deformation. We also observe that the magnitude of the differential shortening of grains is strongly anticorrelated with the anisotropy in contiguity in time and space. During pure shear deformation, melt is expelled from tubules wetting grain boundaries parallel to the principal compressive strain. During simple shear deformation, such grain boundary wetting takes place along planes oriented in a sense antithetic to the shear direction. We elaborate these key findings in the following subsections. The results from our microstructural analysis contain the shape and contiguity of each grain during each step of deformation, not obtainable by previous experimental and numerical techniques.

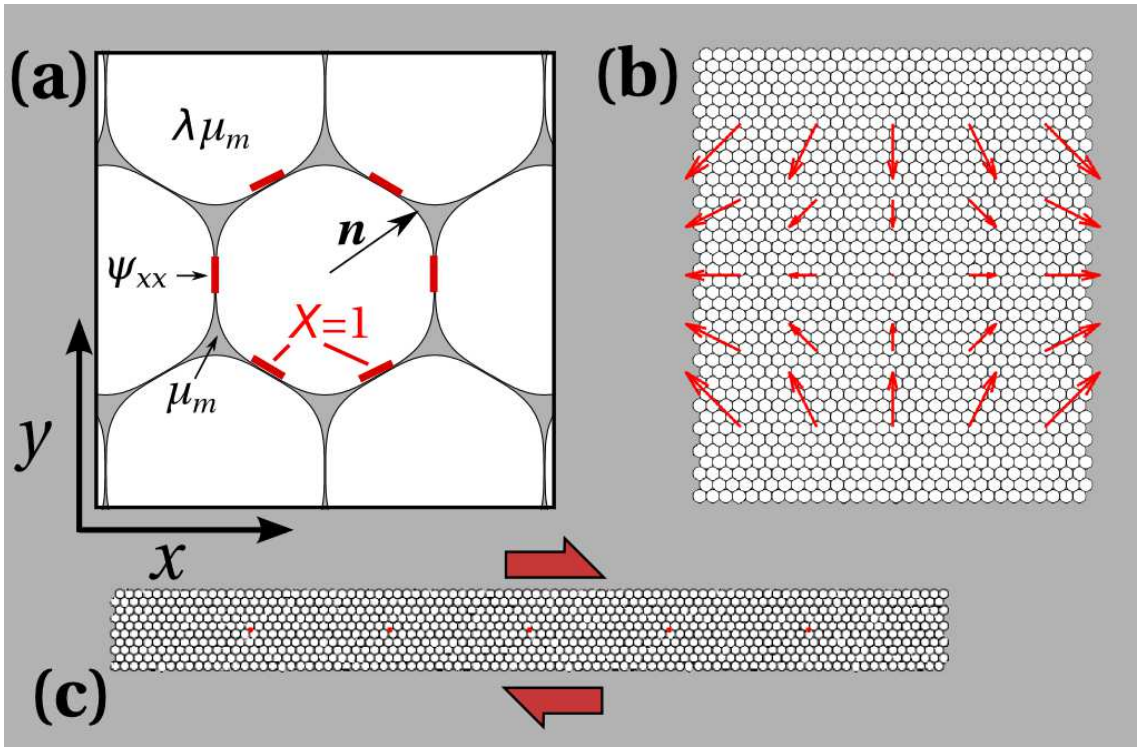

Figure 3.1: Setup for numerical experiments. (a) Initial geometry of a grain surrounded by six other grains and interstitial melt in gray at three grain junctions. The unit normal to the grain interface $\hat{n}_k(\boldsymbol{x})$, the contact function χ, and the ψ_{xx} component of the contiguity tensor are also shown in the diagram. Viscosity of the melt is μ_m, while that of the grain is $\lambda\mu_m$. (b) The initial configuration of the entire aggregate prior to the pure shear experiment. The aggregate consists of 1200 grains arranged in 40 rows and 30 columns. The red lines indicate the imposed external flow. (c) The initial configuration for simple shear experiment. The aggregate consists of 900 grains arranged in 10 rows and 90 columns. The sense of applied shear, as depicted by the bold red arrows, is dextral.

3.3.1 Pure shear deformation

When deformed in pure shear, melt from tubules in three grain corners is expelled, wetting grain boundaries oriented parallel to the direction of principal compressive strain. The synthetic micrographs in Figure 3.2 demonstrate the influence of deformation on two different aggregates with different values of λ. In 3.2(a), we compare the aggregates before and after deformation. In Figure 3.2(b), we display an enlarged view of the synthetic microstructure containing a few grains. Com-

parisons between the microstructure in 3.2(b) and the microstructure in Figure 3.1 reveal a few developments caused by deformation. The equal lengths of intergranular contact in the undeformed aggregate transformed into substantially reduced length of intergranular contact in the vertical direction in Figure 3.2(b), while the length of intergranular contact in the subhorizontal direction has increased. The distance between melt pockets along the vertical boundaries in Figure 3.2(b) is negligible, resulting in grain boundary melt films oriented along the vertical direction, which is also the direction of the principal compressive strain. This result is qualitatively similar to the experimental observations of *Daines and Kohlstedt* [1997], where they observed that initially equant melt pockets became strongly elongated along the direction of the principal compressive stress. The synthetic micrographs in Figure 3.2(c) and (d) outline the evolution of the microstructure for a higher viscosity ratio after the same amount of computational time. For the higher viscosity ratio aggregate, deformation and microstructural development is much less pronounced for the same length of computational time.

During deformation, the flow within the grains and the melt are strongly coupled. The synthetic micrographs in Figure 3.3 compare the microstructure before and after deformation for the cases discussed above. To demonstrate the nature of the coupled flow, the synthetic micrographs are overlain with streamlines colored by the magnitude of nondimensional velocity. The grain in the center of the micrographs is also located in the center of the 1200 grain aggregate. In Figures 3.3(a) and (b), streamlines continue from one grain to another and to the melt phase without distortion both before and after deformation. In these micrographs, the grains

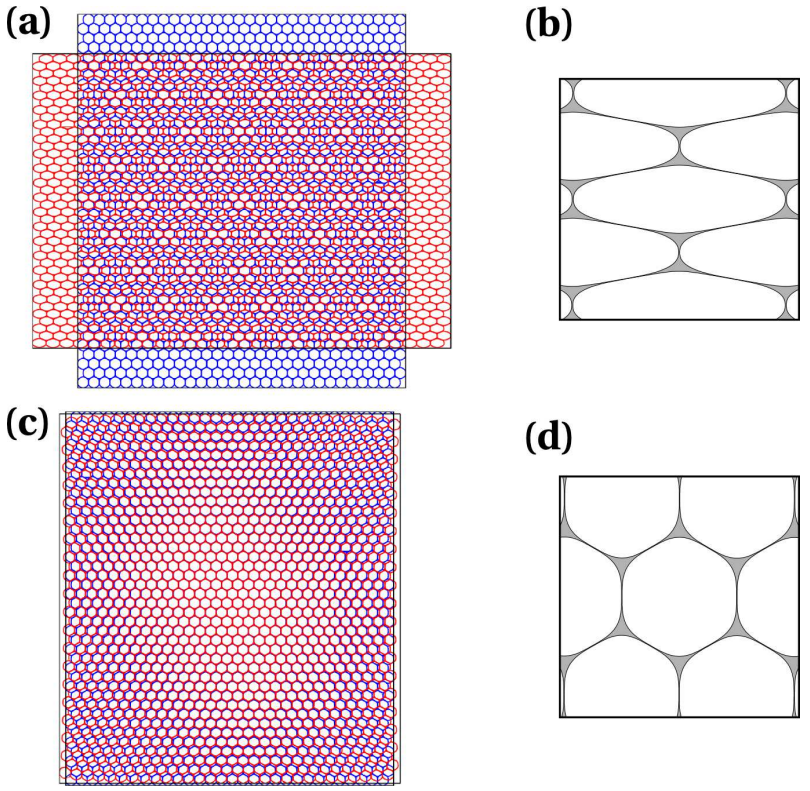

Figure 3.2: (a) Comparison between the deformation of a low viscosity ratio, $\lambda = 1.0$, grain-melt aggregate at the beginning and end of a simulation in a pure shear flow. The aggregate is colored blue at the start of the evolution and red at the end. Bounding boxes are added to emphasize the overall deformation of the aggregate. (b) A sample grain-melt patch with low viscosity ratio, $\lambda = 1.0$, at the end of a simulation in a pure shear flow. The gray areas between the grains represent the melt. (c) Comparison between the deformation of a high viscosity ratio, $\lambda = 50.0$, grain-melt aggregate at the beginning and end of a simulation in a pure shear flow. The aggregate is colored blue at the start of the evolution and red at the end. Bounding boxes are added to emphasize the overall deformation of the aggregate. (d) A sample grain-melt patch with low viscosity ratio, $\lambda = 50.0$, at the end of a simulation in a pure shear flow. The gray areas between the grains represent the melt.

and the melt phase have the same viscosity and thus respond in a similar way to the imposed flow. In contrast, the flow lines display remarkable contrast between the grains and the melt phase in Figures 3.3(c) and (d). The warmer color of the streamlines within the melt phase in Figure 3.3(d) suggests a stronger magnitude of segregation between the melt and the matrix in this case.

Grain deformation and the development of anisotropy in contiguity are strongly related. The synthetic micrographs in Figure 3.4 compare the differential shortening and the ratio between the principal components of contiguity near the beginning and the end of deformation. Comparisons between the maps of D and ψ_1/ψ_2 in both undeformed and deformed states reveal that the least deformed grains, characterized by smaller values of D, are also most isotropic, characterized by higher values of ψ_1/ψ_2. While the magnitude of these variations at a given state of strain are rather small, as revealed by the small range on the color scale, the pattern remains unchanged by deformation. We also notice that the average magnitude of the quantities differs substantially between the top and the bottom panels, resulting from deformation of the aggregates. The spatial pattern is caused by the gradient of the imposed velocity which becomes zero at the center of the aggregate. Consequently, the role of deformation is least pronounced at the center.

3.3.2 Simple shear deformation

In simple shear deformation, melt is expelled from the tubules to wet grain boundaries that are oriented in an antithetic sense to the applied shear strain. The

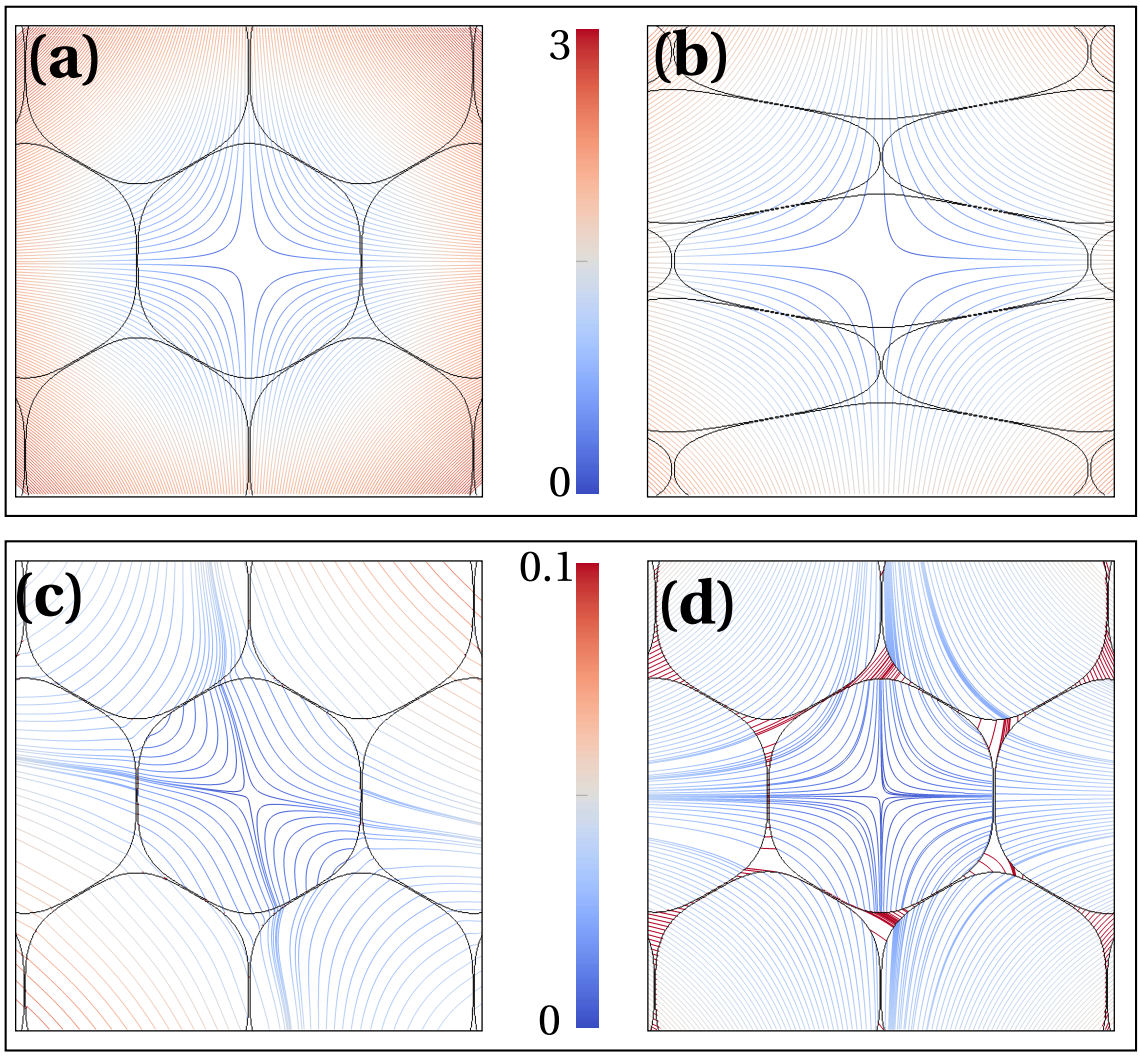

Figure 3.3: Streamlines indicating flow velocities within the grains and the melt pocket. In the top panel, streamlines (a) at the onset and (b) at the end of the numerical experiment are drawn for $\lambda = 1$ and $\mathcal{C}a = 1$. In the lower panel, streamlines (a) at the onset of deformation and (b) at the end of deformation are drawn for $\lambda = 50$ and $\mathcal{C}a = 1$. The streamlines are colored by the magnitude of dimensionless velocity.

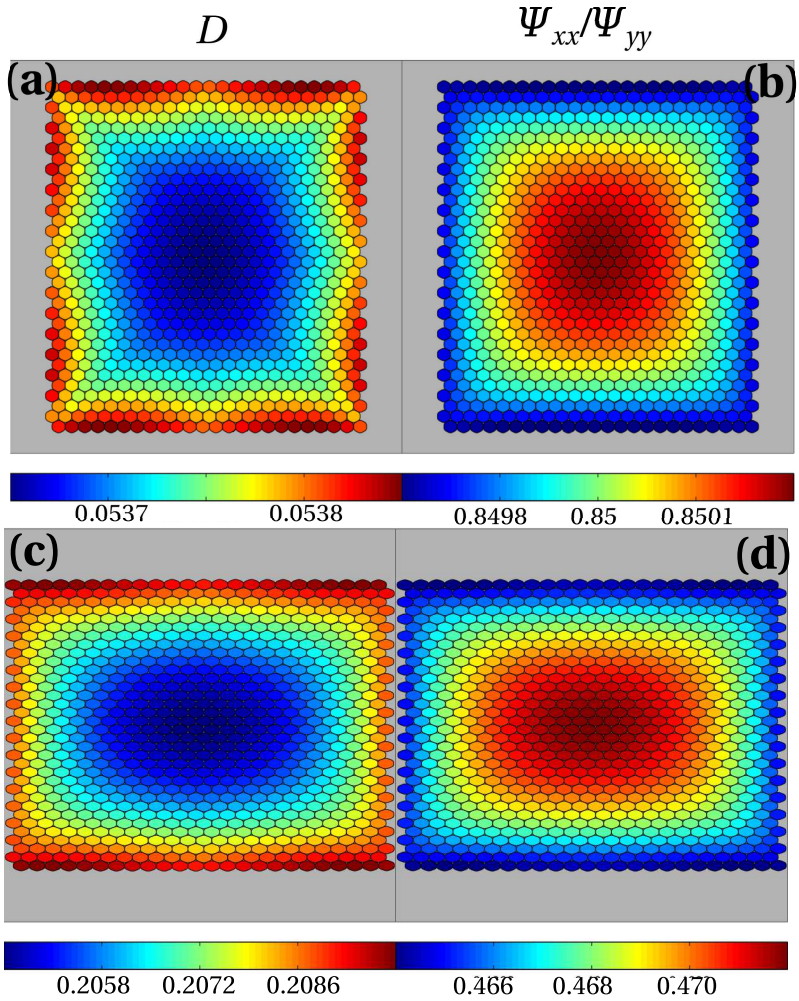

Figure 3.4: (a) and (b) Values of deformation and anisotropy in the contiguity tensor at the start, $t = 0.2$, of a simulation. (c) and (d) Values of deformation and anisotropy in the contiguity tensor at the end, $t = 1.0$, of a simulation. All subfigures are from a pure shear simulation with $\mathcal{C}a = 1.0$ and $\lambda = 1.0$. A heat map is used to show the values of grain properties for a selection of inner grains of the grain-melt aggregate. (a) and (c) show the value of differential shortening, $D = (L - B)/(L + B)$, for each grain, where L is the length of the major axis and B is the length of the minor axis of the grain. (b) and (d) show anisotropy of the contiguity tensor as measured by the ratio between the normal components of the contiguity tensor, ψ_1/ψ_2. The gray patches between the grains and gray area surrounding the aggregate represent the melt.

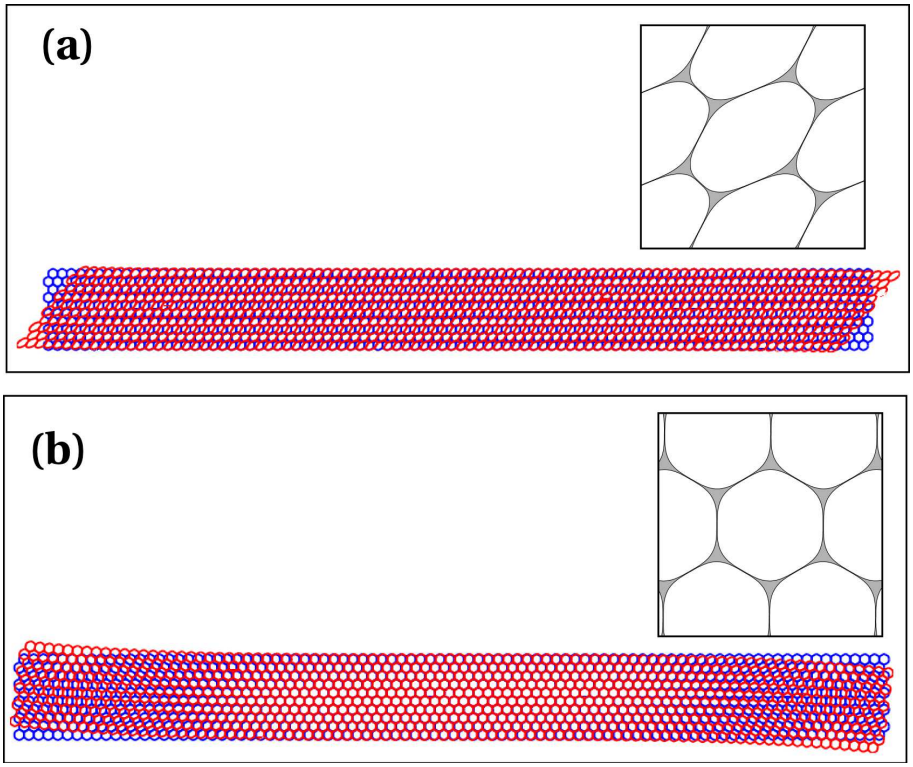

Figure 3.5: (a) Comparison between the deformation of a low viscosity ratio, $\lambda = 1.0$, grain-melt aggregate at the beginning and end of a simulation in a pure shear flow. The aggregate is colored blue at the start of the evolution and red at the end. The top right portion of (a) shows a sample grain-melt patch with low viscosity ratio, $\lambda = 1.0$, at the end of a simulation in a pure shear flow. The gray areas between the grains represent the melt. (c) Comparison between the deformation of a high viscosity ratio, $\lambda = 50.0$, grain-melt aggregate at the beginning and end of a simulation in a pure shear flow. The aggregate is colored blue at the start of the evolution and red at the end. The top right portion of (b) shows a sample grain-melt patch with low viscosity ratio, $\lambda = 50.0$, at the end of a simulation in a pure shear flow. The gray areas between the grains represent the melt.

synthetic micrographs in Figure 3.5 demonstrate the grain boundary wetting for two different viscosity contrasts. The aggregate in Figure 3.5(a) is deformed by a dextral shear, moving the top of the aggregate to the right. The enlarged microstructure in the inset demonstrates that the grains are elongated along an axis oriented from top right to bottom left of the window. We also notice that length of contact is substantially decreased along grain boundaries oriented in a direction perpendicular to the stretching of the grains. This observation is qualitatively similar to the experimental observations of grain boundary wetting by simple shear and torsion [*Hier-Majumder and Kohlstedt*, 2006; *King et al.*, 2011; *Zimmerman et al.*, 1999]. As observed with the pure shear case, the aggregate with the higher viscosity contrast deformed to a much smaller extent for the same length of computational time.

Similar to the pure shear case, flow within the grains and the melt are strongly coupled. The flow lines in Figure 3.6 demonstrate the nature of such coupling in an enlarged view of a few grains whose centers are aligned along the x axis. In all four panels, the direction of the velocity changes from the top (flowing to the right) to the bottom (flowing to the left) of the synthetic micrographs. The top two panels, Figures 3.6(a) and (b) illustrate the development of sheared microstructure at the beginning and the end of the deformation. The streamlines continue from one grain to another and the melt without any significant bends, as all of these phases have the same viscosity. The grains in the middle row in Figure 3.6(b) develop elliptical closed loop circulation in the center in response to the reversal of the direction of the flow velocity. We do not observe any appreciable deformation of the high viscosity grains in Figure 3.6(c) and (d). The streamlines, however, display kinks as they

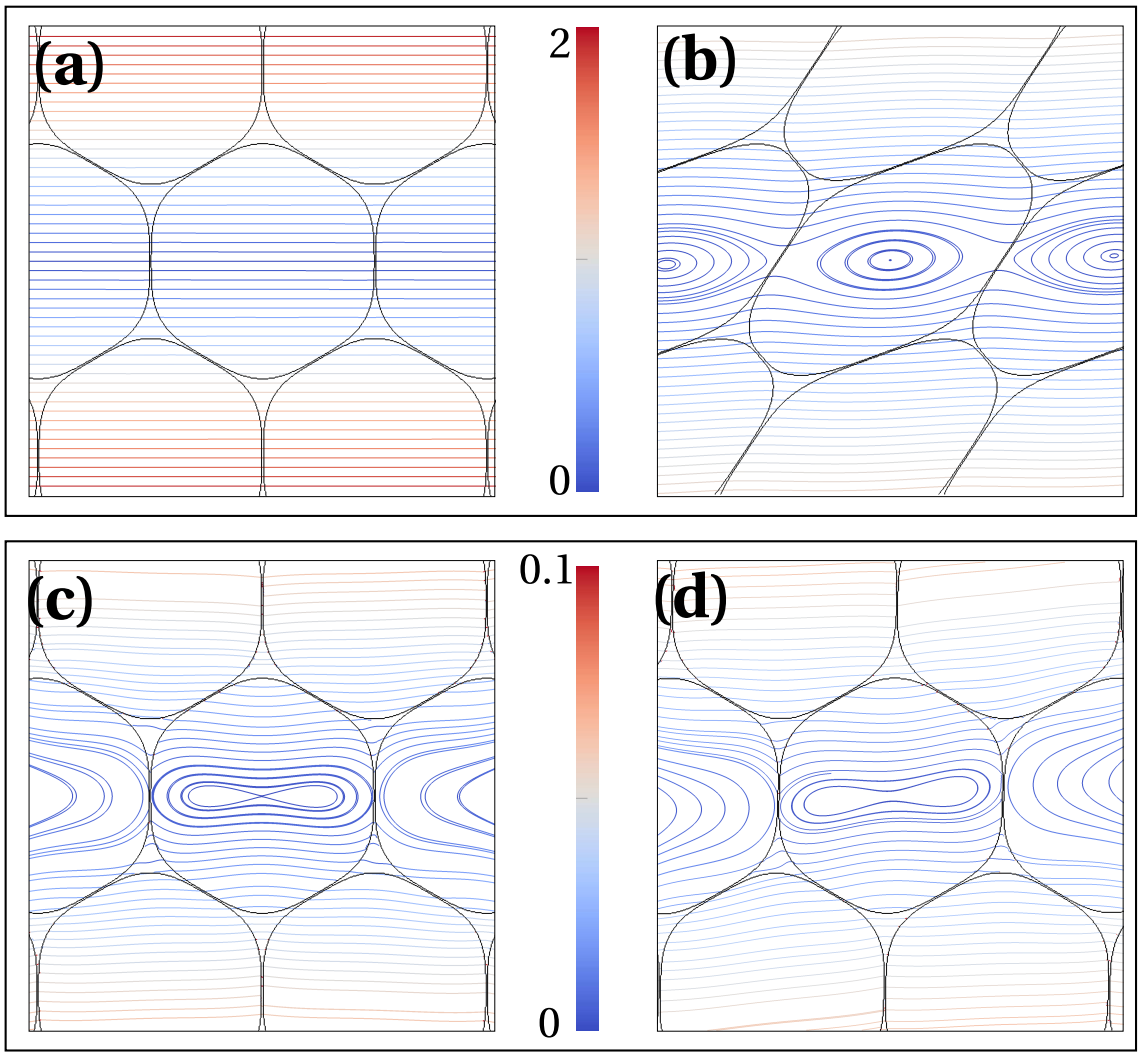

Figure 3.6: Streamlines indicating flow velocities within the grains and the melt pocket. In the top panel, streamlines (a) at the onset and (b) at the end of the numerical experiment are drawn for $\lambda = 1$ and $\mathcal{C}a = 1$. In the lower panel, streamlines (c) at the onset of deformation and (d) at the end of deformation are drawn for $\lambda = 50$ and $\mathcal{C}a = 1$. The streamlines are colored by the magnitude of dimensionless velocity.

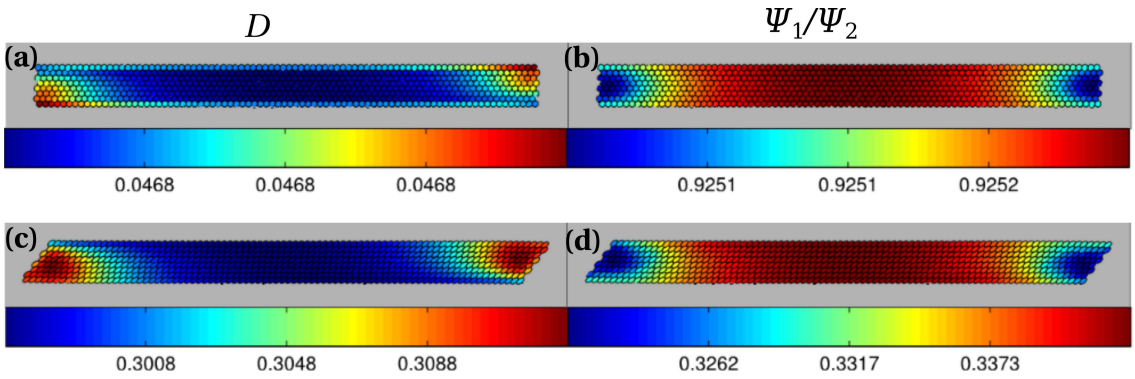

Figure 3.7: (a) and (b) Values of deformation and anisotropy in the contiguity tensor at the start, $t = 0.2$, of a simulation. (c) and (d) Values of deformation and anisotropy in the contiguity tensor at the end, $t = 1.0$, of a simulation. All subfigures are from a simple shear simulation with $\mathcal{C}a = 1.0$ and $\lambda = 1.0$. A heat map is used to show the values of grain properties for a selection of inner grains of the grain-melt aggregate. (a) and (c) show the value of differential shortening, $D = (L - B)/(L + B)$, for each grain, where L is the length of the major axis and B is the length of the minor axis of the grain. (b) and (d) show anisotropy of the contiguity tensor as measured by the ratio between the normal components of the contiguity tensor, ψ_1/ψ_2. The gray patches between the grains and gray area surrounding the aggregate represent the melt.

move from the grains into the melt pockets. The kinks in the streamlines, similar to the pure shear case, are caused by the contrast in viscosity.

The differential shortening and anisotropy increase with an increase in the strain. The magnitude of both quantities is inversely related in space and time, as revealed by the maps in Figure 3.7. The top panels display the differential shortening, D (Figure 3.7(a)), and anisotropy of contiguity, ψ_1/ψ_2 (Figure 3.7(b)), at the onset of deformation. In this state, D shows variation $\mathcal{O}(10^{-5})$ about a mean value of 0.05. After deformation, however, the mean differential shortening increases to 0.3 in Figure 3.7(c), with the higher values concentrated near the ends. Although the $\mathcal{O}(10^{-3})$ spatial variation in the magnitude of D is small, the pattern is anticorrelated with the same order of magnitude variations in the anisotropy of contiguity in Figure 3.7(d). Notice also the sharp reduction in the average value

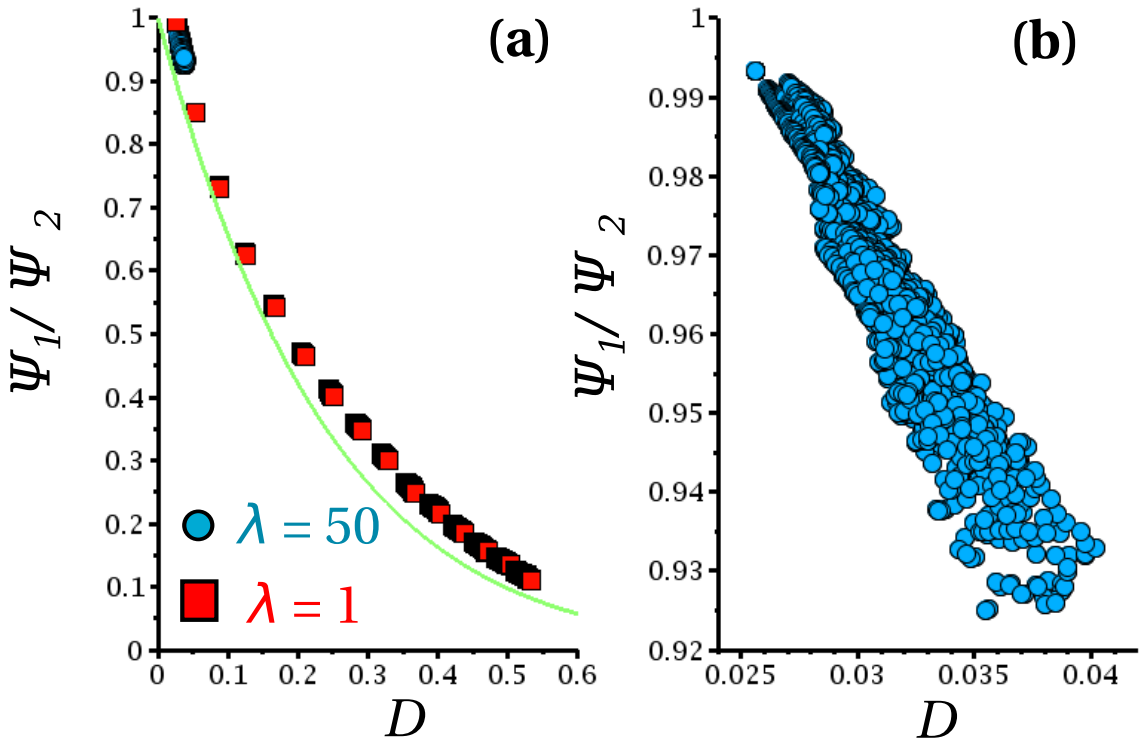

Figure 3.8: (a) Best fit between the anisotropy of the contiguity tensor, ψ_1/ψ_2, and differential shortening, D, for the pure shear simulations. The blue dots represent measurements of grains from simulations where $\lambda = 50.0$ and $\mathcal{C}a = 1.0$. The red dots represent measurements of grains from simulations where $\lambda = 1.0$ and $\mathcal{C}a = 1.0$. The relationship is given by $\psi_1/\psi_2 \sim \exp(-3.909D^2 - 1.005D)$ with $R^2 = 0.998$. (b) A zoomed in view of the high viscosity data points from (a).

of ψ_1/ψ_2 from 0.9 before deformation (3.7 (b)) to a value of 0.3 after deformation. Similar to the observation from pure shear experiments, these results depict the grain scale correlation between deformation and generation of anisotropic contiguity.

The negative correlation between the magnitudes of anisotropy in contiguity and differential shortening is revealed when these two quantities are continually tracked during the course of a deformation experiment. The plots in Figure 3.8 display this pattern. In the plots in Figure 3.8(a), we compare the values of ψ_1/ψ_2 and D calculated from each grain at each level of shortening, from two different pure shear experiments. The plot reveals that the nature of anticorrelation is strongly

nonlinear. Also overlain on the plot is a fit to the data $\psi_1/\psi_2 = e^{-3.909D^2-1.005D}$. The plot in Figure 3.8(b) displays the values for $\lambda = 50$ only. Although deformed to smaller strains, the strong negative correlation is obvious from the plot. The fact that data from both low and high viscosity contrast aggregates in Figure 3.8(a) follow the same trend demonstrates that the geometric parameters such as differential shortening and anisotropic contiguity are nearly insensitive to the viscosity ratio at the same stage of deformation. We discuss this issue further in the next section.

3.4 Discussion

3.4.1 Trade-offs in selection of parameters

An important advantage of our microgeodynamic model lies in the ability to track a large quantity of information for each grain during the course of deformation. The implementation of FMBEM allows us to retrieve this information without unrealistic costs of computation. The range of viscosity ratio, λ, explored in this study is substantially smaller than the values observed in nature. The smaller values of λ in our simulations allow us to observe and quantify the development of anisotropy in a reasonable computation time. Despite the short timescale, the final microstructural parameters at a given stage of state were relatively insensitive to the viscosity ratio.

The plots in Figure 3.9 demonstrate the evolution of anisotropy and differential shortening with increasing strain. The plots in Figure 3.9(a) illustrate that the ratio ψ_1/ψ_2 decreases with the strain in a nonlinear fashion. The superposition of two sets of data illustrates that for a comparable strain, the influence of the viscosity

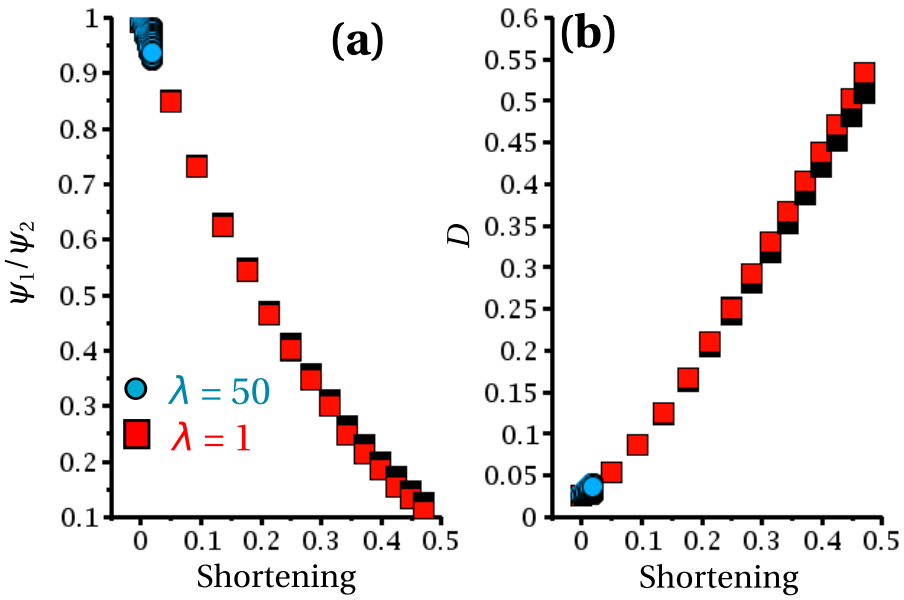

Figure 3.9: Development of anisotropic textures in pure shear experiments. (a) Plot of anisotropy in contiguity ψ_1/ψ_2 as a function of bulk strain for viscosity ratios $\lambda = 1$ (red squares) and $\lambda = 50$ (blue circles). (b) Plot of differential shortening as a function of bulk strain for viscosity ratios $\lambda = 1$ (red squares) and $\lambda = 50$ (blue circles).

contrast on the anisotropic contiguity is insignificant. The plots in Figure 3.9(b) demonstrate the differential shortening increases as the grains deform into elongated shapes with an increase in strain. As in Figure 3.9(a), for a given strain the influence of viscosity ratio on the differential shortening is minimal.

3.4.2 Comparison with previous results

The results from our work is in great qualitative agreement with a number of previous works. In a set of laboratory experiments, *Daines and Kohlstedt* [1997] deformed partially molten aggregates of olivine and basalt in pure shear. Studying the microstructures of the deformed samples, they observed that the initially equant melt pockets became more elongated with deformation. They also observed that these films aligned themselves in a direction parallel to the direction of principal

compressive stress. This observation is similar to our synthetic micrographs where grain boundaries parallel to the principal shortening direction and perpendicular to the x axis are preferentially wetted resulting in elongated film-like melt units. Since the work of *Daines and Kohlstedt* [1997] did not report contiguity or differential shortening from their microstructures, direct quantitative comparison between these two works is difficult.

In a set of laboratory experiments with analogue materials, *Takei* [2005] observed the development of shear wave anisotropy during deformation. The samples were deformed in pure shear configuration while alternating between the principal compressive and extensive stress. In this work, *Takei* [2005] reports average values of contiguity ψ from the deformed aggregates. The scalar contiguity, the trace of the contiguity tensor from our pure shear experiments, is similar to these reported values. We present quantitative comparisons between these two works in Chapter 4. Qualitatively, the orientation of grain boundary films in relation to the principal compressive stress in these experiments is also similar to our pure shear experiments.

3.5 Conclusion

The results from our numerical experiments demonstrate that melt is expelled from grain edge tubules to grain boundary films during deformation. In pure shear configuration, the orientation of these films is parallel to the direction of the principal compressive stress. In simple shear, these films are oriented in a sense antithetic to the sense of applied shear. The results from our microgeodynamic model also

demonstrate that the magnitudes of anisotropic contiguity and differential shortening display a strongly nonlinear negative correlation. Such a correlation is revealed both in spatial distribution and temporal evolution of these quantities with progressive deformation. We also demonstrate that the flow between the grains and the interstitial melt phase are strongly coupled during deformation.

Chapter 4: Development of Anisotropic Contiguity in Deforming Partially Molten Aggregates II: Implications for the Lithosphere-Asthenosphere Boundary

4.1 Introduction

Deformation of partially molten aggregates plays an important role in grain scale redistribution of melt. After deformation, the initially isotropic network of grain edge tubules becomes anisotropic as the melt preferentially wets grain boundaries oriented parallel to the principal compressive stress [*Daines and Kohlstedt*, 1997; *Takei*, 2005]. Such a transformation of the microstructure of the melt also renders contiguity, the fractional area of intergranular contact, anisotropic. As the elastic strength of the aggregate depends on the area of contact between adjacent, load-bearing grains, development of anisotropy in contiguity renders the effective elastic strength anisotropic, even if the solid matrix is isotropic.

Direct observation of the evolution of anisotropy of contiguity and shear wave speed during the course of deformation was previously precluded by the setup of laboratory experiments and prohibitive computational cost of numerical models. Here, we present the results from a Fast Multipole Boundary Element Method (FMBEM)

based model that addresses the shortcomings of previous numerical models. In this work, we model the deformation of partially molten aggregates in pure and simple shear while tracking the information on shape and contiguity of each grain during each time step of the numerical experiment. In Chapter 3, we present the numerical methods and synthetic microstructures. In this chapter, we focus on the implications of our results on the Earth's Lithosphere-Asthenosphere Boundary (LAB).

The LAB is an ideal place to study the coupling between deformation and melt geometry. Results from experimental petrology indicate small amounts of melt, possibly less than 1 vol%, can exist in conditions similar to the LAB [*Sifré et al.*, 2014]. Dynamic coupling between the motion of lithospheric plates and the underlying asthenosphere will produce large amounts of deformation in the LAB, inducing strong anisotropy in the geometry of this melt [*Holtzman and Kendall*, 2010; *Kawakatsu et al.*, 2009]. The physical properties of this deformed, anisotropic aggregate should be able to explain the seismic and electric signature of the LAB.

A number of constraints can be placed on the nature of the LAB from its seismic and electric signature. Multiple studies indicate that despite regional variations, the LAB is characterized by a relatively sharp reduction in shear wave speed over a short depth range [*Schmerr*, 2012; *Fischer et al.*, 2010; *Rychert et al.*, 2010]. Another feature of the LAB is seismic anisotropy on global [*Nettles and Dziewoski*, 2008] and regional scales [*Holtzman and Kendall*, 2010]. Magnetotelluric studies reveal that the LAB is characterized by a nearly horizontal channel of elevated electrical conductivity [*Evans et al.*, 2005; *Naif et al.*, 2013]. If partially molten, the interaction between deformation and redistribution of the melt should be able to

explain these observed signatures of the LAB.

We explore the nature of the LAB from a microstructural perspective. In Chapter 3, we demonstrate that the anisotropy in contiguity displays a strongly nonlinear increase as deformation progresses. In this chapter, we combine our results of anisotropic melt geometry with a mineral physics database using an averaging scheme to calculate the development of shear wave anisotropy during the course of deformation. We also compare the seismic signature of melt distributed in tubules with that of melt films created by grain boundary wetting.

This chapter is divided into the following sections. First, we present the methods for calculating the shear wave speeds and anisotropy from our numerical data. Next, we discuss the evolution of the calculated seismic signature as a function of deformation. Finally, we discuss the implications of our study on the nature of seismic velocities and anisotropy in the LAB.

4.2 Methods

In this work, we use our numerical data to calculate the shear wave anisotropy. To estimate the effect of deformation in shear wave speed reduction and anisotropy generation, we also present predicted profiles of shear wave speed using the numerical code MuMaP [*Hier-Majumder et al.*, 2014]. In this section, we present a brief description of the numerical methods from Chapter 3 that were used to calculate the contiguity, followed by a derivation for calculating shear wave anisotropy from numerical values of contiguity, and a short summary of the technique used to build

profiles of shear wave speed using MuMaP.

4.2.1 Numerical model

In the microgeodynamic model of Chapter 3, we carry out two sets of numerical experiments. In each set, the partially molten aggregate was modeled as a collection of two dimensional, tightly packed hexagonal grains with an interstitial melt phase. During the deformation of this aggregate under an applied, constant strain rate, the grains and the melt deform in a viscous manner. We take the Partial Differential Equations (PDEs) governing the conservation of mass and momentum within each grain and convert these PDEs into a Boundary Integral Equation (BIE) for each grain and melt phase. The vector BIE for the j-th component of the unknown velocity $u_j(\boldsymbol{x}_0)$ at a point $\boldsymbol{x}_0$ on the boundary of the q-th grain is given by

$$u_j(\boldsymbol{x}_0) = \frac{2}{1+\lambda_q}\left[u_j^{\infty}(\boldsymbol{x}_0) - \frac{1}{4\pi\mathcal{C}a}\sum_{p=1}^{P}\int_{\Gamma_p}\Delta f_i(\boldsymbol{x})\mathcal{U}_{ij}(\boldsymbol{x},\boldsymbol{x}_0)\,\mathrm{d}\Gamma_p + \sum_{p=1}^{P}\frac{1-\lambda_p}{4\pi}\int_{\Gamma_p}^{\mathcal{PV}} u_i(\boldsymbol{x})\mathcal{T}_{ijk}(\boldsymbol{x},\boldsymbol{x}_0)\hat{n}_k(\boldsymbol{x})\,\mathrm{d}\Gamma_p\right] \qquad \boldsymbol{x}_0 \in \Gamma_q, \tag{4.1}$$

where λ_p is the ratio of viscosities between the p-th grain and the melt, u_j^{∞} is an applied far-field velocity, Δf_i arises from tension at the surface of the grain, the second rank Stokeslet tensor $\mathcal{U}_{ij}$ arises from the response of the flow to surface tension, the third rank Stresslet tensor $\mathcal{T}_{ijk}$ arises from the contributions due to deformation within the grains, and $\hat{n}_i$ is the unit normal vector along the boundary of the p-th grain pointing into the melt. The nondimensional capillary number $\mathcal{C}a$

is the ratio between the forces of surface tension and deformation. In this analysis, we present results for $\lambda = 1$ and $\mathcal{C}a = 1$.

The shape of the p-th grain responds to the applied deformation. To ensure the volume of each grain is conserved, the shape function, F^p, evolves following the kinematic relation,

$$F^p_{,t}(\boldsymbol{x}, t) + u_i(\boldsymbol{x}, t) F^p_{,i}(\boldsymbol{x}, t) = 0. \tag{4.2}$$

As the shape of the grain evolves, so does the contiguity. The contiguity tensor for the p-th grain at any time is given by

$$\psi^p_{ij} = \frac{1}{L} \int_{\Gamma_p} \chi(\boldsymbol{x}) \hat{n}_i(\boldsymbol{x}) \hat{n}_j(\boldsymbol{x}) \, \mathrm{d}\Gamma_p, \tag{4.3}$$

where L is the length of Γ_p [*Takei*, 1998], and $\hat{n}_i$ is the unit normal which is numerically evaluated from F^p at each time step. The quantity $\chi(\boldsymbol{x})$ is the contact function [*Takei*, 1998], which assumes a value of unity at the grain-grain contact and zero at the grain melt contact. The trace of the contiguity tensor, ψ, is also numerically evaluated at each time step for each grain.

We carry out numerical experiments in a pure shear and simple shear setup. For the pure shear experiments, the aggregate consists of 1200 grains arranged in 40 rows and 30 columns, while the simple shear experiments are conducted on an aggregate of 900 grains arranged in 10 rows and 90 columns. The detailed numerical methods are presented in Chapter 3. For the seismic analysis in this chapter, we use

the values of the components of the contiguity tensor, the eigenvalues, and the trace from the numerical experiment. We then average the values of these quantities over all grains at any given time step. These averaged values are then used to calculate the development of anisotropic contiguity and shear wave anisotropy as a function of increasing strain.

4.2.2 Calculation of shear wave speed and anisotropy

In a deforming, partially molten aggregate, anisotropy is produced by (a) deformation of individual grains along dominant slip planes, and (b) by redistribution of melt into an anisotropic geometry. Deformation of crystals along specific slip planes and the resultant Lattice Preferred Orientation (LPO) can exert significant influence in the anisotropy of the structure. While the general technique, outlined below is able to address both sources of anisotropic texture, in this work we assume that the viscosity of the grains remains constant, leading to a Newtonian rheology. In crystals, such behavior is achieved by deformation in the diffusion creep regime. In this regime, slip of dislocations and generation of an LPO is suppressed. Consequently, in our analysis, following the works of *Takei* [1998] and *Takei* [2005], we assume that the anisotropy is caused only by the anisotropic distribution of melt geometry. The work of *Holtzman and Kendall* [2010] outlines the competition between these two effects.

Consider an initially isotropic partially molten aggregate in the $x-y$ plane. As this aggregate is deformed, the components of the contiguity tensor change, leading

to a change in the shear wave speed based on the direction of polarization. For example, the shear wave traveling in the z direction while vibrating along the i-th direction in the $x-y$ plane will experience a reduction in shear wave speed, δV_{Si}, given by

$$\frac{\delta V_{Si}}{V_{Si}^{eq}} = \frac{\delta\psi_{ii}}{2\psi}\frac{S_{zizi}^{eq} - S_{zizi}^{s}}{S_{zizi}^{eq}} \qquad i = x, y, \tag{4.4}$$

where ψ_{ii} is the component of the contiguity tensor on the face perpendicular to the i axis, ψ is the trace of the contiguity tensor, V_{Si}^{eq} is the shear wave speed in the undeformed aggregate, and S_{ijkl} is the elastic compliance tensor. Assuming both the solid (superscript $m = s$) and the undeformed, partially molten matrix (superscript $m = eq$) are isotropic, the compliance tensors are defined as [*Takei*, 1998]

$$S_{ijkl}^{m} = \frac{1}{9k_m}\delta_{ij}\delta_{kl} + \frac{1}{4\mu_m}\left[\delta_{ik}\delta_{jl} + \delta_{il}\delta_{jk} - \frac{2}{3}\delta_{ij}\delta_{kl}\right], \tag{4.5}$$

where δ_{ij} is the Kronecker delta, k_m is the bulk modulus, and μ_m is the shear modulus. For the solid matrix, k_s and μ_s simply represent the temperature, pressure, and composition dependent bulk and shear moduli. For the partially molten matrix, the effective compliance tensor, S_{ijkl}^{eq}, is sensitive to the interconnection between the load bearing grains through the contiguity in the undeformed state. Using this definition of the compliance tensor, we can show that the last term on the right

hand side of equation (4.4) becomes

$$\frac{S^{eq}_{zizi} - S^{s}_{zizi}}{S^{eq}_{zizi}} = 1 - \frac{\mu_{eq}}{\mu_s}. \tag{4.6}$$

Following the parameterization of *Takei* [2002], we can express the quantity on the right hand side of equation (4.6) as

$$1 - \frac{\mu_{eq}}{\mu_s} = (1 - \psi)^n \,, \tag{4.7}$$

where the exponent n is also a function of the trace of contiguity ψ.

Combining (4.4) through (4.7), we find the simplified relation for the variations in the seismic wave speed as

$$\delta V_{Si} = V^{eq}_{Si} \left[\frac{\delta \psi_{ii}}{2\psi} \right] (1 - \psi)^n \,, \tag{4.8}$$

where $i = x, y$. The quantity within square brackets on the right hand side of equation (4.8) represents the contribution of anisotropic contiguity in shear wave splitting. If the contiguity is the same as the undeformed or equilibrium stage, $\delta\psi_{ii} = 0$, leading to $\delta V_{Si} = 0$. In this analysis, we assume that $V^{eq}_{zx} = V^{eq}_{Si} = V_0(\phi, \psi)$, where ϕ is the melt volume fraction. This formulation directly relates anisotropy in the microstructure, $\delta\psi_{ii}$, to the anisotropy in shear wave speed, δV_{Si}. Using the formulation of *Takei* [2002], we can calculate $V_0(\phi, \psi)$ for a known melt fraction and contiguity. In our numerical experiments, we calculated the scalar contiguity, ψ, and four components of the contiguity tensor ψ_{ij}, for all grains at each time step.

In the absence of deformation, the shear wave speed through the partially molten aggregate at a given depth is controlled by the elastic properties of the solid and melt, the potential temperature, and the bulk solid composition. In the equilibrium assemblage, the influence of melt on the shear wave speed is controlled by the melt geometry and the volume fraction.

We use the numerical model MuMaP [*Hier-Majumder et al.*, 2014] to create vertical profiles of shear wave speed. The elastic properties of the reference mantle were obtained from the work of *Xu et al.* [2008] for mantle potential temperatures of 1300 K and 1500 K and a basalt fraction of 0.2 in the bulk composition. We use the equation of state for 5% carbonated peridotite from *Ghosh et al.* [2007] to obtain the physical properties of the melt phase. Next, we insert an approximately 35 km thick partially molten zone in the reference mantle. The top of the temperature sensitive partially molten zone is set at depths of 45 km for a potential temperature of 1500 K and 60 km for the potential temperature of 1300 K. We then calculate the reduction in shear wave speed when the melt is distributed in tubules in an undeformed state for melt volume fractions of 0.001 and 0.02, for dihedral angles of 5° and 25°, respectively. The detailed method of these calculations has been outlined in *Hier-Majumder et al.* [2014]. To test the role of deformation in the shear wave reduction, we also calculate the relative reduction in shear wave speed caused by melt films. Following the equations of *Walsh* [1969], we carry out these calculations for a melt volume fraction of 0.001 and film aspect ratios of 0.002 and 0.005.

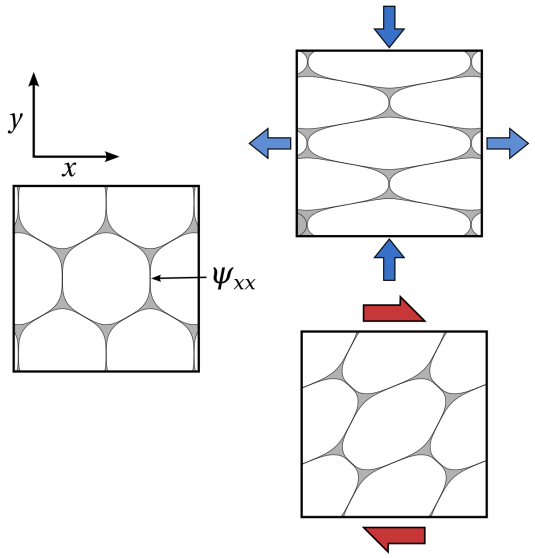

Figure 4.1: Microstructure of a small section from the deforming aggregate. On the left, the undeformed aggregate is shown. The ψ_{xx} component of the contiguity tensor is illustrated on a grain boundary of the undeformed aggregate. On the right, microstructures resulting from pure shear (top) and simple shear (bottom) deformation are shown.

4.3 Development of anisotropy

In this section, we present the results for the development of anisotropy in contiguity for both pure and simple shear deformation. We also present the results for seismic anisotropy for the pure shear case.

4.3.1 Development of anisotropic contiguity

During the course of deformation in the numerical experiments, as the grain shapes evolved, so did the anisotropy in the contiguity. The synthetic microstruc-

tures in Figure 4.1 depict the change in the shape of grains during pure and simple shear deformation. In the undeformed state, the melt is distributed evenly along tubules in three grain junctions. After pure shear deformation, the intergranular contact along the boundaries perpendicular to the x axis is substantially reduced, as the pockets on each end nearly touch each other, effectively transitioning into a film-like texture. An important consequence of this transformation is a significant reduction of the ψ_{xx} component of contiguity. In the simple shear experiment, we also see the development of such film-like structures along grain boundaries oriented in a sense antithetic to the applied, dextral shear.

As the partially molten aggregate is deformed in pure shear, the ψ_{xx} component of the contiguity tensor decreases while ψ_{yy} increases. The magnitude of contiguity, ψ, remains nearly constant. Data in Figure 4.2(a) demonstrate this trend. In the absence of deformation (zero strain), both diagonal components of contiguity are equal. The sum of these two components is the same as the total contiguity, ψ, which is the trace of the contiguity tensor. Each data point in the plot represents an average made over 1200 grains in the aggregate. As the aggregate is compressed parallel to the y axis, grain boundaries parallel to the direction of compression open up. Consequently, ψ_{xx}, the component of contiguity on the face perpendicular to the x axis, decreases. The opposite is observed for the faces normal to the y axis, resulting in an increase in the value of the ψ_{yy} component. This behavior of the aggregate is qualitatively similar to the change in microstructure observed in fractured, porous rocks [*Mavko et al.*, 2003]. The trace of the contiguity tensor, ψ, remains nearly constant during deformation. The shaded region in the plot

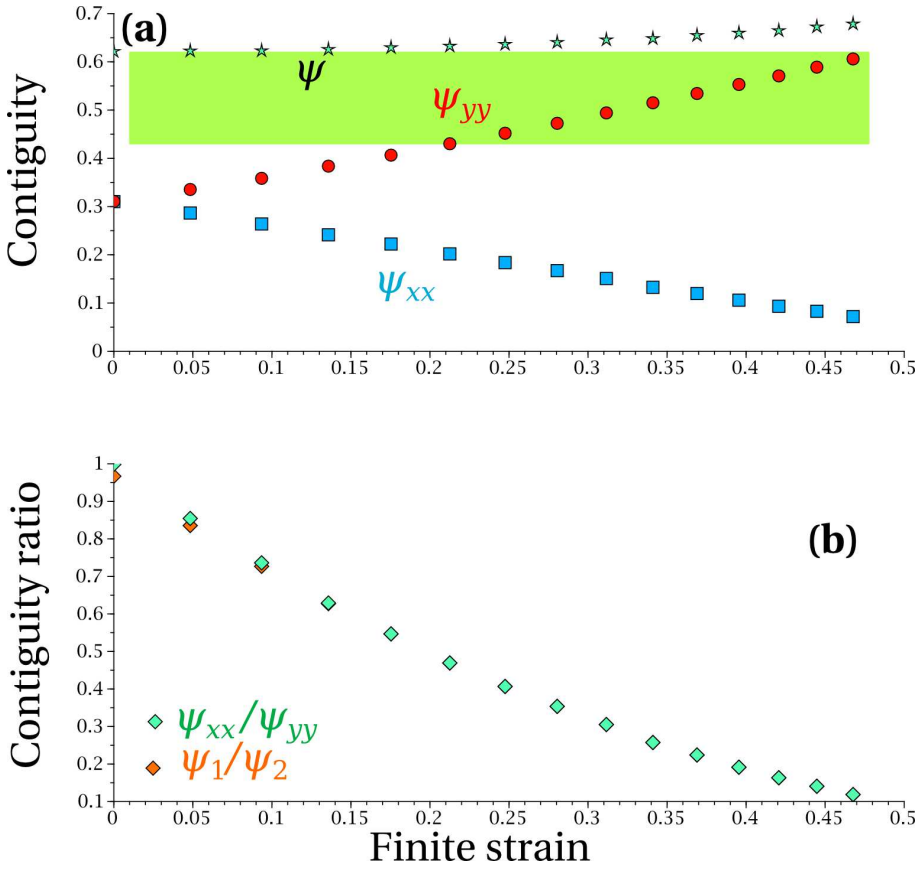

Figure 4.2: Development of anisotropic contiguity in pure shear. (a) Plot of the magnitude of contiguity, ψ, and the components ψ_{xx} and ψ_{yy} as a function of shortening. Each data point is averaged over 1200 grains in the numerical experiment. Width of the shaded region represents the range of contiguity reported by *Takei* [2005] for comparable melt volume fractions. (b) Ratio between the two principal components of contiguity (ψ_1/ψ_2) and the ratio between the ψ_{xx} and ψ_{yy} components. The data sets are practically indistinguishable and overlie each other.

depicts the range of values of contiguity measured by *Takei* [2005] in her samples deformed in pure shear. As the plot indicates, the trace of our contiguity matches the experimental measurements well.

During pure shear deformation, the anisotropy becomes stronger but no rotation of the contiguity tensor is observed. In Figure 4.2(b), the ratio between the xx and yy components of the contiguity tensor are plotted with the ratio between the two eigenvalues, ψ_1 and ψ_2. Both sets of data indicate a reduction in the ratio, signaling a strengthening of the anisotropy, while the data sets become indistinguishable as strain increases. As the principal axes of the applied strain rate remain stationary, this behavior of anisotropy development is physically reasonable. This observation qualitatively matches well with the experimental observation of *Takei* [2005] and *Daines and Kohlstedt* [1997].

During simple shear deformation, variations in the ψ_{xx} and ψ_{yy} components are comparatively small. In Figure 4.3(a), initially the ψ_{xx} component is slightly larger than the ψ_{yy} component. As deformation proceeds, however, the ψ_{xx} component is modestly reduced in magnitude. Similar to the pure shear case, the contiguity ψ remains nearly constant and consistent with the experimentally observed contiguity of *Takei* [2005]. The difference in behavior between the two types of deformation is explained by the data in Figure 4.3(b). Unlike the pure shear case, the ratio between the principal components differs significantly from the ratio between the x and y components. This difference arises from the rotational nature of the simple shear flow. As the grains deform, they undergo rotational motion, leading to a rotation of the contiguity tensor. As a result, the contiguity tensor is as anisotropic as

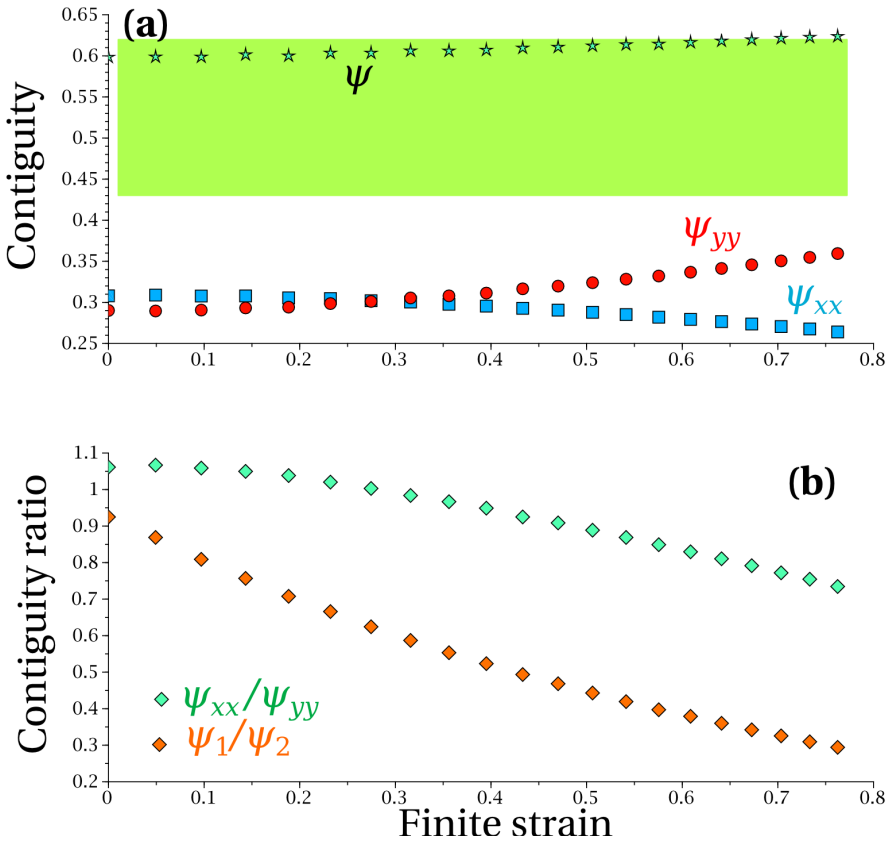

Figure 4.3: Development of anisotropic contiguity during simple shear. Each data point is averaged over 900 grains in the numerical experiment. (a) Plots of magnitude of contiguity ψ, and the components ψ_{xx} and ψ_{yy} as a function of shear strain. Width of the shaded region represents the range of contiguity reported by *Takei* [2005] for comparable melt volume fractions. (b) Ratio of the two principal components of contiguity (ψ_1/ψ_2) and the ratio between the ψ_{xx} and ψ_{yy} components.

the pure shear case, but the principal axes of anisotropy differ from the coordinate axes. It should be noted that the shear strains in our numerical experiments are relatively modest in comparison with experimental measurements [*King et al.*, 2011; *Hustoft and Kohlstedt*, 2006; *Hier-Majumder and Kohlstedt*, 2006]. Whereas the strain in the numerical pure shear experiments is substantially higher than experimental measurements such as *Daines and Kohlstedt* [1997], the fact that the ratio of the principal components of contiguity are comparable for both cases outlines that simple shear is more effective in generating anisotropic texture.

4.3.2 Development of seismic anisotropy

In the two-dimensional aggregate, melt is confined in pockets along the junction of three grains only. Due to the hexagonal symmetry of the grains, all components of contiguity are equal. Consequently, the speed of shear waves traveling through this aggregate is independent of either the direction of propagation or the directions of polarization. As deformation of the aggregate forces melt out of the triple grain junctions and wets a larger fraction of two grain contacts or grain boundaries, however, the speed of shear waves varies based on the direction of propagation and the direction of polarization. For the present two-dimensional case, we present the results for a shear wave traveling out of the plane in the z direction.

During pure shear, $\delta V_{Sx}/V_0$ decreases while $\delta V_{Sy}/V_0$ increases, as depicted in the plots in Figures 4.4(a) and (b). The rate of decrease of $\delta V_{Sx}/V_0$ slows down significantly, achieving a steady state around a finite strain of 0.4. At this strain,

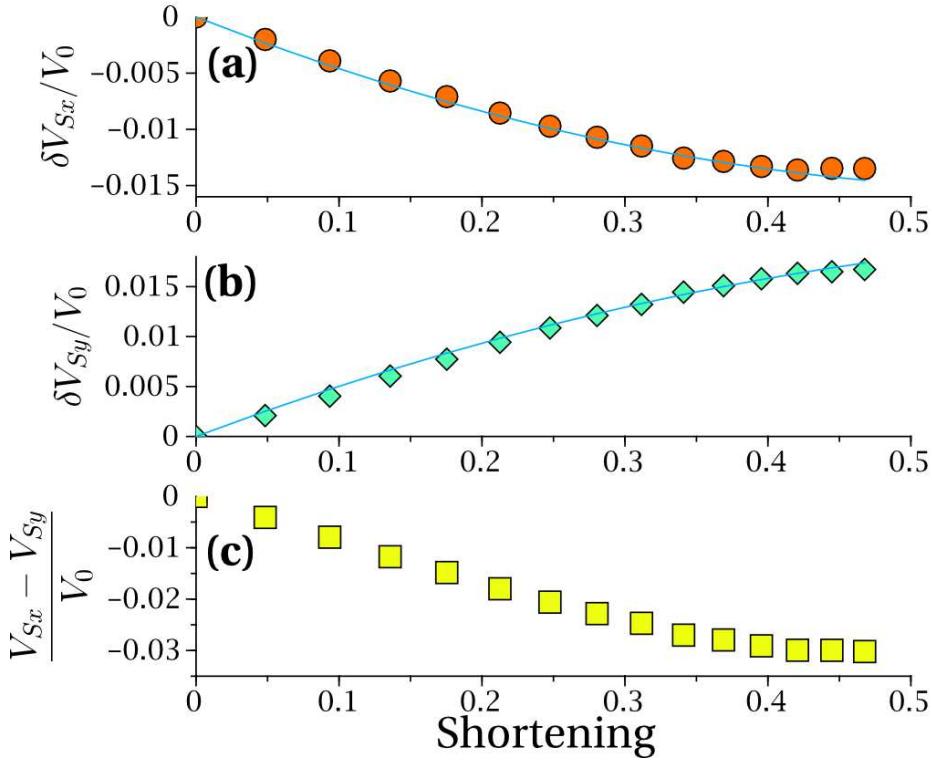

Figure 4.4: Development of shear wave anisotropy as a function of strain in pure shear. Variations in the wave speed of a wave traveling out of the plane of deformation with a polarization parallel to the (a) x axis, δV_{Sx}, and (b) y axis, δV_{Sy}, normalized by the wave speed in the isotropic aggregate, V_{eq}. The blue lines are polynomial fits to the data. Parameters for the fit and the fitting function are reported in Table 4.1. (c) Total seismic anisotropy, difference between the two polarizations of the shear wave, normalized by V_{eq}. The strain on the horizontal axis is shortening. Each data point represents an average of the 1200 grains.

Experiment	Quantity	p_1	p_2
Pure shear	δV_{Sy}	0.054	-0.036
	δV_{Sx}	-0.050	0.041
Simple shear	δV_{Sy}	0.002	0.008
	δV_{Sx}	-0.001	-0.006

Table 4.1: Parameters for fit to the reduction in shear wave speed $\delta V_{Si}(i = x, y)$ as a function of strain in pure and simple shear experiments. The equation for the fit is $\delta V_{Si} = p_1\epsilon + p_2\epsilon^2$, where ϵ is either the shortening or the shear strain.

the changes in the ratio $\delta V_{Sy}/V_0$ also slow down sharply. This trend is explained by the development of well-wetted vertical grain boundaries. Both changes reach approximately 1.5% by the steady state. In Figure 4.4(c), we plot the total anisotropy $(V_{sx} - V_{Sy})/V_0$ as a function of strain. Following the trend of each component, the total anisotropy also attains a nearly constant value of -0.03 at a shortening of 0.4. We overlay the data with a polynomial fit in Figures 4.4(a) and (b). The fitting function and coefficients are listed in Table 4.1.

During simple shear, however, reduction of the shear wave speeds with x polarization and increase of those with y polarization is less than the pure shear. Up to a shear strain of 0.8, δV_{Sx} is reduced by 0.4%, while δV_{Sy} increases by 0.6%, leading to a total anisotropy of approximately 1% as shown in Figures 4.5(a), (b), and (c). Since the principal components of the anisotropy tensor rotate away from the x and y plane, the shear wave anisotropy along the coordinate axes is weaker in this case.

Development of well-wetted grain boundaries is manifested in the seismic signature of the partially molten region. In the following section, we discuss the implications for this textural change on the seismic signature of the LAB.

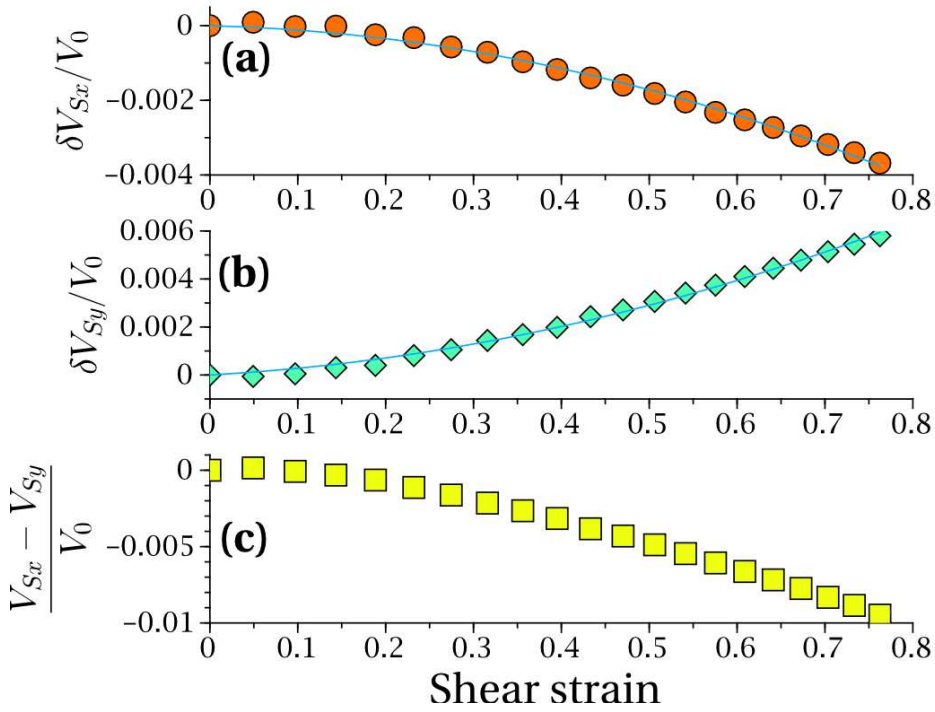

Figure 4.5: Development of shear wave anisotropy as a function of strain in simple shear. Variations in the wave speed of a wave traveling out of the plane of deformation with a polarization parallel to the (a) x axis, δV_{Sx}, and (b) y axis, δV_{Sy}, normalized by the wave speed in the isotropic aggregate, V_{eq}. The blue lines are polynomial fits to the data. Parameters for the fit and the fitting function are reported in Table 4.1. (c) Total seismic anisotropy, difference between the two polarizations of the shear wave, normalized by V_{eq}. The strain on the horizontal axis is the shear strain. Each data point represents an average of the 900 grains.

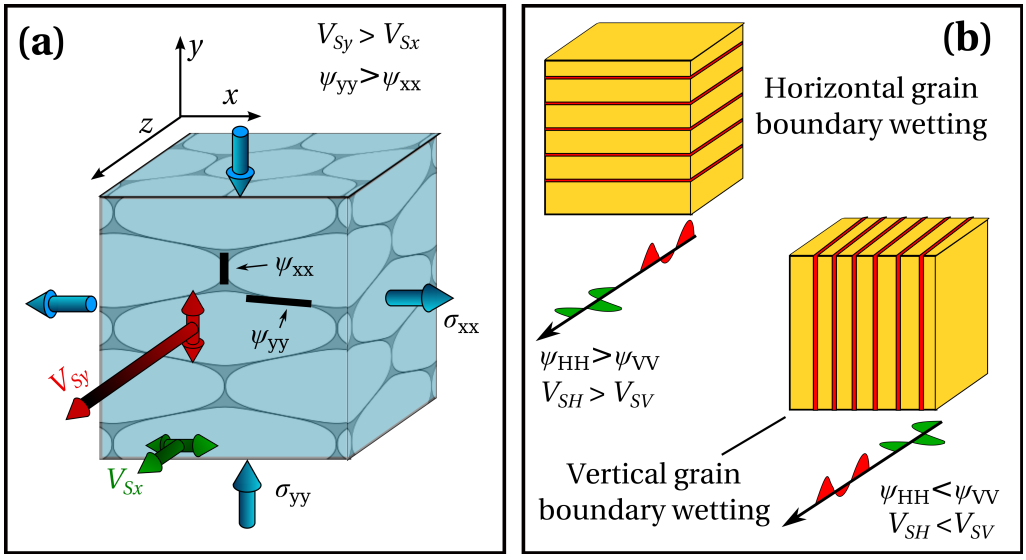

Figure 4.6: (a) A cartoon identifying the components of anisotropy and stress in an aggregate deformed by pure shear. Also shown are two waves, V_{Sx} and V_{Sy}, that travel out of the plane of deformation and are polarized in the x and y directions, respectively. The component of contiguity, ψ_{xx}, is reduced by predominant wetting of the grain boundaries perpendicular to the x direction. (b) Two illustrative cases resulting from preferential wetting of either horizontal or vertical grain boundaries. When the grain boundary melt films are horizontal, $V_{SH} > V_{SV}$, while the picture is reversed for vertical melt films.

4.4 Implications for melting in the LAB

Mapping the numerical experiments to nature As deformation forces melt to wet a greater fraction of grain boundaries, shear wave splitting will become more prominent. The cartoons in Figures 4.6(a) and (b) demonstrate the way seismic anisotropy from our numerical experiments can be mapped to the natural conditions. In our numerical experiments, contiguity is reduced along planes perpendicular to the x axis, rendering $\psi_{xx} < \psi_{yy}$. This situation is akin to the experimental observations of increase in aspect ratio of melt pockets in the direction of maximum compressive stress by *Daines and Kohlstedt* [1997]. Thus, we have $V_{Sy} > V_{Sx}$. If we consider two simple end member cases as outlined in Figure 4.6(b), predominantly

horizontal grain boundary wetting will lead to $V_{SH} > V_{SV}$. If the grain boundary wetting is vertical, however, the opposite effect will take place. Although we do not consider the role of LPO in the matrix, this picture is qualitatively similar to the predictions by *Holtzman and Kendall* [2010]. It is important to note that neither case demonstrates formation of large melt-rich bands. The shear wave anisotropy is brought about by grain scale redistribution of melt.

Comparison between observations and predictions We use two constraints arising from seismic observations. First, *Schmerr* [2012] observes nearly 5% reduction in the shear wave speed underneath the Pacific. The second observation involves 4% anisotropy of globally averaged shear wave speed beneath the LAB [*Nettles and Dziewoski*, 2008]. We test the influence of the melt volume fraction and geometry on these seismic signatures.

We consider two shear wave speed profiles for a reference mantle at temperatures of 1300 K and 1500 K, as depicted in Figures 4.7(a) and (b). The presence of a partially molten zone will be marked with a reduction in the shear wave speed. We consider a 35 km thick partially molten zone in this reference mantle. To account for the differences in depth of melting due to different potential temperatures, we place the top of the partially molten zone at a depth of 45 km for a potential temperature of 1500 K and 60 km for the potential temperature of 1300 K. The seismic profiles in Figure 4.7(a) compare the reduction of shear wave speed due to melt in tubules of dihedral angles varying between 5° and 25°. As the profiles indicate, reduction of the dihedral angle, for the same volume fraction of melt, causes a sharp reduction in the shear wave speed. Based on this profile, the observed 5% reduction in shear

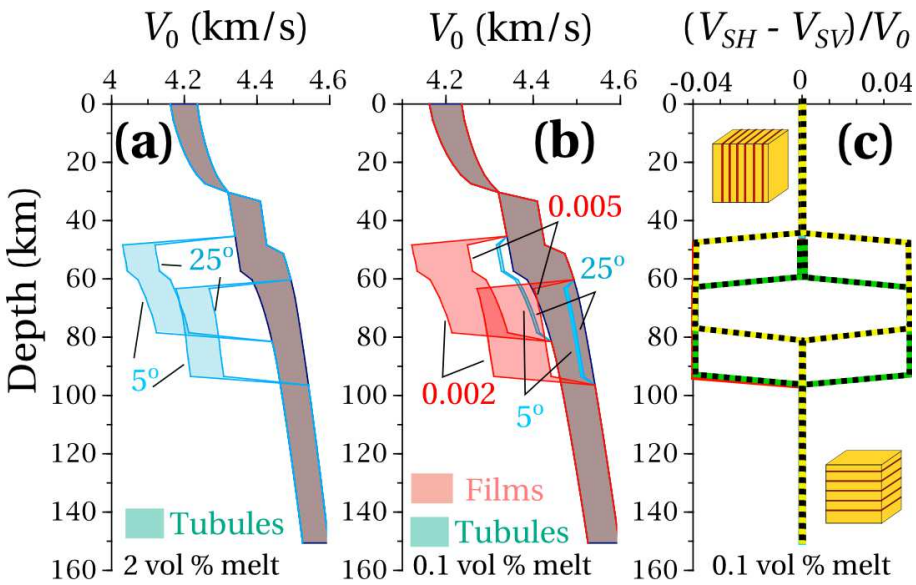

Figure 4.7: (a) Effect of melt geometry in shear wave speed reduction in the LAB. The gray shaded region represents shear wave speed profiles varying between potential temperatures of 1300 K and 1500 K, from *Xu et al.* [2008]. The temperature sensitive top and bottom of the melting zones are marked by broken horizontal lines. The blue shaded profiles represent shear wave speed reduction caused by 2 vol% melt in tubules for dihedral angles of 5° and 25°. (b) The thin blue curves correspond to reduction in the shear wave speed of the reference mantle if the 0.1 vol% melt is distributed in grain boundary tubules. The red regions represent reduction in the shear wave velocity if the same volume fraction of melt is distributed in thin grain boundary films. The width of the region represents the variations in the aspect ratio of the film. For the melt fraction of 0.1 vol%, the observed 5% reduction in shear wave velocity can be explained by melt films of aspect ratio 0.002, created by deformation. (c) Profiles of seismic anisotropy resulting from the distribution of melt in grain boundary films. If the films are oriented horizontally, the melting zone will depict an anisotropy of +4%. The sign of anisotropy will reverse if the melt is organized in vertical films.

wave speed can be explained by 2 vol% melt in tubules with a dihedral angle of 5°.

Although the shear wave speed reduction can be explained by 2 vol% melt in tubules, several other factors need to be taken into consideration. The isotropic distribution of melt in this case fails to explain the observed anisotropy in seismic and magnetotelluric signatures of the LAB. If partially molten, it is not possible to generate anisotropy by LPO of crystals by deformation while keeping the melt in uniformly distributed tubules. In addition, the permeability of 2 vol% melt may be sufficiently large to allow gravitational rise of the lighter melt rendering the source region depleted in melt. It is illustrative, therefore, to predict the seismic signature of a smaller volume fraction of melt distributed in films.

The profile in Figure 4.7(b) compares the reduction in shear wave speed caused by 0.1 vol% melt in films and tubules. At such small volume fractions, variations in the dihedral angle produce very small variations in the shear wave speed reductions, as indicated by the width of the blue profiles in this figure. We also plot the shear wave speed reduction by melt distributed along grain boundary films of aspect ratio varying between 0.002 and 0.005 using the relations from *Walsh* [1969]. When the melt is distributed in films of aspect ratio 0.002, the shear wave speed can be reduced to 5% despite the small melt volume fraction. In the profile in Figure 4.7(c), we plot the resultant seismic anisotropy for two different orientations of melt films. This anisotropy corresponds to the steady state anisotropy from melt films in our simple shear experiments.

Seismic anisotropy induced by small volume fraction of melt in horizontal films agrees well with the suggestion of *Kawakatsu et al.* [2009]. The relatively large

volume fraction of melt in tubules required to explain the seismic anisotropy poses two problems. First, such a large volume fraction of melt will likely be gravitationally unstable. The small volume fraction of melt in films is more likely to be retained at the source region as the low permeability and high surface tension at such small melt fractions will prevent efficient extraction of the melt [*Hier-Majumder*, 2011; *Hier-Majumder and Courtier*, 2011; *Hier-Majumder et al.*, 2006]. Second, the presence of small amounts of carbon will lead to a small degree of incipient melting in the LAB [*Sifré et al.*, 2014]. While this observation may explain the global radial anisotropy of shear wave, regional trends of $V_{SH} < V_{SV}$ can be likely attributed to the regional geodynamic setup [*Holtzman and Kendall*, 2010]. In addition, horizontal melt films help explain the observed nearly horizontal region of elevated electrical conductivity.

4.5 Conclusion

In this chapter, we demonstrate that the anisotropy in contiguity increases in a strongly nonlinear fashion with progressive pure and simple shear deformation. During pure shear deformation, the anisotropy in shear wave speed also increases in a strongly nonlinear fashion and achieves a steady state during our numerical experiments. Our results demonstrate that the observed shear wave speed reduction and seismic anisotropy in the LAB can be explained by as low as 0.1 vol% melt in horizontal films.

Chapter 5: Evolution of Anisotropy in Migrating Ultralow-Velocity Zones

5.1 Introduction

Earth's core-mantle boundary (CMB) marks a sharp transition in composition and physical properties between the rocky mantle and the molten, metallic outer core. The mantle side of this boundary is marked by a patchwork of physically distinct structures, termed Ultralow-Velocity Zones (ULVZs) [*Williams and Garnero*, 1996]. The ULVZs are typically 10% denser than the surrounding mantle [*Williams and Garnero*, 1996; *Rost and Revenaugh*, 2003; *Rost et al.*, 2005] and can span up to several hundreds of kilometers in lateral extent [*Cottaar and Romanowicz*, 2012; *Thorne et al.*, 2013]. Within the ULVZ, the speed of traveling shear waves decreases more dramatically (up to 30%) compared to compressional wave speed (up to 10%). As shear wave speed is more sensitive to the presence of partial melt, such a differential reduction likely implies the presence of 5-10 vol% melt within the ULVZ [*Hier-Majumder*, 2008; *Wimert and Hier-Majumder*, 2012; *Hier-Majumder*, 2014], although it has been argued that extremely iron-rich mineral phases can give rise to such seismic signatures [*Wicks et al.*, 2010; *Mao et al.*, 2006]. Based on a scaling

relation between the topography and viscosity of the ULVZ and the degree of melting, the viscosity of the ULVZ can be up to two orders of magnitude lower than the viscosity of the surrounding mantle [*Hier-Majumder and Revenaugh*, 2010].

The high density and low viscosity of the ULVZ plays an important role in the spatial correlation with structures in the lower mantle. In a series of analogue material experiments, *Jellinek and Manga* [2004] demonstrated that a thin, dense, and low viscosity ULVZ layers can act as anchors to mantle plumes, stabilizing them over geologic time scales. In addition, narrow, elongated ULVZs are detected along the edges of the Large Low Shear Velocity Provinces (LLSVPs), two nearly antipodal structures located beneath the Pacific and Africa, respectively [*McNamara et al.*, 2010]. Like mantle plumes, the LLSVPs are dynamic structures with active internal convection [*McNamara et al.*, 2010; *Bower et al.*, 2011; *Tan and Gurnis*, 2007]. The location, topography, and geometry of the ULVZ, thus, must be a result of the dynamic interaction between circulation within the ULVZ and the surrounding mantle structures.

The structure and location of the ULVZ embedded in a dynamic mantle is achieved by a balance between traction at the LLSVP-mantle interface and buoyancy forces. Low viscosity patches embedded within a circulating, higher viscosity fluid can be mixed and homogenized easily in geological time scales [*Manga*, 1996]. In the absence of an entraining, circulation around the dense patch, gravity current within the patch will spread it over the substrate into a thin, undetectable layer [*Koch and Koch*, 1995]. The fact that ULVZs are spatially correlated with regions of mantle flow and are structurally distinct from the surrounding mantle indicates

their shapes are controlled by a balance between gravitational drainage through the volume and traction at their interface caused by the entraining flow [*Hier-Majumder and Revenaugh*, 2010]. The flow within the ULVZ, excited by the entraining flow will also have important consequences for the internal structure of the ULVZ [*Hernlund and Jellinek*, 2010; *Hier-Majumder*, 2014].

If partially molten, deformation of the ULVZ matrix will redistribute the melt both in the large and small scale. In the large scale, compaction within the ULVZ aided by a top-driven cavity flow [*Hernlund and Jellinek*, 2010] or a pulsating vertical flow [*Hier-Majumder*, 2014], lead to the formation of a melt-rich layer near the top of the ULVZ. In the scale of individual mineral grains, deformation of the matrix will expel melt from tubules along triple grain junctions into films along grain boundaries, rendering the physical properties anisotropic. Anisotropic texture of the ULVZ matrix will likely leave its signature in the seismic wave speeds within the ULVZ. If detectable, the nature of such seismic anisotropy will be highly dependent on the nature of the flow within the ULVZ.

Previous studies have attempted to model the shapes of the ULVZs. *Garnero and McNamara* [2008]; *McNamara et al.* [2010]; *Bower et al.* [2011] modeled convection within the LLSVPs, but due to the nature of the model, they were not able to resolve the stress and tractions at the interfaces between the ULVZ and LLSVP. *Hier-Majumder and Revenaugh* [2010] studied the steady state shape of the ULVZ in isolation, which did not take into account the continuous deformation of the ULVZ. These models were not able to prescribe the stress jump at the LLSVP-mantle interface and track the exact shape of the ULVZ due to the imposed

flow.

In this work, we study the evolution of the shape of ULVZs with an imposed LLSVP flow. We combine the calculations for the flow field to model the likely presence of anisotropy within the ULVZ. In Section 5.2, we describe the governing equations that model the evolution of ULVZs within an LLSVP and the methods used to obtain numerical solutions. In Section 5.3, we present three simulations of ULVZ configuration of the numerical simulations. We present the results of the simulation in Section 5.4. Section 5.5 discusses their applicability to understanding the evolution of ULVZs within the LLSVP. We share closing thoughts and future research directions in Section 5.6.

5.2 Model

The evolution of ULVZ geometry within a convecting LLSVP is governed by a coupled viscous flow between ULVZ reservoirs and the LLSVP. In this section, we present the governing equations for the coupled flow, the setup for our numerical experiments, and the methods of post processing our numerical data.

Consider a collection of dense and low viscosity ULVZ patches embedded within a viscous LLSVP. The ULVZs and LLSVP are treated as incompressible fluids, such that the conservation of mass within each phase leads to

$$u_{i,i} = 0, \tag{5.1}$$

where u_i is the i-th component of the velocity vector and $(,i)$ represents the deriva-

tive with respect to x_i. Conservation of momentum within each ULVZ and the LLSVP requires, in the presence of gravitational acceleration,

$$\sigma_{ij,i} + \rho g_j = 0, \tag{5.2}$$

where σ_{ij} is the stress tensor of the fluid with density ρ. The vector g_j represents the force due to gravitational acceleration. The stress tensor is related to the fluid velocity through the constitutive relation,

$$\sigma_{ij} = -\delta_{ij} P + \mu \left(u_{i,j} + u_{j,i} \right), \tag{5.3}$$

where P is the dynamic pressure of the fluid, μ is the fluid viscosity, and δ_{ij} is the Kronecker delta. Governing Partial Differential Equations (PDEs) (5.1) and (5.2) within each ULVZ and the LLSVP need to be supplemented with boundary conditions to solve for the unknown velocity and dynamic pressure.

First, we impose the no-slip boundary condition at the LLSVP-ULVZ interfaces [*Pozrikidis*, 2001; *Leal*, 1992; *Kim and Karilla*, 2005], such that

$$u_i^{(-)}\Big|_{\Gamma_p} = u_i^{(+)}\Big|_{\Gamma_p}, \tag{5.4}$$

where $u_i^{(-)}$ is the velocity inside the p-th ULVZ and $u_i^{(+)}$ is the velocity in the LLSVP. The interface between the p-th ULVZ and the LLSVP is denoted Γ_p.

We fix the geometry of the LLSVP within the larger mantle and prescribe a driven-cavity flow-like condition on the tangential velocities along the LLSVP-

mantle boundary. The no-slip boundary condition at the LLSVP-mantle is

$$u_i \mid_{\Gamma_L} = \begin{cases} t_i & x_1 > 0 \\ -t_i & x_1 < 0 \end{cases}, \tag{5.5}$$

where t_i is the counterclockwise tangential vector along the LLSVP-mantle boundary, Γ_L. Boundary condition (5.5) maintains the shape of the LLSVP while driving the convection seen in larger thermo-chemical mantle simulations [*McNamara et al.*, 2010].

Next, we require the difference in traction across the LLSVP-ULVZ interfaces balance with buoyancy forces, leading to the stress jump condition

$$\Delta\sigma_{ij}\hat{n}_j + \Delta\rho x_j g_j \hat{n}_i = 0, \tag{5.6}$$

where $\Delta\sigma_{ij}$ is the stress drop across the surface of the ULVZ, $\Delta\rho$ is the density contrast, and $\hat{n}_i$ is the unit normal vector along the ULVZ-LLSVP interface, pointing into the LLSVP [*Leal*, 1992]. The density contrast is defined as $\Delta\rho = \rho_L - \rho_U$, where ρ_L is the density of the LLSVP and ρ_U is the density of the ULVZ. Since we prescribe the velocity at the LLSVP-mantle boundary, the tractions can be calculated from the imposed velocity.

Finally, we need an additional equation to describe the change in ULVZ shape due to deformation. Let $F^p(\boldsymbol{x}, t) = 0$ be the level set that defines Γ_p at time t. To ensure the volume of each grain remains constant during deformation of the grain,

we use the kinematic equation

$$F^p_{,t}(\boldsymbol{x},t) + u_i(\boldsymbol{x},t)F^p_{,i}(\boldsymbol{x},t) = 0. \tag{5.7}$$

The Boundary Element Method (BEM) is used to solve the PDEs (5.1) and (5.2) subject to the boundary condition for no-slip. The BEM uses Boundary Integral Equations (BIEs) first developed in *Ladyzhenskaya* [1963] and later described by a number of works [*Pozrikidis*, 2001; *Kim and Karilla*, 2005; *Happel and Brenner*, 1983; *Rallison and Acrivos*, 1978; *Manga and Stone*, 1993]. The BIE provides an integral formulation of the PDEs where all integration is limited to the boundaries, which provides significant advantages over domain methods for our problem. First, the discretization is limited to the boundary, reducing the dimension of the problem by one. Second, for evolving the ULVZs in an LLSVP, boundary methods only provide the solution along the boundary, which is exactly where the velocity is required for the kinematic equations. Furthermore, if desired, the BIE provides a method for computing the solution at arbitrary positions in the domain given once the solution at the boundary is obtained [*Pozrikidis*, 2001].

We follow the method laid out in *Manga and Stone* [1993] and *Pozrikidis* [2001] to describe the interaction between multiple deformable viscous drops. The dimensionless BIE for P ULVZ patches embedded in an LLSVP relates the velocity

$u_i(\boldsymbol{x})$ at point $\boldsymbol{x}_0$ on the surface of the q-th boundary by:

$$u_j(\boldsymbol{x}_0) = \frac{2}{1+\lambda_q}\left[-\sum_{p=1}^{P+1}\frac{\mathcal{R}_p}{4\pi}\int_{\Gamma_p}\Delta f_i(\boldsymbol{x})\mathcal{U}_{ij}(\boldsymbol{x},\boldsymbol{x}_0)\,\mathrm{d}\Gamma_p + \sum_{p=1}^{P+1}\frac{1-\lambda_p}{4\pi}\int_{\Gamma_p}^{\mathcal{PV}} u_i(\boldsymbol{x})\mathcal{T}_{ijk}(\boldsymbol{x},\boldsymbol{x}_0)\hat{n}_k(\boldsymbol{x})\,\mathrm{d}\Gamma_p\right], \tag{5.8}$$

where $\boldsymbol{x}_0$ is on the q-th fluid interface and often called the pole point. The point $\boldsymbol{x}$ on the p-th surface is called the field point [*Pozrikidis*, 2001]. To keep notation compact, we define $\Gamma_{P+1} \equiv \Gamma_L$ with the normal vector pointing from the LLSVP into the mantle. The two integrals over the interfaces are referred to as the single-layer and double-layer integrals, respectively. When $\boldsymbol{x}_0$ is on the boundary between a ULVZ and LLSVP, the dimensionless parameter, $\lambda_p = \mu_U/\mu_L$, is the viscosity ratio between the ULVZ and LLSVP, otherwise $\lambda_{P+1} = 0$.

Both integrands on the right hand side of equation (5.8) contain tensorial kernel functions. The tensors $\mathcal{U}_{ij}(\boldsymbol{x},\boldsymbol{x}_0)$ and $\mathcal{T}_{ijk}(\boldsymbol{x},\boldsymbol{x}_0)$ correspond to the velocity and stress components of the fundamental solution to the Stokes flow PDE [*Pozrikidis*, 2001; *Ladyzhenskaya*, 1963; *Kim and Karilla*, 2005]. For the present two-dimensional analysis, the second rank Stokeslet tensor is given by

$$\mathcal{U}_{ij}(\boldsymbol{x},\boldsymbol{x}_0) = -\delta_{ij}\ln r + \frac{\hat{x}_i\hat{x}_j}{r^2}, \tag{5.9}$$

where $\hat{\boldsymbol{x}} = \boldsymbol{x} - \boldsymbol{x}_0$ and $r = |\hat{\boldsymbol{x}}|$. The third rank tensor $\mathcal{T}_{ijk}(\boldsymbol{x},\boldsymbol{x}_0)$ is known as the Stresslet and is given by

$$\mathcal{T}_{ijk}(\boldsymbol{x},\boldsymbol{x}_0) = -4\frac{\hat{x}_i\hat{x}_j\hat{x}_k}{r^4}. \tag{5.10}$$

The interfacial stress jump $\Delta f_i(\boldsymbol{x})$ in the single-layer integral arises from the boundary condition balancing the stress drop across the interface with forces due to differences in fluid densities. Using (5.2), the interfacial stress jump is

$$\Delta f_i(\boldsymbol{x}) = \Delta\rho x_j \hat{g}_j \hat{n}_i. \tag{5.11}$$

The dimensionless compositional Rayleigh number, $\mathcal{R}_p$, represents the ratio between buoyancy and viscous forces at the LLSVP-ULVZ interface. The compositional Rayleigh number can be expressed in terms of the density difference $\Delta\rho_p$, gravitational acceleration g, characteristic length x_c, characteristic velocity u_c, and viscosity μ_L as

$$\mathcal{R}_p = \frac{\Delta\rho_p g x_c^2}{u_c \mu_L}. \tag{5.12}$$

We set $\mathcal{R}_{P+1} = 0$, eliminating the generation of forces along the LLSVP-mantle boundary.

The viscosity ratios and compositional Rayleigh numbers are the parameters that control the evolution of ULVZ shapes for the imposed velocity at the LLSVP-mantle boundary. At each time step, we solve the BIE (5.8) numerically to obtain the velocities at the boundary nodes of each grain. Next, we update the shape of each grain using equation (5.7). The geometric parameters from the new ULVZ shape are then used to solve the BIE for the next time step.

To visualize the coupled flow in the ULVZ interior and the LLSVP, we need

to construct streamlines from the velocity vectors. Once the velocities along the boundaries are known, the velocity at a point $\boldsymbol{x}_0$ located in the LLSVP is computed by

$$\begin{aligned} u_j(\boldsymbol{x}_0) = &- \sum_{p=1}^{P+1} \frac{\mathcal{R}_p}{4\pi} \int_{\Gamma_p} \Delta f_i(\boldsymbol{x}) \mathcal{U}_{ij}(\boldsymbol{x}, \boldsymbol{x}_0) \, \mathrm{d}\Gamma_p \\ &+ \sum_{p=1}^{P+1} \frac{1-\lambda_p}{4\pi} \int_{\Gamma_p} u_i(\boldsymbol{x}) \mathcal{T}_{ijk}(\boldsymbol{x}, \boldsymbol{x}_0) \hat{n}_k(\boldsymbol{x}) \, \mathrm{d}\Gamma_p. \end{aligned} \tag{5.13}$$

Notice that in contrast to the BIE (5.8), the velocity $u_i(\boldsymbol{x})$ and interfacial stress jump $\Delta f_i(\boldsymbol{x})$ in the integrands over the boundaries are now known. Thus, by choosing the location $\boldsymbol{x}_0$ at various points within the LLSVP and repeating the calculation in equation (5.13), we can generate the representation of the flow field within the LLSVP.

Similarly, the velocity at a point $\boldsymbol{x}_0$ within the q-th ULVZ is given by,

$$\begin{aligned} u_j(\boldsymbol{x}_0) = &- \sum_{p=1}^{P+1} \frac{\mathcal{R}_p}{4\pi\lambda_q} \int_{\Gamma_p} \Delta f_i(\boldsymbol{x}) \mathcal{U}_{ij}(\boldsymbol{x}, \boldsymbol{x}_0) \, \mathrm{d}\Gamma_p \\ &+ \sum_{p=1}^{P+1} \frac{1-\lambda_p}{4\pi\lambda_q} \int_{\Gamma_p} u_i(\boldsymbol{x}) \mathcal{T}_{ijk}(\boldsymbol{x}, \boldsymbol{x}_0) \hat{n}_k(\boldsymbol{x}) \, \mathrm{d}\Gamma_p. \end{aligned} \tag{5.14}$$

Since all quantities on the right hand side of equation (5.14) are known, we can calculate the velocity within each ULVZ by repeating the calculation for different locations $\boldsymbol{x}_0$ in the interior of the ULVZ. We continue the process for other ULVZs to compute the velocity field for a representative section of the problem domain. We visualize the velocity streamlines and derive strain tensors using the software

Paraview.

The method of collocation is used to discretize the BIE in (5.8). For the p-th interface, n_p pole nodes are placed on the boundary Γ_p. We adaptively space the pole points according to $\delta \propto \kappa^{\frac{2}{3}}$ where δ is the space between pole points and κ is the interface curvature [*Dritschel*, 1989]. The segments between two poles on the boundary is referred to as a boundary element. We approximate the position within each boundary element by cubic spline interpolation [*Press et al.*, 1992]. The stress jump $\Delta f_i(\boldsymbol{x})$ and velocity $u_i(\boldsymbol{x})$ along the boundary are interpolated piecewise linearly over each boundary element.

The resulting linear system is rewritten in matrix notation as

$$\left(\frac{1+\lambda}{2}\mathbf{I} - \frac{1-\lambda}{4\pi}\mathbf{T}\right)\boldsymbol{u} = -\frac{\mathcal{R}}{4\pi}\mathbf{U}\Delta\boldsymbol{f}, \tag{5.15}$$

where $\mathbf{I}$ is the identity matrix, and $\mathbf{U}$ and $\mathbf{T}$ are the matrices generated from the kernels of the single- and double-layer integrals, respectively. The vectors $\boldsymbol{u}$ and $\boldsymbol{\Delta f}$ are the velocities and interfacial stress jumps along the boundary, respectively. Velocities on the LLSVP-ULVZ boundary are unknown, as are the tractions along the LLSVP-mantle boundary. The linear system is rearranged to solve for the unknowns.

The system of linear algebraic equations arising from discretization of (5.8) is dense and generally asymmetric, requiring direct matrix inversion to solve. Direct methods require $\mathcal{O}(N^3)$ time and $\mathcal{O}(N^2)$ storage, where N is the number of degrees of freedom. The Fast Multipole Method (FMM) uses series expansions to

approximate the dense matrix-vector multiplications [*Appel*, 1985; *Barnes and Hut*, 1986; *Ambrosiano et al.*, 1988; *Carrier et al.*, 1988; *Guiggiani and Gigante*, 1990; *Board and Schulten*, 2000]. The series expansions separate the pole point from the integrals over the field points, removing the requirement of a unique evaluation for every combination of pole point and boundary element. The end result is an approximate matrix-vector multiplication that takes $\mathcal{O}(N)$ time and space compared to $\mathcal{O}(N^2)$ time and space required by direct BEM. The accelerated multiplication, in conjunction with iterative methods such as the GMRES [*Saad*, 2003], solves the linear system of equations in (5.15) in $\mathcal{O}(N)$ time.

5.3 Simulations

The geometry of the simulation is divided into two sets of interfaces: the LLSVP-mantle interface and LLSVP-ULVZ interfaces. For each simulation, we fix the LLSVP-mantle boundary as a trapezoid with rounded corners. The width, height, interior angle, and radius of curvature for the corners are specified to create the LLSVP geometry similar to structures observed in whole-mantle models. The LLSVP is 1,000 km across and 100 km high. The lower acute corner of the trapezoid has an angle of $\tan^{-1}(1/3)$. Both the corners are rounded with a 10 km radius of curvature. The density of the LLSVP is $\rho_L = 3500$ kg/m^3, while the density of the 10% denser ULVZ, ρ_U, is 3850 kg/m^3. The viscosity of the LLSVP is $\mu_L = 5 \times 10^{20}$ Pa s, and the viscosity of the ULVZ is two orders of magnitude less at $\mu_L = 5 \times 10^{18}$ Pa s. Acceleration due to gravity is $g = 9.8$ m/s^2. The imposed velocity along the

LLSVP-mantle prescribed in (5.5) is given a magnitude of 1 cm/yr.

We simulate three stages of ULVZ evolution within the LLSVP. Each simulation begins with ULVZs configured in a unique initial geometry. The first stage simulates the evolution of ULVZ material distributed in the center of the LLSVP. The second simulation begins with the ULVZ material distributed along the CMB. The third and final simulation demonstrates the steady state behavior of the ULVZ material in the corner of the LLSVP. We model the entire LLSVP for each stage but, since the results are symmetric, we only present the left half of the domain. Besides the three presented simulations, other geometry configurations we simulated others varying the size, position, and number of ULVZs within the LLSVP. The selected results are emblematic of the other simulations, displaying a representative collection of the observed phenomena.

We set the characteristic length $x_c = 25$ km and the characteristic velocity $u_c = 1$ cm/yr, resulting in a time scale of 2.5 Ma. Taken together with the physical parameters for the density, gravitational acceleration, and viscosity of the LLSVP, the dimensionless compositional Rayleigh number at the LLSVP-ULVZ boundary is $\mathcal{R}_p = -13.5$, where the negative sign indicates that the ULVZ is more dense than the surrounding LLSVP. A summary of the parameters used in the simulations is in Table 5.1.

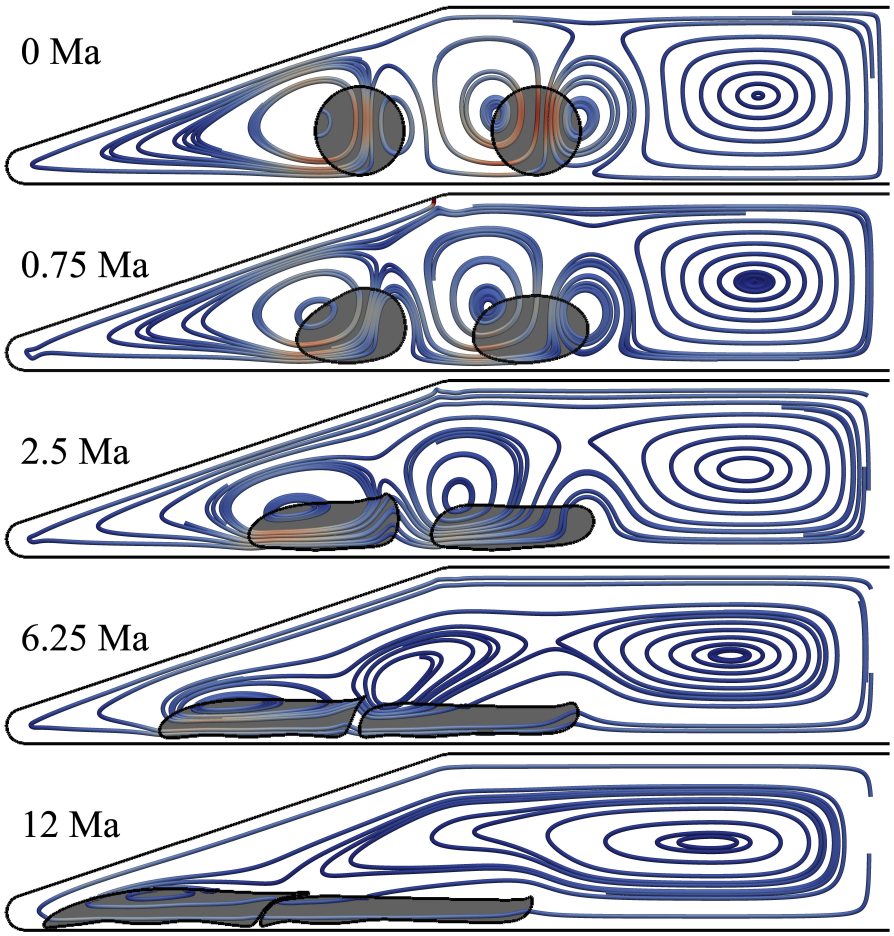

Figure 5.1: Evolution of circular ULVZ reservoirs placed in the LLSVP. The five snapshots show the evolution of the system between 0 and 12 Ma. The streamlines are colored by the magnitude of the velocity with light blue corresponding to 1 cm/yr and dark red to 3 cm/yr. The ULVZ patches are separated from the LLSVP by a black outline and shaded in gray.

Paramater	Symbol	Value
Characteristic length	x_c	25 km
Characteristic velocity	u_c	1 cm/yr
Gravitational acceleration	g	9.8 m/s^2
Viscosity of LLSVP	μ_L	5×10^{20} Pa s
Density of LLSVP	ρ_L	3500 kg/m^3
Density of ULVZ	ρ_U	3850 kg/m^3
Viscosity ratio	λ_p	10^{-2}
Compositional Rayleigh number	$\mathcal{R}_p$	-13.5

Table 5.1: Summary of parameters used in simulations. At the LLSVP-mantle interface, the viscosity ratio and compositional Rayleigh number are set to zero. The buoyancy neutral simulations set $\mathcal{R}_p = 0$ at the LLSVP-ULVZ interface. The boundary conditions at the LLSVP-mantle interface are given by (5.5).

5.4 Results

The first stage of numerical simulations, seen in Figure 5.1, demonstrate sinking, lateral spreading, and coalescence of two separated, initially circular ULVZ patches, each with a radius of 25 km. The ULVZs are centered 200 km and 300 km horizontally off center in the LLSVP and 30 km above the CMB, respectively. The dense ULVZs rapidly sink to the bottom of the LLSVP. Initially, the magnitude of velocity in and around the ULVZs is $\sim$3 cm/yr, as depicted by the color of the stream tubes. At 0.75 Ma, the initially circular ULVZs begin to flatten along the CMB. The clockwise circulation within the left half of the LLSVP sweeps the ULVZs to the left as they settle. By 2.5 Ma, the ULVZs are less than one half their original height and nearly double in width, as they continue flattening and spreading toward the corner of the LLSVP. The flattening reduces the buoyancy force of the ULVZs with velocity slowing to a maximum of 2 cm/yr.

The sunken ULVZ patches coalesce over the next 10 Ma. The velocities within the ULVZs and LLSVP continue to slow over the next 3.75 Ma with further flattening. At this point, the circulation within the LLSVP is the dominant force, pushing the ULVZs left toward the corner of the LLSVP. The ULVZs start approaching each other as they continue to be swept towards the left corner of the LLSVP. The coalescence between the two initially isolated ULVZ patches is complete by 12 Ma. The spreading edge of both ULVZs develop a "nose" structure, characteristic of well developed gravity currents [*Koch and Koch*, 1995]. The trailing edge of the left ULVZ wraps around and covers the leading edge of the ULVZ to the right. These stages of development leading to the coalescence of the ULVZs are very characteristic of coalescence of interacting, viscous drops [*Manga and Stone*, 1993]. The overall velocities within the system continue to drop to just above 1 cm/yr as the buoyancy force decreases and the system is driven almost completely by the LLSVP convection. At the end of this stage, a thin, horizontal ULVZ ponds at the bottom corner of the LLSVP. To avoid numerical singularities arising from sharp curvature, we start the next stage of simulation with a thin horizontal layer.

Flow near the corner of the LLSVP sweeps an initially flat ULVZ patch into a steady state pile near the corner over a relatively short period of time. The second stage of simulation, depicted in Figure 5.2, starts with a flat ULVZ that would result from the merger of two ULVZ patches from the previous simulation. In the simplified geometry, the ULVZs have coalesced into a single rounded rectangle approximately 111 km long and 9 km high (conserving the volume of the two original ULVZs). The stream tubes around the corner show the velocity field which will lift the ULVZ along

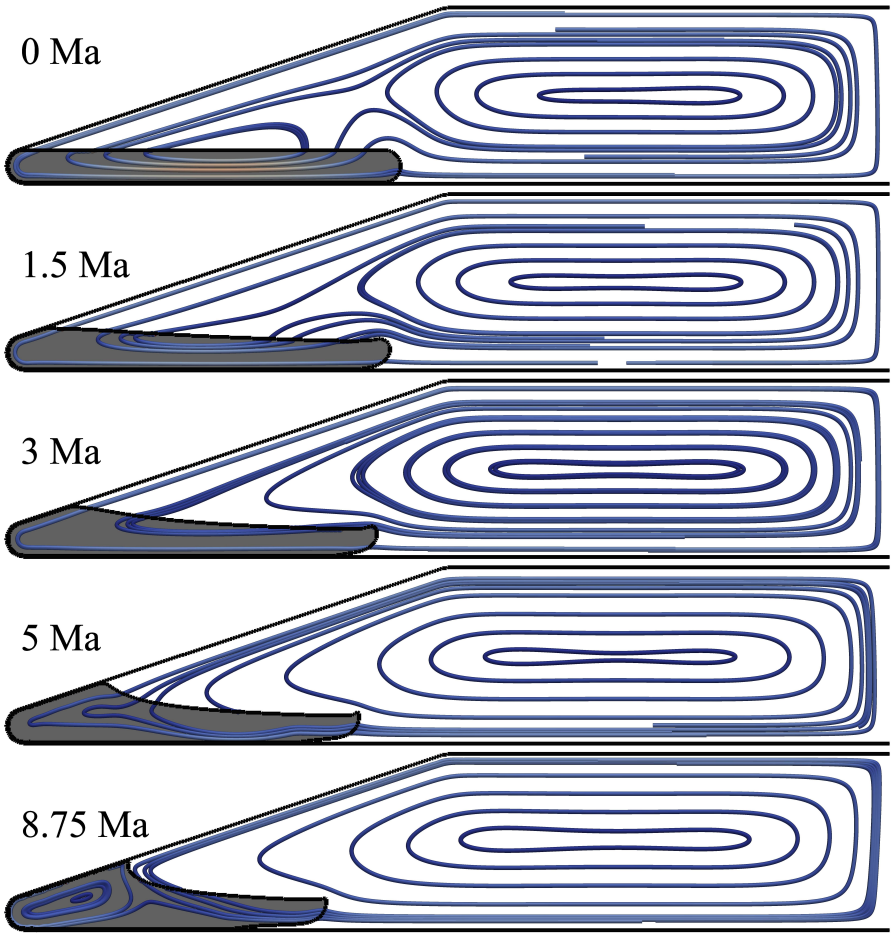

Figure 5.2: Evolution of rectangular ULVZ reservoirs with rounded corners placed in corners of the LLSVP. The five snapshots show the evolution of the system between 0 and 8.75 Ma. The streamlines are colored by the magnitude of the velocity with light blue corresponding to 1 cm/yr and dark red to 2 cm/yr. The ULVZ patches are separated from the LLSVP by a black outline and shaded in gray.

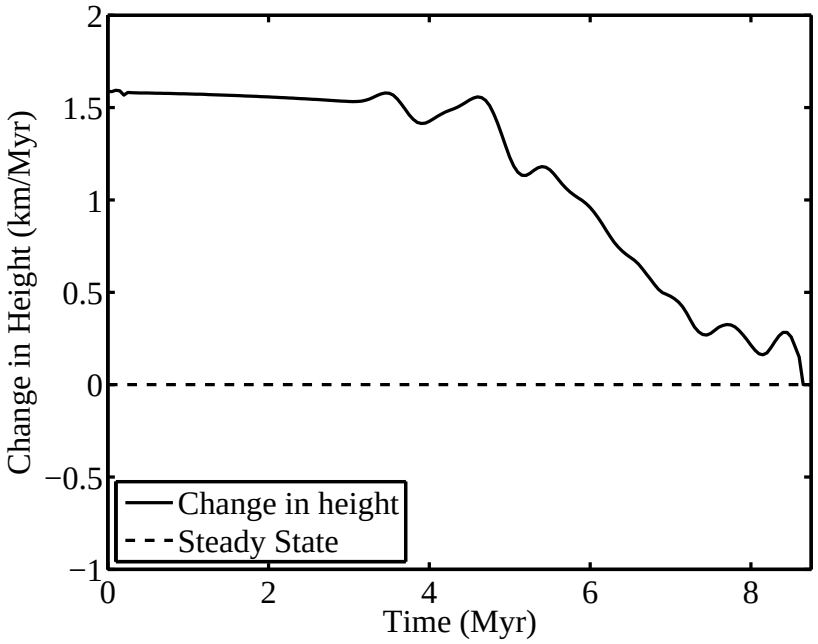

Figure 5.3: Change in height of the ULVZ reservoir as it climbs the wall of the LLSVP in Figure 5.2 is plotted by the solid line. The dashed line represents no change in height, i.e., steady state. The derivative is passed through a triangle smoothing filter to reduce noise in the measurement.

the wall of the LLSVP. The lifting is driven by the LLSVP clockwise convection of 1 cm/yr, which is impeded by the gravitational force from the dense ULVZ. At 1.5 Ma, the corner edge of the ULVZ becomes thicker than the central edge, showing initial signs of the lift. The continuous, wall-parallel streamlines indicate the circulation within the ULVZ is still very similar to the circulation within the LLSVP and lifting will continue. On the right edge of the ULVZ, the streamlines from the LLSVP bend around the end of the ULVZ.

In the next 7.25 Ma, an equilibrium is established between the entraining flow and the gravitational pull. The snapshots from 3 Ma and 5 Ma show an increase in the height of the ULVZ near the corner. The streamlines on the right edge of the

ULVZ now continue into the ULVZ instead of bending around it. Consequently, this edge is pushed toward the left. This combination of the lifting flow at the corner and the pushing flow on the trailing edge changes the shape of the initially flat ULVZ into a pile. Finally, at 8.75 Ma we observe the sign of the establishment of a steady state flow within the ULVZ. At this stage, a closed circulation, indicated by concentric streamlines, is established at the ULVZ corner. The closed circulation implies that while the flow is still active within the ULVZ, the shape is approaching a steady state. The plot in Figure 5.3 shows the rate of change in height of the ULVZ. The trend of the curve indicates a slowdown in growth approaching 8.75 Ma. By the end of the simulation, the ULVZ has increased its height by over 210% to 19 km. At this stage, high curvature near the top of the trailing edge of the ULVZ induces numerical instability to the ULVZ shape upon further deformation. To test for the steady state structure, we transform the initial ULVZ geometry in the next set of simulations.

The final simulation tracks the evolution of a ULVZ elevated beyond its steady state height. The initial geometry resembles a triangular wedge of ULVZ material placed into the corner of the LLSVP. Figure 5.4 shows the evolution of the triangular ULVZ wedge over 5 Ma. In the beginning of the simulation, the velocity field indicates the height of the ULVZ is unstable. At the corner, concentric stream tubes depict the closed circulation that was observed in the steady state in Figure 5.2 at 8.75 Ma. The circulation on the LLSVP-ULVZ interface, however, is quite distinct, as stream tubes enter and leave the ULVZ at the top and the bottom, respectively. Notice the stream tubes are tightly bunched over a small fraction of

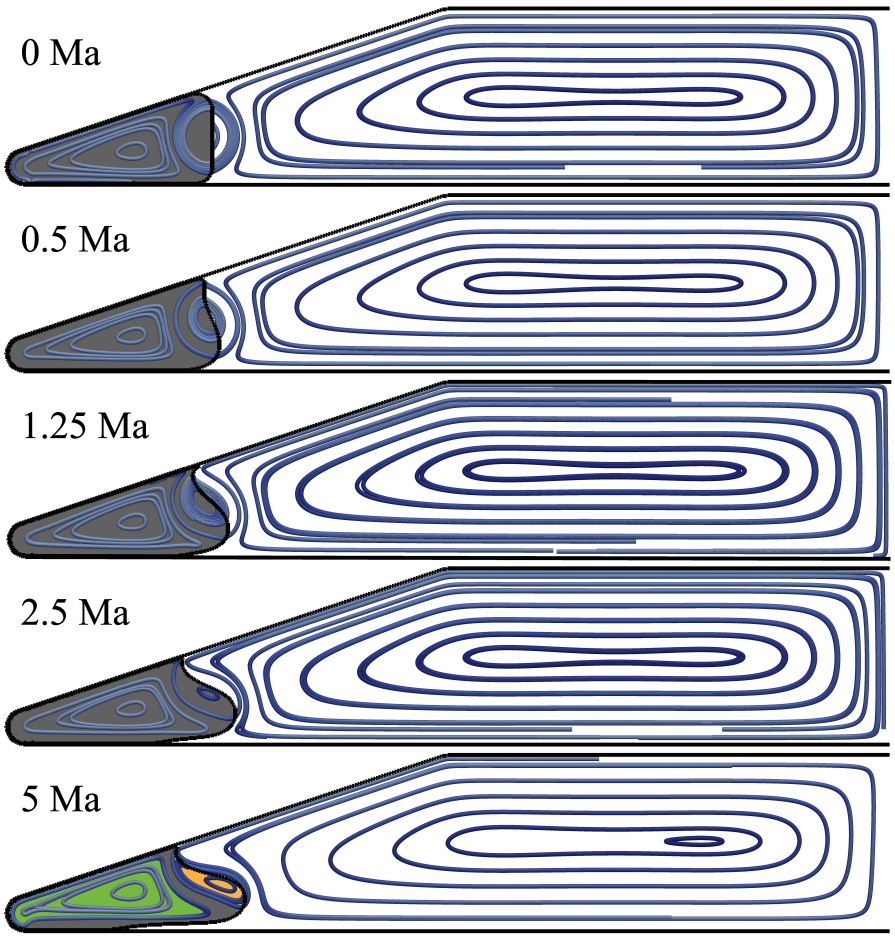

Figure 5.4: Evolution of ULVZ reservoirs wedged into the corners of the LLSVP. The five snapshots show the evolution of the system between 0 and 5 Ma. The streamlines are colored by the magnitude of the velocity with light blue corresponding to 1 cm/yr and dark red to 2 cm/yr. The ULVZ patches are separated from the LLSVP by the black outline and shaded in gray. The last snapshot highlights the streamlines, in green and orange, completely within the ULVZ indicating a steady state geometry has been achieved.

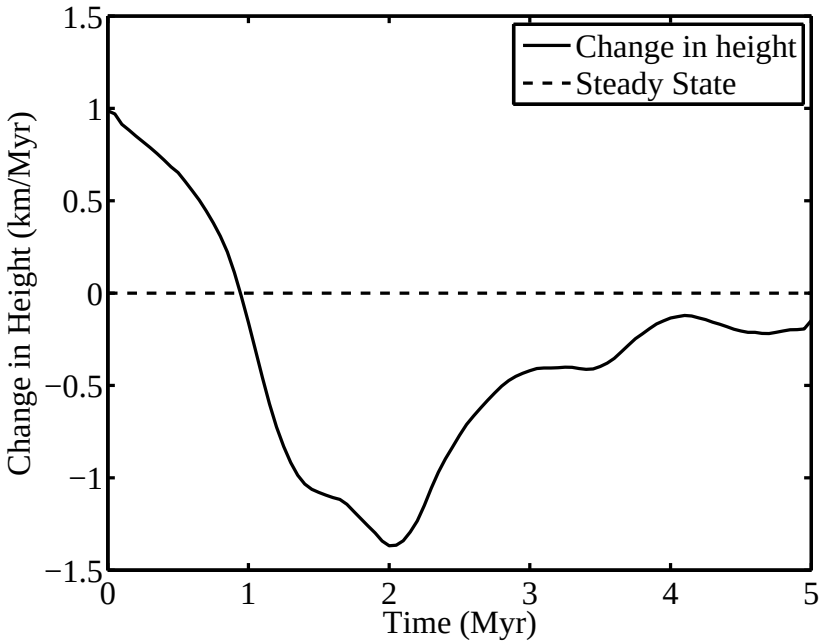

Figure 5.5: Change in height of the ULVZ reservoir as it falls down the wall of the LLSVP in Figure 5.4 is plotted in the solid line. The dashed line represents no change in height, i.e., steady state. The derivative is passed through a triangle smoothing filter to reduce noise in the measurement.

the area of the LLSVP-ULVZ interface, indicating the flow takes place in narrow regions. This counterclockwise flow, driven primarily by buoyancy forces, drains ULVZ material by a gravity current flowing upstream with respect to the entraining flow in the LLSVP. Over the next 2.5 Ma, the gravity current develops a nose-like structure near the bottom, where the outward normal velocity is the highest, indicated by the high angle subtended by the stream tubes to the interface. The opposing flow within the LLSVP lifts the bottom of the right edge of the ULVZ by a small amount, as the gravity current continues spreading upstream. By 5 Ma, two closed circulations are established within the ULVZ. Both of these circulations are highlighted in the figure. The stream tubes on the LLSVP-ULVZ interface are now mostly tangential to the interface. As a result, the shape of the ULVZ remains practically unchanged during subsequent iterations of the simulation. The steady state behavior is reinforced by the reduction in the change in height over time seen in Figure 5.5. The ULVZ has a height of 23.5 km and width of 67 km within the corner of the LLSVP.

In summary, the series of simulations indicate that near the center of the LLSVP, the ULVZ spreads out towards the edges as a gravity current. Over geologic time scales, the ULVZ becomes a thin, horizontal layer near the center of the LLSVP. The second and third stages of simulations indicate that in the steady state, the ULVZ occupies the corner of the LLSVP with a trailing lobe to the right. The balance between gravitational drainage and entrainment by the LLSVP is observed by the establishment of two circulation cells within the ULVZ, one excited by the entraining flow, the other excited by gravitational drainage.

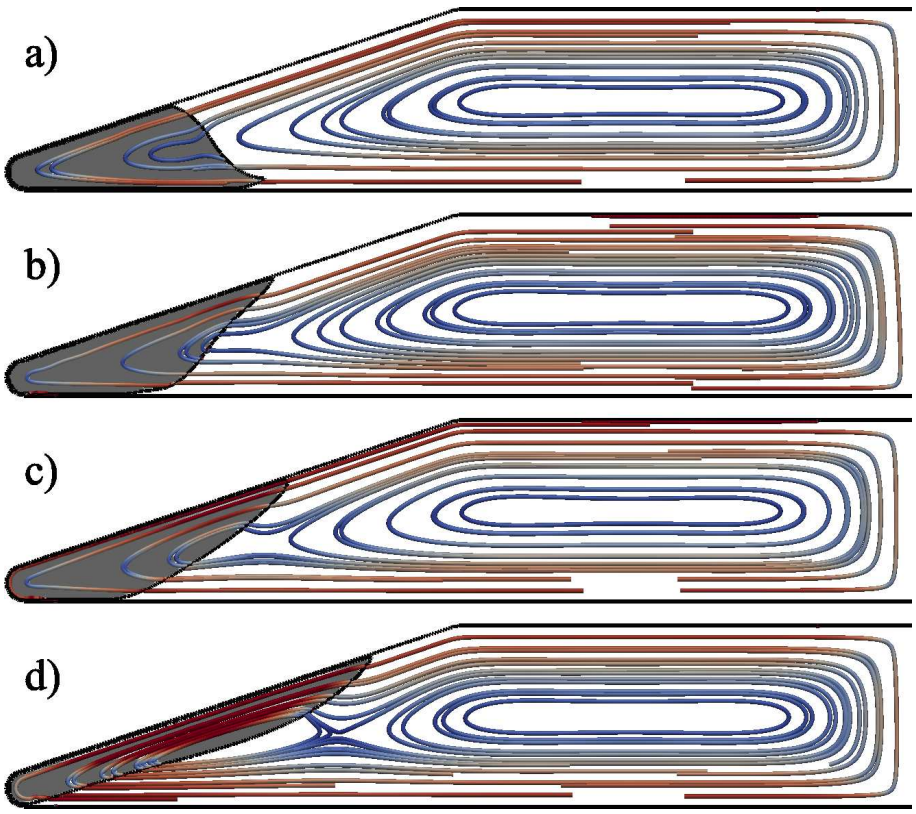

Figure 5.6: Evolution of buoyancy free, i.e., $\mathcal{R}_p = 0$, ULVZ reservoirs. The streamlines are colored by the magnitude of the velocity with light blue corresponding to 0 cm/yr and dark red to 1 cm/yr. a) and b) initially started in the same condition as Figure 5.2 at 0 Ma after 8.75 Ma and 15 Ma, respectively. c) and d) initially started in the same condition as Figure 5.4 at 0 Ma after 5 Ma and 10 Ma. The buoyancy neutral ULVZs are completely lifted up the wall of the LLSVP.

5.5 Discussion

5.5.1 The role of buoyancy

The series of snapshots presented in the previous section depict the evolution of the ULVZ shape, forced by the balance between entrainment and buoyancy. To further demonstrate the role of buoyancy, we carried out a separate set of simulations, spanning over 10 Ma. This series of simulations, depicted in Figure 5.6, starts

with a configuration similar to the steady state shape of a dense ULVZ. In this case, the trajectory of evolution of the ULVZ shape is remarkably different from the previous case. As the simulation continues, the ULVZ is easily lifted and stretched along the edge of the LLSVP. The flow pattern within the ULVZ, depicted by the stream tubes, differs from the previous case in a number of ways. First, a closed circulation loop is never established within the ULVZ. As the results in the previous section indicate, establishment of closed circulation is a crucial indicator of steady state. Second, the stream tubes entering and exiting the ULVZ at the bottom and the top of the LLSVP-ULVZ interface respectively, are spread evenly over a larger fraction of the interface. As a result, we do not observe the development of bulges and lobes, instead the deformation is distributed through the entire length of the ULVZ. This behavior is qualitatively similar to the behavior of neutrally buoyant, low viscosity blobs embedded in a circulating mantle as reported by *Manga* [1996]. While our calculations stop at 10 Ma, when continued over longer time scales, the ULVZ will be well mixed with the LLSVP matrix, undetectable by seismic waves. The seismic observations of dense ULVZs occurring along the corner of LLSVPs are therefore a clear indicator of the dynamic nature of the interaction between the ULVZs and the surrounding LLSVP.

5.5.2 Strain and anisotropy within the ULVZ

Figure 5.7(a) shows the strain at the end of the first simulation where the ULVZs started at the center of the LLSVP and then coalesced at the bottom of the

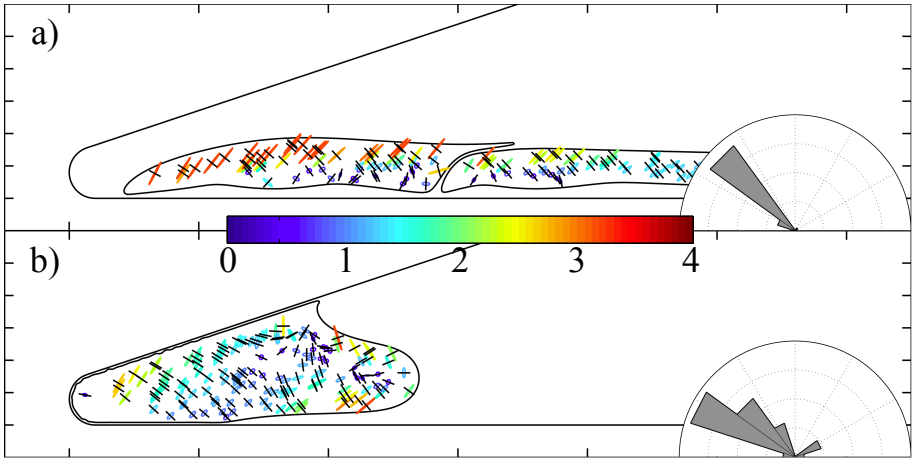

Figure 5.7: Strain tensor throughout the LLSVP for a) the end of the first simulation where the ULVZs were initially distributed in the center of the LLSVP and swept into the corner and b) the end of the third simulation where the ULVZ was initially a triangle wedge that settled into a steady state geometry. The strain is colored based on the magnitude of the principal dimension of deformation. The black lines represents the angle of melt channels forming within the ULVZs.

LLSVP (Figure 5.1). There is little strain throughout the LLSVP with the exception of the two small regions of mild strain at the top and bottom of the cavity's center. When the ULVZ is stretched along the CMB, the principal elongation is parallel to the $\theta = \pi/6$ axis, corresponding to nearly horizontal stretching of the ULVZ material. Buoyancy forces driving the ULVZ toward the CMB prevent the strain from stretching perfectly horizontal, i.e., along $\theta = 0$.

In Figure 5.7(b), we examine the steady state ULVZ geometry produced by initially placing a wedge-shaped ULVZ into the corner of the LLSVP (Figure 5.4). Again, there is little to no strain throughout the LLSVP. Here, the strain within the ULVZ is colored blue and dark purple, corresponding to elongation in the direction parallel to θ between $\pi/3$ and $2\pi/3$. Now, we see in the steady state that 1) the elongation is in the vertical direction, opposite the horizontal deformation in the

LLSVP, and 2) the strain rate is significantly higher within the less viscous ULVZ.

The results from Chapter 4 relate the finite strain of a partially molten aggregate to the changes in seismic velocities and can be qualitatively applied to our results here. As the strain increases within the partially molten ULVZ, we expect there to be a corresponding increase in the anisotropy in the contiguity tensor. Specifically, we expect vertical melt channels to open up when the ULVZ is in a steady state configuration at the corner of the LLSVP. The vertical melt channels will then lead to a drop in the velocity of the horizontally polarized shear waves compared to vertically polarized waves. The effect of melt channels, even with as low as 5 to 10 vol% melt, has been shown to generate relatively large amounts of anisotropy, which can lead to similar types of shear wave slowdowns that are observed in ULVZs located at the corner of LLSVPs.

5.6 Conclusion

We have used high resolution boundary to simulate the evolution of dense ULVZs within a convecting LLSVP. The results indicate a steady state geometry for elevated ULVZ patches located in the corners of the LLSVP, with the final geometry a result of a balance between weak convecting forces of the LLSVP and the gravitational potential of the ULVZ. Further analysis indicates ULVZ reservoirs in the process of being transported to the corners of the LLSVP exhibit nearly horizontal deformation throughout. Once in steady state, the strain in the ULVZ is primarily in the vertical direction, leading to the opening of vertical melt channels

within the partially molten ULVZ. The channels, even with low vol% of melt, are able to significantly affect shear wave velocities.

Chapter 6: Conclusion

The Boundary Element (BEM) addresses the issue of dynamic interaction between adjacent particles, leading to their deformation, by converting the governing Partial Differential Equations (PDEs) into a set of Boundary Integral Equations (BIEs) on the interface of each fluid. By coupling the BIEs with level set equations that govern the evolution of each fluid shape, we model the interaction between a number of fluids and their resulting deformation. While the BIE reduces the dimension of the problem by moving the calculation from the domain to the boundary, the calculations become computationally expensive as the number and resolution of the fluids grows, increasing the DOFs of the discretized set of algebraic equations. The computational expense of the BEM poses a challenge in carrying out simulations with a large number of fluids. The work in this thesis resolves this issue by implementing the Fast Multipole Boundary Element Method (FMBEM), which reduces the computational cost of solving the dense system of linear equations resulting from the discretization of the BIE by employing fast multipole expansion.

The results from our numerical experiments in Chapter 2 demonstrate that melt is expelled from grain edge tubules to grain boundary films during deformation. In pure shear configuration, the orientation of these films is parallel to the direction

of the principal compressive stress. In simple shear, these films are oriented in a sense antithetic to the sense of applied shear. The results from our microgeodynamic model also demonstrate that the magnitudes of anisotropic contiguity and differential shortening display a strongly nonlinear negative correlation. Such a correlation is revealed both in spatial distribution and temporal evolution of these quantities with progressive deformation. We also demonstrate that the flow between the grains and the interstitial melt phase are strongly coupled during deformation.

In Chapter 4, we demonstrated that the anisotropy in contiguity increases in a strongly nonlinear fashion with progressive pure and simple shear deformation. During pure shear deformation, the anisotropy in shear wave speed also increases in a strongly nonlinear fashion and achieves a steady state during our numerical experiments. Our results demonstrate that the observed shear wave speed reduction and seismic anisotropy in the Lithosphere-Asthenosphere Boundary (LAB) can be explained by as low as 0.1 vol% melt in horizontal films.

In Chapter 5, we have used high resolution boundary to simulate the evolution of dense UltraLow-Velocity Zones (ULVZs) within a convecting Large Low Shear Velocity Provinces (LLSVP). The results indicate a steady state geometry for elevated ULVZ patches located in the corners of the LLSVP, with the final geometry a result of a balance between weak convecting forces of the LLSVP and the gravitational potential of the ULVZ. Further analysis indicates ULVZ reservoirs in the process of being transported to the corners of the LLSVP exhibit nearly horizontal deformation throughout. Once in steady state, the strain in the ULVZ is primarily in the vertical direction, leading to the opening of vertical melt channels within

the partially molten ULVZ. The channels, even with low vol% of melt, are able to significantly affect shear wave velocities.

Chapter A: Resolving the Stokes' Paradox

In two dimensions, the Stokeslet is unbounded as the distance between the pole point and field point grows, resulting in unbounded velocities at infinity when modeling unbounded fluid domains as in Chapter 3. The fact that the velocity of two-dimensional free-space Stokeslet is unbounded in the presence of a point force is at the center of the Stokes' Paradox.

Often, the Stokeslet in two dimensions is modified to contain an image term that forces the velocity to converge to zero away from the point force. The image kernel is given by

$$\mathcal{U}_{ij}^{IM}(\boldsymbol{x}_0, \boldsymbol{x}) = \mathcal{U}_{ij}(\boldsymbol{x}_0, \boldsymbol{x}) - \mathcal{U}_{ij}(\boldsymbol{x}_0^{IM}, \boldsymbol{x}), \tag{A.1}$$

where $\mathcal{U}_{ij}(\boldsymbol{x}, \boldsymbol{x}_0)$ is the Stokeslet from (2.12) and $\boldsymbol{x}_0^{IM}$ is $\boldsymbol{x}_0$ reflected over a prescribed axis. The corresponding Stresslet is given by

$$\mathcal{T}_{ijk}^{IM}(\boldsymbol{x}_0, \boldsymbol{x}) = \mathcal{T}_{ijk}(\boldsymbol{x}_0, \boldsymbol{x}) - \mathcal{T}_{ijk}(\boldsymbol{x}_0^{IM}, \boldsymbol{x}), \tag{A.2}$$

where $\mathcal{T}_{ijk}(\boldsymbol{x}, \boldsymbol{x}_0)$ is the Stresslet from (2.12). While these new half-space kernels eliminate the Stokes' Paradox, they also impose an infinite wall with no-slip bound-

ary at the prescribed axis.

The infinite wall is unnatural for the numerical simulations presented in Chapter 3. An immediate option to reduce the wall's effect on the evolution of the simulation is to move the aggregate away from the wall. As the distance between the aggregate and the wall increases that the image Stokeslet evaluated at the fluid interfaces becomes bounded by

$$c_{ij} - \epsilon < \mathcal{U}_{ij}(\boldsymbol{x}_0^{IM}, \boldsymbol{x}) < c_{ij} + \epsilon, \tag{A.3}$$

where c_{ij} is a constant tensor and $\epsilon \propto \frac{1}{\delta}$, where δ is the distance between the aggregate and the wall. Thus if the aggregate is moved far enough from the wall, the value of the image Stokeslet at any point along the fluid interfaces is

$$\mathcal{U}_{ij}(\boldsymbol{x}_0^{IM}, \boldsymbol{x}) \approx c_{ij}, \tag{A.4}$$

up to numerical error. Thus, when far away from the wall, (A.1) becomes the standard Stokeslet (2.12). Since $\mathcal{T}_{ijk}(\boldsymbol{x}, \boldsymbol{x}_0)$ naturally tends to zero at infinity, (A.2) becomes the standard Stokeslet (2.14) as well.

The paradox will only arise when evaluating the velocity away from the aggregate, i.e., closer to infinity. If the velocity is only evaluated in the domain near the fluid interfaces, as in the cases presented in this work, the results when using the free-field or the modified half-space kernels will be numerically indistinguishable.

Chapter B: Tabular data from figures

This appendix presents the data used to generate Figures 4.2, 4.3, 4.4, and 4.5.

Finite Strain	ψ	ψ_{xx}	ψ_{yy}	ψ_{xx}/ψ_{yy}	ψ_1/ψ_2
0.000000	0.620927	0.310245	0.310682	0.998593	0.966951
0.048325	0.621979	0.286588	0.335391	0.854490	0.835497
0.093488	0.622407	0.263917	0.358490	0.736192	0.726803
0.135751	0.625135	0.241425	0.383710	0.629187	0.627301
0.175362	0.628907	0.222351	0.406556	0.546912	0.546661
0.212548	0.632036	0.201887	0.430149	0.469341	0.469149
0.247523	0.635761	0.183828	0.451933	0.406760	0.406605
0.280478	0.639700	0.167134	0.472566	0.353673	0.353541
0.311594	0.645012	0.150848	0.494163	0.305260	0.305139
0.341032	0.647684	0.132580	0.515105	0.257384	0.257259
0.368945	0.654157	0.119769	0.534388	0.224123	0.223997
0.395458	0.659043	0.105935	0.553108	0.191527	0.191387
0.420690	0.664084	0.093277	0.570806	0.163414	0.163254
0.444749	0.671871	0.082911	0.588960	0.140775	0.140591
0.467676	0.677987	0.071952	0.606035	0.118726	0.118505
0.489331	0.662567	0.038051	0.624516	0.060929	0.060605
0.510211	0.662255	0.021491	0.640765	0.033539	0.033192
0.529885	0.675585	0.019298	0.656287	0.029405	0.029009
0.548617	0.689176	0.017493	0.671683	0.026043	0.025595
0.566295	0.702221	0.015911	0.686310	0.023184	0.022671
0.582552	0.714737	0.014562	0.700175	0.020798	0.020206

Table B.1: Data from Figure 4.2

Finite Strain	ψ	ψ_{xx} ψ_{yy}	ψ_{xx}/ψ_{yy}	ψ_1/ψ_2	
0.000000	0.598137	0.307979	0.290158	1.061419	0.924972
0.049241	0.598444	0.308901	0.289543	1.066857	0.868868
0.097008	0.598397	0.307744	0.290653	1.058804	0.808945
0.143365	0.601125	0.307855	0.293270	1.049735	0.756770
0.188375	0.599726	0.305503	0.294222	1.038343	0.707682
0.232096	0.603205	0.304641	0.298564	1.020353	0.665948
0.274582	0.603168	0.302038	0.301130	1.003016	0.624302
0.315886	0.605833	0.300435	0.305398	0.983748	0.586899
0.356055	0.605694	0.297727	0.307967	0.966748	0.553239
0.395131	0.606762	0.295452	0.311310	0.949059	0.523327
0.433155	0.609322	0.292789	0.316532	0.924990	0.493535
0.470165	0.610367	0.290579	0.319788	0.908662	0.468299
0.506193	0.611911	0.287929	0.323983	0.888716	0.442941
0.541272	0.613396	0.285181	0.328216	0.868882	0.419349
0.575431	0.614058	0.281968	0.332090	0.849072	0.397059
0.608698	0.616051	0.279327	0.336725	0.829541	0.379119
0.641099	0.617915	0.276616	0.341299	0.810479	0.359970
0.672659	0.619421	0.273672	0.345749	0.791534	0.342132
0.703400	0.621092	0.270581	0.350510	0.771964	0.325530
0.733347	0.622397	0.267657	0.354740	0.754515	0.309380
0.762518	0.623453	0.264016	0.359438	0.734525	0.294141

Table B.2: Data from Figure 4.3

Shortening	$\delta V_{Sx}/V_0$	$\delta V_{Sy}/V_0$	$(\delta V_{Sx} - V_{Sy})/V_0$
0.000000	0.000000	0.000000	0.000000
0.048325	-0.002001	0.002090	-0.000997
0.093488	-0.003908	0.004033	-0.001935
0.135751	-0.005698	0.006046	-0.002859
0.175362	-0.007090	0.007734	-0.003604
0.212548	-0.008553	0.009430	-0.004368
0.247523	-0.009722	0.010863	-0.004995
0.280478	-0.010706	0.012110	-0.005530
0.311594	-0.011484	0.013220	-0.005978
0.341032	-0.012559	0.014451	-0.006531
0.368945	-0.012853	0.015095	-0.006746
0.395458	-0.013307	0.015789	-0.007014
0.420690	-0.013619	0.016328	-0.007209
0.444749	-0.013471	0.016490	-0.007198
0.467676	-0.013488	0.016718	-0.007245
0.489331	-0.017277	0.019920	-0.008958
0.510211	-0.018370	0.020999	-0.009482
0.529885	-0.016768	0.019918	-0.008805
0.548617	-0.015218	0.018765	-0.008129
0.566295	-0.013823	0.017641	-0.007503
0.582552	-0.012567	0.016554	-0.006926

Table B.3: Data from Figure 4.4

Shear strain	$\delta V_{Sx}/V_0$	$\delta V_{Sy}/V_0$	$(\delta V_{Sx} - V_{Sy})/V_0$
0.000000	0.000000	0.000000	0.000000
0.049241	0.000091	-0.000061	0.000037
0.097008	-0.000023	0.000049	-0.000018
0.143365	-0.000012	0.000303	-0.000077
0.188375	-0.000243	0.000399	-0.000158
0.232096	-0.000320	0.000807	-0.000276
0.274582	-0.000571	0.001054	-0.000398
0.315886	-0.000712	0.001438	-0.000526
0.356055	-0.000968	0.001682	-0.000649
0.395131	-0.001175	0.001983	-0.000773
0.433155	-0.001400	0.002431	-0.000937
0.470165	-0.001593	0.002712	-0.001053
0.506193	-0.001816	0.003064	-0.001193
0.541272	-0.002045	0.003413	-0.001333
0.575431	-0.002322	0.003744	-0.001482
0.608698	-0.002524	0.004102	-0.001617
0.641099	-0.002728	0.004448	-0.001751
0.672659	-0.002954	0.004786	-0.001887
0.703400	-0.003183	0.005137	-0.002028
0.733347	-0.003402	0.005448	-0.002156
0.762518	-0.003682	0.005802	-0.002310

Table B.4: Data from Figure 4.5

Bibliography

Ambrosiano, J., L. Greengard, and V. Rokhlin, The fast multipole method for gridless particle simulation, *Computer Physics Communications*, *48*(1), 117 – 125, doi:http://dx.doi.org/10.1016/0010-4655(88)90029-X, 1988.

Appel, A. W., An efficient program for many-body simulation, *SIAM Journal of Computing*, *6*, 85–103, 1985.

Barnes, J., and P. Hut, A hierarchical $\mathcal{O}(n \log n)$ force-calculation algorithm, *Nature*, *324*, 446–449, doi:10.1038/324446a0, 1986.

Board, J., and L. Schulten, The fast multipole algorithm, *Computing in Science & Engineering*, *2*(1), 76–79, 2000.

Bower, D. J., J. K. Wicks, M. Gurnis, and J. M. Jackson, A geodynamic and mineral physics model of a solid-state ultralow-velocity zone, *Earth and Planetary Science Letters*, *303*(3-4), 193 – 202, doi:DOI: 10.1016/j.epsl.2010.12.035, 2011.

Carrier, J., L. Greengard, and V. Rokhlin, A fast adaptive multipole algorithm for particle simulations, *SIAM Journal on Scientific and Statistical Computing*, *9*(4), 669–686, doi:10.1137/0909044, 1988.

Cottaar, S., and B. Romanowicz, An unsually large ULVZ at the base of the mantle near Hawaii, *Earth and Planetary Science Letters*, *355-356*, 213–222, doi: 10.1016/j.epsl.2012.09.005, 2012.

Daines, M. J., and D. L. Kohlstedt, Influence of deformation in melt topology in peridotites, *Journal of Geophysical Research*, *102*(B5), 10,257– 10,271, 1997.

Dritschel, D. G., Contour dynamics and contour surgery: Numerical algorithms for extended, high-resolution modelling of vortex dynamics in two-dimensional, inviscid, incompressible flows, *Computer Physics Reports*, *10*(3), 77 – 146, doi: http://dx.doi.org/10.1016/0167-7977(89)90004-X, 1989.

Drombosky, T. W., and S. Hier-Majumder, Development of anisotropic texture in deforming partially molten aggregates i: Theory and fast multipole boundary elements method, *Journal of Geophysical Research: Solid Earth*, 2014.

Evans, R. L., G. Hirth, K. Baba, D. Forsyth, A. Chave, and R. Mackie, Geophysical evidence from the melt area for compositional controls on oceanic plates, *Nature*, *437*, 249–252, doi:10.1038/nature04014, 2005.

Fischer, K. M., H. A. Ford, D. L. Abt, and C. A. Rychert, The lithosphere-asthenosphere boundary, *Annual Review of Earth and Planetary Sciences*, *38*(1), 551–575, doi:10.1146/annurev-earth-040809-152438, 2010.

Gao, X.-W., Numerical evaluation of singular boundary integrals- theory and fortran code, *Journal of Computational and Applied Mathematics*, *188*(B5), 44–64, 2006.

Garnero, E., and A. K. McNamara, Structure and dynamics of Earth's lower mantle, *Science*, *320*, 626–628, 2008.

German, R., *Liquid Phase Sintering*, Plenum Press, 1985.

Ghosh, S., E. Ohtani, K. Litasov, A. Suzuki, and T. Sakamaki, Stability of carbonated magmas at the base of the Earth's upper mantle, *Geophysical Research Letters*, *34*(22), doi:10.1029/2007GL031349, 2007.

Greengard, L., and W. Gropp, A parallel version of the fast multipole method, *Computers & Mathematics with Applications*, *20*(7), 63 – 71, doi: http://dx.doi.org/10.1016/0898-1221(90)90349-O, 1990.

Guiggiani, M., and A. Gigante, A general algorithm for multidimensional cauchy principal value integrals in the boundary element method, *ASME Transactions*, *57*, 906–915, 1990.

Happel, J., and H. Brenner, *Low Reynolds number hydrodynamics*, Kluwer, 1983.

Hernlund, J. W., and A. M. Jellinek, Dynamics and structure of a stirred partially molten ultralow-velocity zone, *Earth and Planetary Science Letters*, *296*(1-2), 1–8, doi:10.1016/j.epsl.2010.04.027, 2010.

Hier-Majumder, S., Influence of contiguity on seismic velocities of partially molten aggregates, *Journal of Geophysical Research-Solid Earth*, *113*(B12), B12,205, doi: 10.1029/2008JB005662, 2008.

Hier-Majumder, S., Development of anisotropic mobility during two-phase flow, *Geophysical Journal International*, *186*, 59–68, doi:10.1111/j.1365-246X.2011.05024.x, 2011.

Hier-Majumder, S., Melt redistribution by pulsed compaction within ultralow velocity zones, *Phys. Earth and Planet. Int.*, doi:10.1016/j.pepi.2014.01.004, 2014.

Hier-Majumder, S., and M. E. Abbott, Influence of dihedral angle on the seismic velocities in partially molten rocks, *Earth and Planetary Science Letters*, *299*(1-2), 23–32, doi:10.1016/j.epsl.2010.08.007, 2010.

Hier-Majumder, S., and A. Courtier, Seismic signature of small melt fraction atop the transition zone, *Earth and Planetary Science Letters*, *308*(3-4), 334–342, doi:doi:10.1016/j.epsl.2011.05.055, 2011.

Hier-Majumder, S., and T. W. Drombosky, Development of anisotropic texture in deforming partially molten aggregates ii: Implications for the lithosphere-asthenosphere boundary, *Journal of Geophysical Research: Solid Earth*, 2014.

Hier-Majumder, S., and D. Kohlstedt, Role of dynamic grain boundary wetting in fluid circulation beneath volcanic arcs, *Geophysical Research Letters*, *33*(8), L08,305, doi:10.1029/2006GL025716, 2006.

Hier-Majumder, S., and J. Revenaugh, Relationship between the viscosity and topography of the ultralow-velocity zone near the core-mantle boundary, *Earth and Planetary Science Letters*, *299*(3-4), 382–386, doi:10.1016/j.epsl.2010.09.018, 2010.

Hier-Majumder, S., E. B. Keel, and A. M. Courtier, The influence of temperature, bulk composition, and melting on the seismic signature of the low-velocity layer above the transition zone, *Journal of Geophysical Research: Solid Earth*, pp. n/a–n/a, doi:10.1002/2013JB010314, 2014.

Hier-Majumder, S., Y. Ricard, and D. Bercovici, Role of grain boundaries in magma migration and storage, *Earth and Planetary Science Letters*, *248*(3-4), 735–749, doi:10.1016/j.epsl.2006.06.015, 2006.

Holtzman, B. K., and J.-M. Kendall, Organized melt, seismic anisotropy, and plate boundary lubrication, *Geochemistry Geophysics Geosystems*, *11*(12), n/a–n/a, doi:10.1029/2010GC003296, 2010.

Holtzman, B. K., D. L. Kohlstedt, M. E. Zimmerman, F. Heidelbach, T. Hiraga, and J. Hustoft, Melt segregation and strain partitioning: Implications for seismic anisotropy and mantle flow, *Science*, *301*, 1227–1230, 2003.

Hustoft, J., and D. Kohlstedt, Metal silicate segregation in deforming dunitic rocks, *Geochemistry Geophysics Geosystems*, *7*(Q02001), 2006.

Jellinek, A., and M. Manga, Links between long-lived hotspots, mantle plumes D″, and plate tectonics, *Reviews of Geophysics*, *42*(RG3002), 2004.

Kang, S.-j. L., *Sintering: Densification, Grain Growth and Microstructure*, Elsevier, 2005.

Kawakatsu, H., P. Kumar, Y. Takei, M. Shinohara, T. Kanazawa, E. Araki, and K. Suyehiro, Seismic evidence for sharp lithosphere-asthenosphere boundaries of oceanic plates, *Science*, *324*(5926), 499–502, doi:10.1126/science.1169499, 2009.

Kim, S., and S. J. Karilla, *Microhydrodynamics: Principles and selected applications*, chap. 13, Dover, 2005.

King, D. S. H., S. Hier-Majumder, and D. L. Kohlstedt, An experimental study of the effects of surface tension in homogenizing perturbations in melt fraction, *Earth and Planetary Science Letters*, *307*(3-4), 735–749, doi:doi:10.1016/j.epsl.2011.05.009, 2011.

Koch, D. M., and D. L. Koch, Numerical and theoretical solutions for a drop spreading below a free fluid surface, *Journal of Fluid Mechanics*, *287*, 251–278, doi:10.1017/S0022112095000942, 1995.

Lachat, J., and J. Watson, Effective numerical treatment of boundary integral equations: A formulation for three-dimensional elastostatics, *International Journal for Numerical Methods in Engineering*, *10*, 991–1005, 1987.

Ladyzhenskaya, O., *The Mathematical Theory of Viscous Incompressible Flow*, chap. 3, Gordon and Breach, 1963.

Leal, G., *Laminar Flow and Convective Transport Processes*, Butterworth-Heinemann, 1992.

Lean, M., and A. Wexler, Accurate numerical integration of singular boundary element kernels over boundaries with curvature, *International Journal for Numerical Methods in Engineering*, *21*, 211–228, 1985.

Li, X., and C. Pozrikidis, Shear flow over a liquid drop adhering to a solid surface, *Journal of Fluid Mechanics*, *307*, 167–190, 1996.

Liu, Y., *Fast Multipole Boundary Element Method*, Cambridge University Press, 2009.

Liu, Y., and N. Nishimura, The fast multipole boundary element method for potential problems: A tutorial, *Engineering Analysis with Boundary Elements*, *30*(5), 371–381, doi:10.1016/j.enganabound.2005.11.006, 2006.

Manga, M., Dynamics of drops in branched tubes, *Journal of Fluid Mechanics*, *315*, 105–117, 1996.

Manga, M., and H. Stone, Buoyancy-driven interactions between two deformable viscous drops, *Journal of Fluid Mechanics*, *256*, 647–683, 1993.

Mao, W. L., H.-K. Mao, W. Sturhahn, J. Zhao, V. B. Prakapenka, Y. Meng, J. Shu, Y. Fei, and R. J. Hemley, Iron-rich post perovskite and the origin of the ultra low velocity zone, *Science*, *312*, 564–565, 2006.

Mavko, G., T. Mukerji, and J. Dvorkin, *Rock Physics Handbook*, Cambridge University Press, 2003.

McNamara, A. K., E. J. Garnero, and S. Rost, Tracking deep mantle reservoirs with ultra-low velocity zones, *Earth and Planetary Science Letters*, *299*(1-2), 1–9, doi:10.1016/j.epsl.2010.07.042, 2010.

Morton, G. M., A computer oriented geodetic data base; and a new technique in file sequencing, *Tech. rep.*, IBM, Ottawa, Canada, 1966.

Naif, S., K. Key, S. Constable, and R. L. Evans, Melt-rich channel observed at the lithosphere-asthenosphere boundary, *Nature*, *495*, 356–359, doi: 10.1038/nature11939, 2013.

Nettles, M., and A. M. Dziewoski, Radially anisotropic shear velocity structure of the upper mantle globally and beneath north america, *Journal of Geophysical Research: Solid Earth*, *113*(B2), B02,303, doi:10.1029/2006JB004819, 2008.

Pozrikidis, C., The deformation of a liquid drop moving normal to a plane wall, *Journal of Fluid Mechanics*, *215*, 331–363, 1990.

Pozrikidis, C., *Boundary integral and singularity methods for linearized viscous flow*, chap. 5, Cambridge University Press, 1991.

Pozrikidis, C., Interfacial dynamics for stokes flow, *Journal of Computational Physics*, *169*, 250–301, 2001.

Press, W. H., S. A. Teukolsky, W. T. Vetterling, and B. P. Flannery, *Numerical recipes in FORTRAN*, chap. 19.6, 2 ed., Cambridge University Press, 1992.

Rallison, J., and A. Acrivos, A numerical study of deformation and burst of a viscous drop in an extensional flow, *Journal of Fluid Mechanics*, *89*, 191–200, 1978.

Rost, S., and J. Revenaugh, Small scale ultralow-velocity zone structure imaged by *ScP*, *Journal of Geophysical Research*, *108*(B12056), 2003.

Rost, S., E. J. Garnero, Q. Williams, and M. M., Seismological constraints on a possible plume root at the core-mantle boundary, *Nature*, *435*, 666–669, 2005.

Rychert, C. A., P. M. Shearer, and K. M. Fischer, Scattered wave imaging of the lithosphereasthenosphere boundary, *Lithos*, *120*(12), 173 – 185, doi: http://dx.doi.org/10.1016/j.lithos.2009.12.006, 2010.

Saad, Y., *Iterative Methods for Sparse Linear Systems*, 2 ed., SIAM, 2003.

Schmerr, N., The gutenberg discontinuity: Melt at the lithosphere-asthenosphere boundary, *Science*, *335*(6075), 1480–1483, doi:10.1126/science.1215433, 2012.

Sifré, D., E. Gardés, L. Hashim, M. Massuyeau, S. Hier-Majumder, and F. Gaillard, Incipient $CO_2 - H_2O$ rich melts in the lithosphere-asthenosphere boundary, *Nature*, 2014.

Sutton, A. P., and R. W. Balluffi, *Interfaces in Crystalline Materials*, Oxford University Press, 1995.

Takei, Y., Constitutive mechanical relations of solid-liquid composites in terms of grain boundary contiguity, *Journal of Geophysical Research*, *103*, 18,183–18,203, 1998.

Takei, Y., Effect of pore geometry on v_p/v_s: From equilibrium geometry to crack, *Journal of Geophysical Research*, *107*, 2043, 2002.

Takei, Y., Deformation induced grain boundary wetting and its effect on acoustic and rheological properties of partially molten rock analogue, *Journal of Geophysical Research*, *110*, B12,203, 2005.

Takei, Y., and B. K. Holtzman, Viscous constitutive relations of solid-liquid composites in terms of grain boundary contiguity: 3. causes and consequences of viscous anisotropy, *Journal of Geophysical Research*, *114*(B06207), doi:10.1029/2008JB005852, 2009.

Tan, E., and M. Gurnis, Compressible thermochemical convection and application to lower mantle structures, *Journal of Geophysical Research*, *112*(B6), B06,304, doi:10.1029/2006JB004505, 2007.

Telles, J., A self-adaptive coordinate transformation for efficient numerical evaluation of general boundary element integrals, *International Journal for Numerical Methods in Engineering*, *24*, 959–973, 1987.

Thorne, M. S., E. J. Garnero, G. Jahnke, H. Igel, and A. K. McNamara, Mega ultra low velocity zone and mantle flow, *Earth and Planetary Science Letters*, *364*, 59–67, doi:10.1016/j.epsl.2012.12.034, 2013.

von Bargen, N., and H. Waff, Permeabilities, interfacial areas and curvatures of partially molten systems: results of numerical computations of equilibrium microstructures, *Journal of Geophysical Research*, *91*, 9261–9276, 1986.

Walsh, J., New analysis of attenuation in partially molten rocks, *Journal of Geophysical Research: Solid earth and Planets*, *74*(17), 4333–4337, 1969.

Wicks, J. K., J. M. Jackson, and W. Sturhahn, Very low sound velocities in iron-rich (Mg,Fe)O: Implications for the core-mantle boundary region, *Geophysical Research Letters*, *37*(15), 1–5, doi:10.1029/2010GL043689, 2010.

Williams, Q., and E. Garnero, Seismic evidence for partial melt at the base of Earth's mantle, *Science*, *273*, 1528–1530, 1996.

Wimert, J. T., and S. Hier-Majumder, A three-dimensional microgeodynamic model of melt geometry in the earth's deep interior, *Journal of Geophysical Research: Solid Earth*, *117*(B04), B04,203, doi:10.1029/2011JB009012, 2012.

Wray, P. J., The geometry of two-phase aggregates in which the shape of the second phase is determined by its dihedral angle, *Acta Metallurgica*, *24*, 125–135, 1976.

Xu, W., C. Lithgow-Bertolini, L. Stixrude, and J. Ritsema, The effect of bulk composition and temperature on mantle seismic structure, *Earth and Planetary Science Letters*, *275*, 70–79, 2008.

Zimmerman, M. E., S. Zhang, D. L. Kohlstedt, and S.-I. Karato, Melt distribution in mantle rocks deformed in shear, *Geophysical Research Letters*, *26*(10), 1505–1508, 1999.